UNIVERSITY OF OKLAHOMA

GRADUATE COLLEGE

USING 3D SEISMIC ATTRIBUTES TO INVESTIGATE MUD LOSSES IN A FLUVIAL-DELTAIC SAND: AN EXAMPLE FROM THE OLIVER SANDSTONE.

A THESIS

SUBMITTED TO THE GRADUATE FACULTY

in partial fulfillment of the requirements for the

Degree of

MASTER OF SCIENCE

By

JAKE AUSTIN ELDER
Norman, Oklahoma
2017

USING 3D SEISMIC ATTRIBUTES TO INVESTIGATE MUD LOSSES IN A FLUVIAL-DELTAIC SAND: AN EXAMPLE FROM THE OLIVER SANDSTONE.

A THESIS APPROVED FOR THE
CONOCOPHILLIPS SCHOOL OF GEOLOGY AND GEOPHYSICS

BY

_____
Dr. Kurt Marfurt, Chair

_____
Dr. Matthew Pranter

_____
Dr. Bradley Wallet

To my Mother and Father for instilling in me the attitude to always push myself ; and to my big Sister for always setting the bar high and being a good example for me to follow.

Acknowledgements

I would like to thank all my friends and colleagues who provided their knowledge, support, and kind words to assist me in the writing of this thesis. I would also like to thank my advisor Dr. Kurt Marfurt and committee members Dr. Matthew Pranter and Dr. Brad Wallet for having a great deal of patience with me throughout this process.

Table of Contents

List of Tables

List of Figures

Abstract

Drilling operations in an actively developed basin in Wyoming can experience large quantities of mud losses in a shallow zone along the intermediate (vertical) section of the wellbore. These losses can negatively impact well economics due to the unforeseen expenditures that come with the price of the mud itself and the extended rig time it takes to overcome the mud loss issues. A typical well in the area costs approximately 8 million dollars, of which, drilling cost accounts for 40-50%. Of the roughly $4 million associated with the drilling cost, rig time makes up ~20%, and rig rates range from $18,000 - $25,000 a day. It is common for severe losses to take multiple days of additional rig time and even minor mud loss issues can add ~12 - 24 hours.

Since the depositional nature of fluvial deltaic sands produces moderate to high degrees of grain sorting which translate to moderate or high values of porosity and permeability, I hypothesized that regions in the Oliver sandstone exhibiting porosity and permeability may correlate with localized areas of mud loss. Unfortunately, many of the lost circulation wells do not have logs within the Oliver, prohibiting a direct mud loss versus log porosity correlation. In contrast, all of the wells are contained within a seismic data survey, providing an alternative correlation workflow. I computed a suite of seismic attributes which reveal subtle depositional and structural information about the area. There was no significant correlation of mud loss to structural attributes (e.g. similarity, curvature, and dip magnitude). The same suite of seismic attributes were analyzed using an Artificial Neural Network (ANN) algorithm to predict estimates of porosity within the region of interest. Although the resultant volume delineated

laterally variable zones of low and high porosity in the Oliver Sandstone, the correlations between mud loss volumes and porosity were very low, concluding that porosity does not have a direct influence in the lost circulation.

Chapter 1: Introduction

Geo-hazard identification is one of the many tasks interpretation geophysicists and geologists deal with regularly. Faults, zones of overpressure, and naturally fractured formations are just a few of the common hazards that geoscientists attempt to identify and avoid. In order for drillers to reach a prospective formation for oil and gas production, they must first penetrate several thousand feet of shallower rock termed the intermediate section of the well; while drilling they circulate fluid known as drilling mud down-hole. This fluid serves many functions such as carrying wellbore cuttings to the surface, providing buoyancy to the drill string, sealing permeable formations, and most importantly controlling formation pressures. When a drilling rig encounters a highly fractured zone or an interval of rock with well-developed porosity/permeability, much of the drilling fluid being pumped downhole may be lost to absorption. These events are termed "mud losses" and are very costly to E&P companies due to the cost of the mud itself and the extended rig time that can be associated with the occurrence of such hazards. Drilling fluid cost is about 8% of total drilling cost, amounting to ~$300,000 on average. With water based mud (typical mud system used while drilling across the Oliver) only costing $1-3 per barrel, the volume of losses for this study (ranging from 80 – 8,000 bbls) does not significantly impact well cost, but over the development life of a basin these can quickly add up. In this study we have 28 wells with losses (8.5% of all development locations) and an average lost volume of 1,600 bbls and 12 hours of rig time which adds ~$3,200 and $10,000 per well, respectively. For example, an undeveloped basin which may have 2,500 locations to drill, would result in an additional 2.8 million dollars being spent on drilling costs related to mud

losses. These additional costs are the motivation behind investigating the mud losses observed in the basin. Successfully identifying the cause of the losses and predicting similar hazards prior to drilling, would give valuable foresight so that engineers can design a mud program to mitigate this hazard.

Analysis of the approximate depths and volumes of the losses recorded by the drillers reveal that a significant number of the losses are occurring near the Oliver sandstone formation, in the upper section of the stratigraphic column. The lateral and vertical variability of sand deposition in the system, coupled with the spatial aliasing due to finite well separation, imposes high uncertainties in log correlations. Compounding this problem, many well logs in the area are not recorded in the shallow stratigraphic interval. These complexities lead to uncertainties in the cause of mud loss with previous attempts to predict hazardous trends in the Oliver Sandstone being unsuccessful. The ability to identify the source of mud losses and to predict future occurrences is key to avoiding or minimizing the cost associated with these events.

The mud loss zone addressed in this paper occurs in the Oliver Sandstone, deposited in a fluvial-deltaic environment. These deposits have long been identified as high quality sandstone reservoirs that have the potential to store large volumes of hydrocarbons. Although clastic packages within the fluvial-deltaic environment are often the target of hydrocarbon exploration or exploitation efforts, they can also have a negative impact on drilling procedures for E&P companies when they are associated with mud losses during operations that target deeper formations. Characterization of a fluvial-deltaic environment includes determining the lateral heterogeneity, the thickness, and the connectivity of individual sand intervals. In addition to these

depositional parameters it is also critical to understanding reservoir properties such as porosity, permeability and pressure. The primary source of porosity information comes from borehole logging data where density porosity or neutron porosity curves have been recorded. Unlike porosity, permeability is not directly measured from well logs, but due to the relationship that exists between porosity and permeability (Tiab and Donaldson, 2004), estimations of permeability can be made using porosity data. Understanding these rock properties for the Oliver Sandstone and mapping their distribution is imperative to interpreting hazardous areas where mud losses may be expected.

In this thesis, I evaluate four different potential causes for the mud losses in the Oliver sandstone (1) intersection of channels, (2) connectivity of higher porosity regions, (3) proximity to faults and flexures, and (4) stratigraphic zones with enhanced permeability. I begin my paper with a review of the geologic setting and of the Oliver formation in particular. Then I examine the data available, including a summary of the mud losses incurred. Next, I describe some of the tools used in the analysis, including data conditioning, seismic attributes, artificial neural networks (ANN), and self-organizing maps (SOM). I then evaluate each of my four hypotheses, emphasizing the assumptions and limitations of each. I conclude with a summary of my findings and suggestions for further work. Finally, I add details of petrophysical, seismic inversion, and neural network analysis as appendices.

Chapter 2: Geologic Setting

The Oliver sandstone was deposited in an asymmetric foreland basin during the late Cretaceous. Basin wide sediments include sandstone, siltstone, claystone, and shale (Dyman et al., 1994). The steeply dipping western side of the basin includes mainly non-marine deposition with an abundance of conglomerates with rapid subsidence. The more shallowly dipping eastern portion of the basin is predominantly marine strata deposition including some chalks and limestones. Sediment deposition occurred during sea level fluctuations caused by tectonic and eustatic cycles (Dyman et al., 1994). Strata within the basin range from depths of 20,000 ft to less than 1,000 ft and helped shape the asymmetry of the basin through differing rates of subsidence from sediment loading (Dyman et al., 1994). In the early Cretaceous, sediments formed a foreland wedge which was later deformed by the Laramide uplift (Dyman et al., 1994). The main structural features within the basin include folds, normal faults, reverse faults, high angle faults, and wrench faults (Blackstone, 2005). Basin-bounding structures include several uplifts, the timing of which have contributed greatly to the complexity of structural features. Large east-west trending wrench faults can be seen easily on seismic attributes such as curvature (Figure 1) and are potentially contributing to the mud losses.

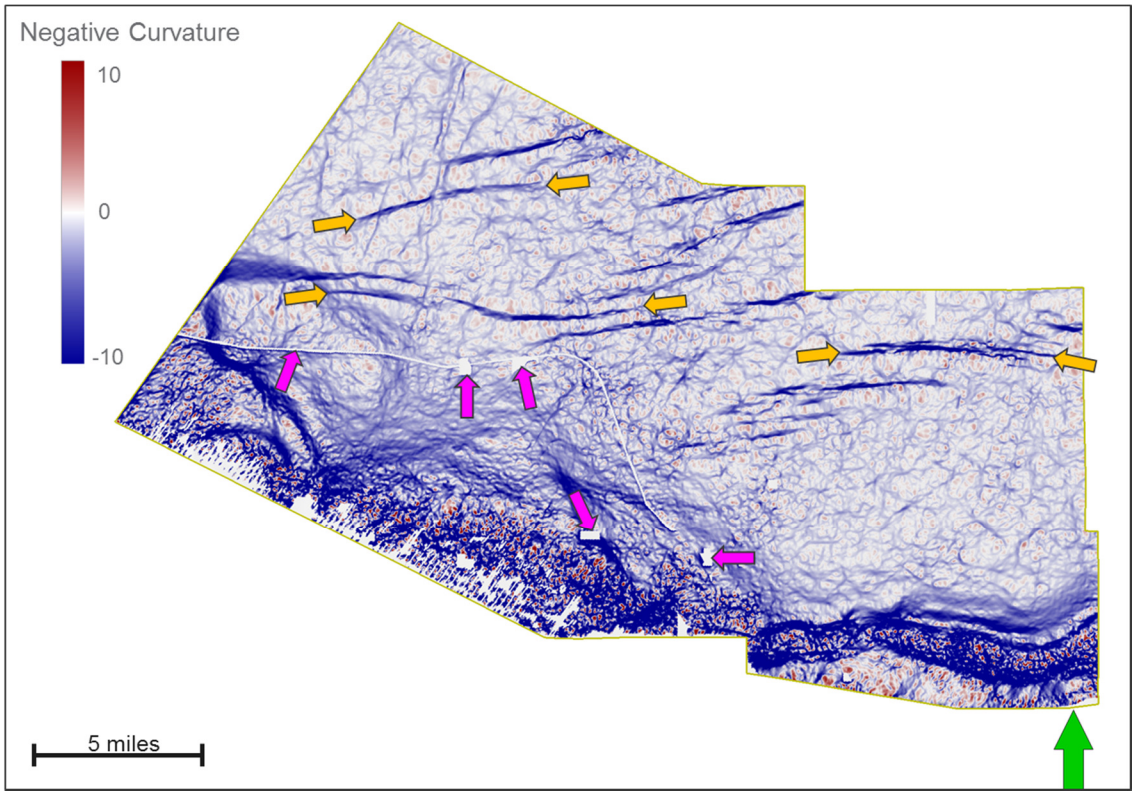

Figure 1. Most negative principal curvature along the Oliver horizon. Orange arrows indicate some of major wrench faults that are prevalent in the basin, pink arrows indicate missing data zones in the seismic. These high magnitude curvature features identify areas that are more prone to natural fractures that may be causing some of the mud losses.

The Oliver sandstone is a river-dominated deltaic sandstone. Sand deposition in this kind of geologic setting can manifest itself in many different ways: In the Delta Plain (coastal environment) thicker sands occur in multistory channel systems, while thinner sands occur as isolated channel sands and crevasse splays; in the delta front (transitional environment), thicker accumulations of mouth bar deposits are most proximal to the channels. These deposits will progressively thin as they transition to more distal facies; in the pro-delta (marine environment) muddy marine deposits are prevalent, but sand bodies may occur as a result of silty turbidite flows or submarine fans flowing off the coastal shelf. In addition to sand body distribution and thickness,

connectivity is another significant aspect of fluvial reservoir characterization, as noted by Pranter et al. (2008, 2010) in their studies on the Williams Fork formation. The Oliver sandstone is normally under pressured, with up to 20% porosity. Inferred values of permeability for the Oliver are ~50 mD when compared to work done by Mullen and Barlow (1993) in the Greater Green River Basin. Given these reservoir properties I would expect to see a higher likelihood of mud losses with increased connectivity of the sand bodies.

Chapter 3: Available Data

The 3D seismic volume encompasses ~320 square miles of good quality data processed using pre-stack 5D OVT time migration. The survey was shot using a combination of vibroseis and dynamite sources with a source point spacing of 220 feet and source line spacing of 1320 feet. Receiver lines were spaced at 880 feet with receiver stations at 220 foot intervals, and with each station consisting of a group of six 10 Hz geophones. Two versions of the data were provided, one having enhanced processing which includes whitening of frequencies from 4-90 Hz (Figure 2a) and another volume, which has the original spectrum preserved (Figure 2b). I will refer to the whitened volume as the "enhanced" survey and the non-whitened volume as the "raw" survey. Figure 3 shows the distribution of different log data used in the project, while Figure 4 shows the locations of wells with mud losses colored by volume of mud lost.

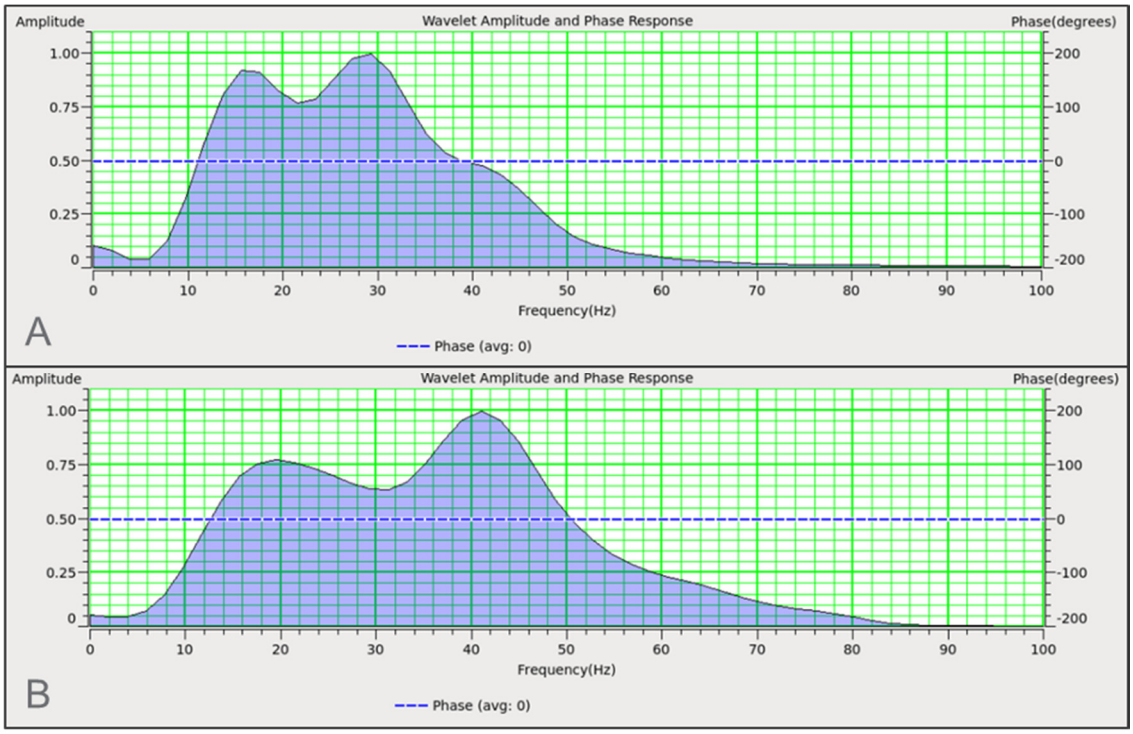

Figure 2. The spectrum (A) before and (B) after spectral balancing resulting in increased signal strength between 35-50 Hz.

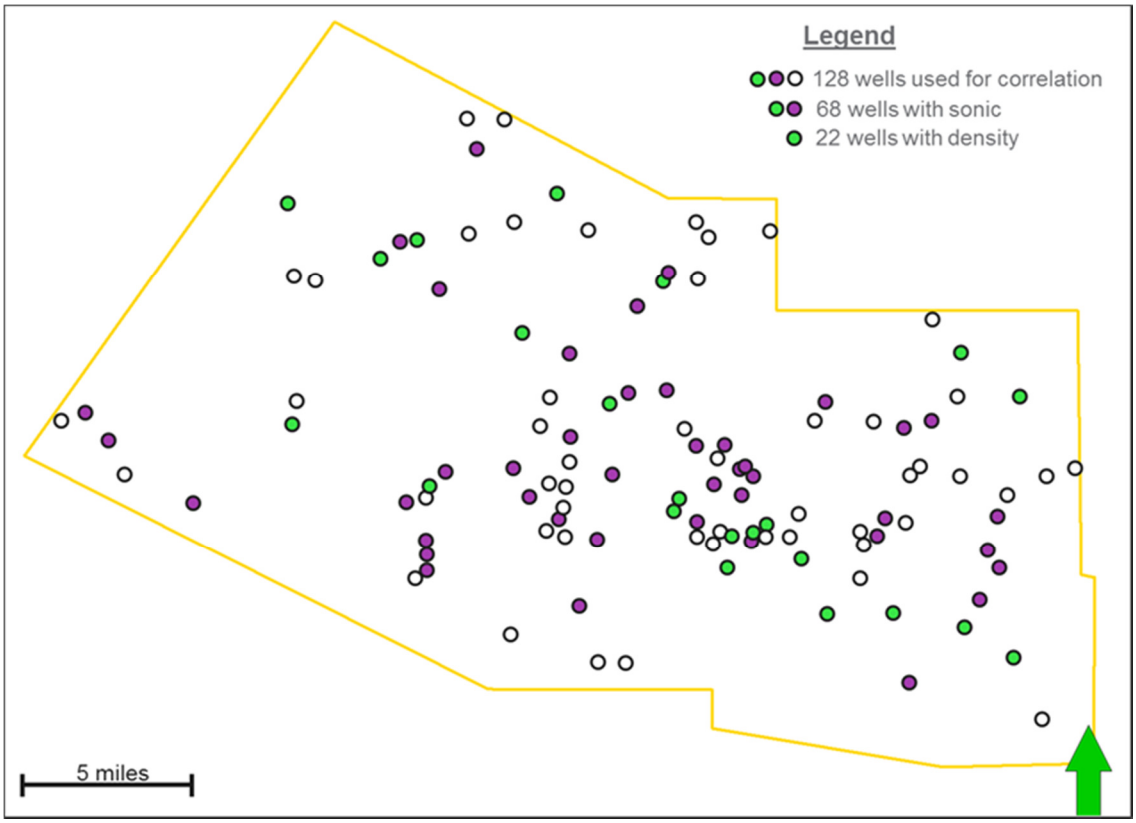

Figure 3. The yellow outline shows the limits of seismic data coverage. The black circled wells indicate the 128 wells that had usable data over the Oliver (e.g. at least containing a log curve for correlations). The purple highlighted wells contain sonic logs that were used for well ties. The 22 green highlighted wells contain both density curves and sonic logs and represent the wells used in the inversion and neural networking.

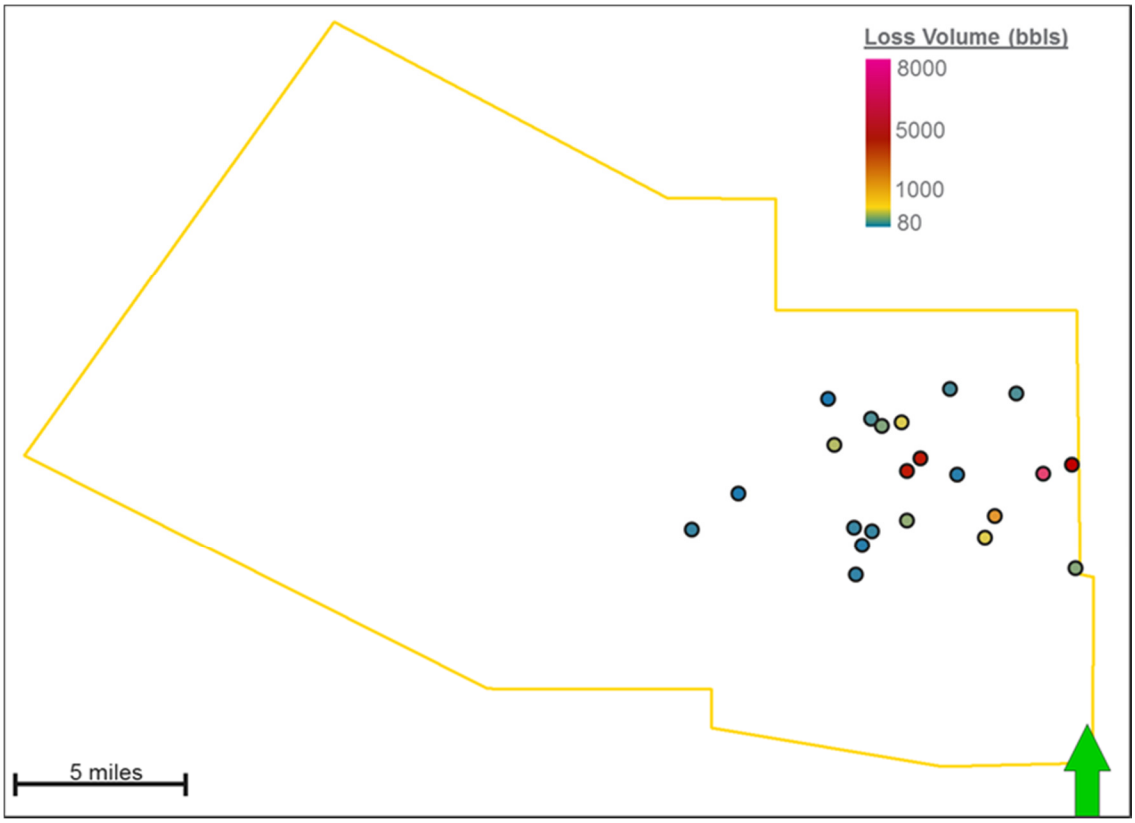

Figure 4. Location of wells with mud losses, color filled by the volume of mud lost.

Chapter 4: Methodology

Stratigraphic Framework

Nine stratigraphic tops were identified and correlated across the 128 wells. The resistivity response was the primary curve used for correlations but sonic and gamma ray logs were also incorporated into the interpretation. The lowest stratigraphic top in the section is the Oliver Marker which is picked on a consistent resistivity response that identifies the base of the basal shale which lies just beneath the Oliver gross interval. Just above that is the Top Shale followed by the Oliver 100, 200, 250, 300, 400, 500 and Top Oliver respectively (Figures 5 and 6). The gamma ray character of the upper portion of the Oliver is consistent with our depositional model of a fluvial deltaic system and displays many key traits such as a broad coarsening upward sequence, interspersed mud and coal deposits, overlain by a large fluvial sequence which contains fining upward deposits indicative of channels as well as erratic thin sands indicative of crevasse splays. The Oliver 300, 400, and 500 define the tops of different prograding sand packages in the Upper Oliver (i.e. above the Oliver 200). The Oliver 200 itself is a maximum regressive surface that marks the beginning of a lower order transgression which leads up to the final progradation of the Upper Oliver. Using sonic logs, I generated synthetic seismograms to create a time depth relationship between wells and tied the logs to the seismic data. Not all stratigraphic horizons could be picked on the seismic data, partly due to the high-order nature of some sequences but also because reflector behavior within the Oliver is chaotic and time consuming to interpret. Since the focus is primarily on the Oliver interval as a whole I picked the Oliver and Oliver Marker to constrain the zone of interest. Additional picks for the Oliver 300, 200 and

Top Shale were also created in case any subintervals needed to be analyzed (Figure 7 and 8).

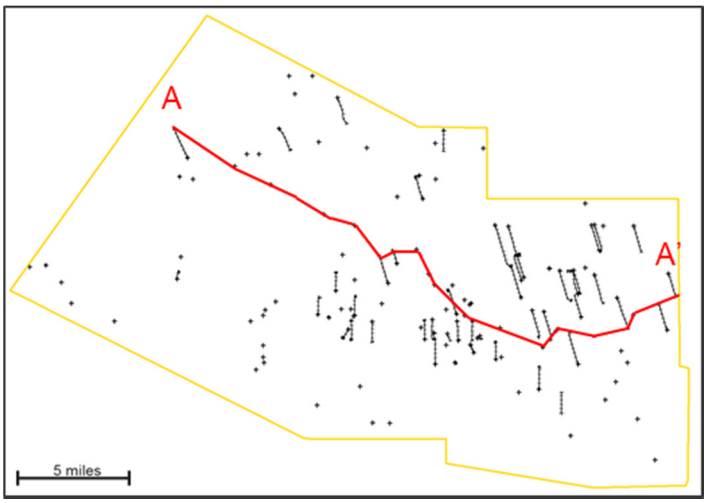

Figure 5. Map showing the location of cross section A-A'

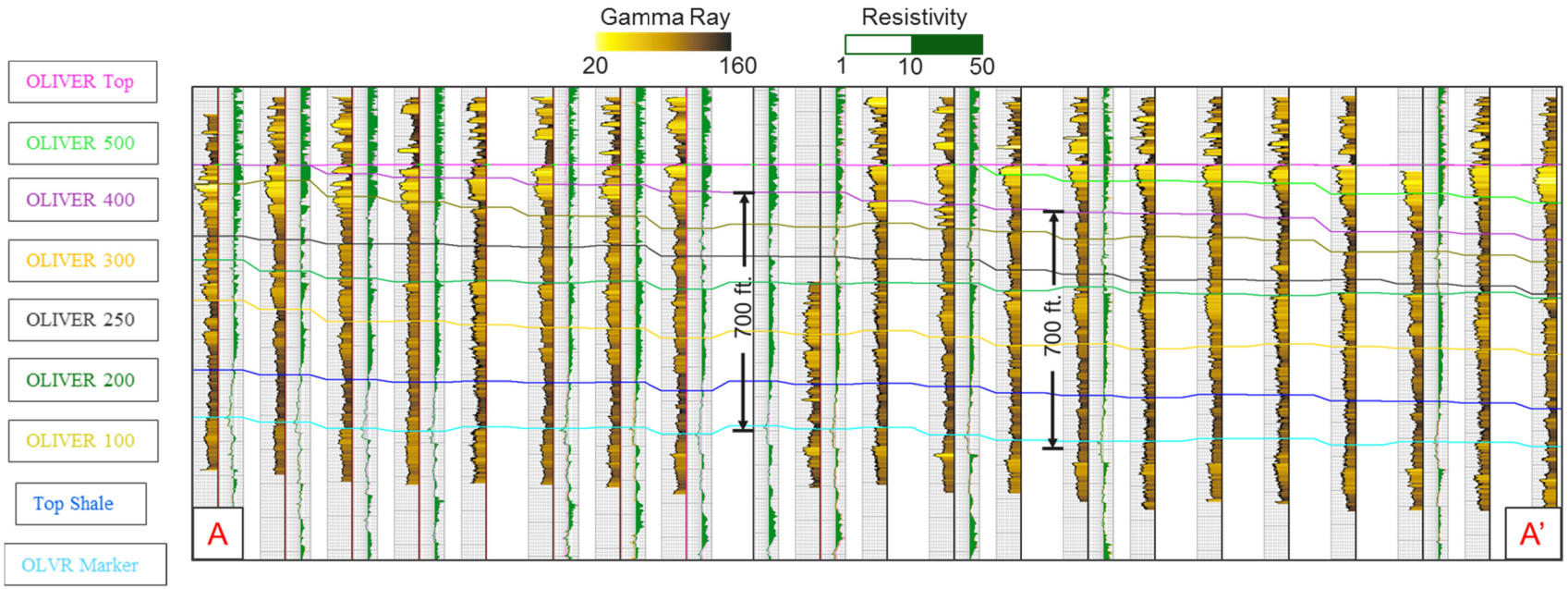

Figure 6. Cross section of sequence stratigraphic top picks displaying the progradational nature of the Upper Oliver.

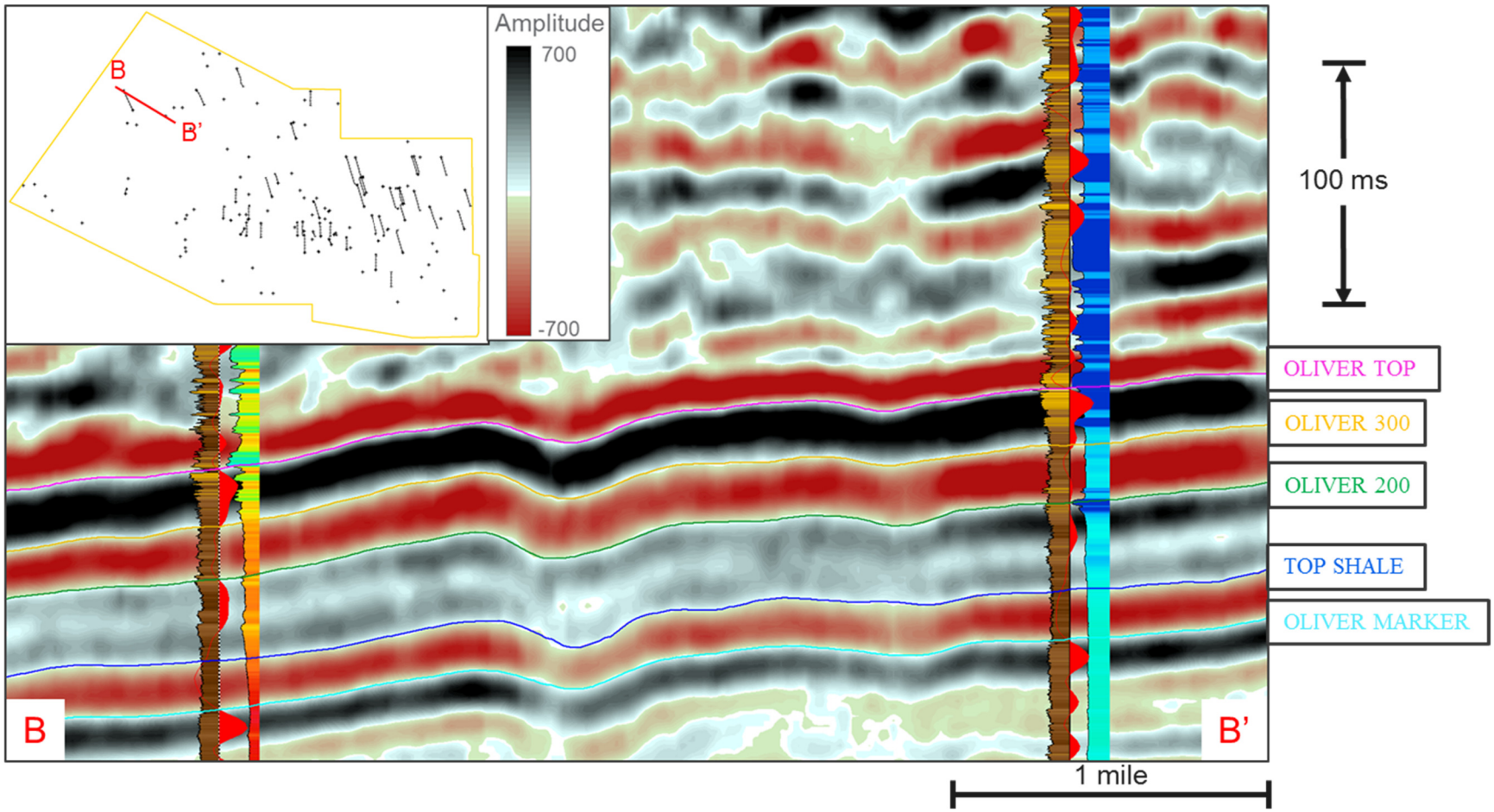

Figure 7. Well ties in the west part of the study area show that the Oliver top correlates to a "Z" – crossing (the zero crossing above a peak).

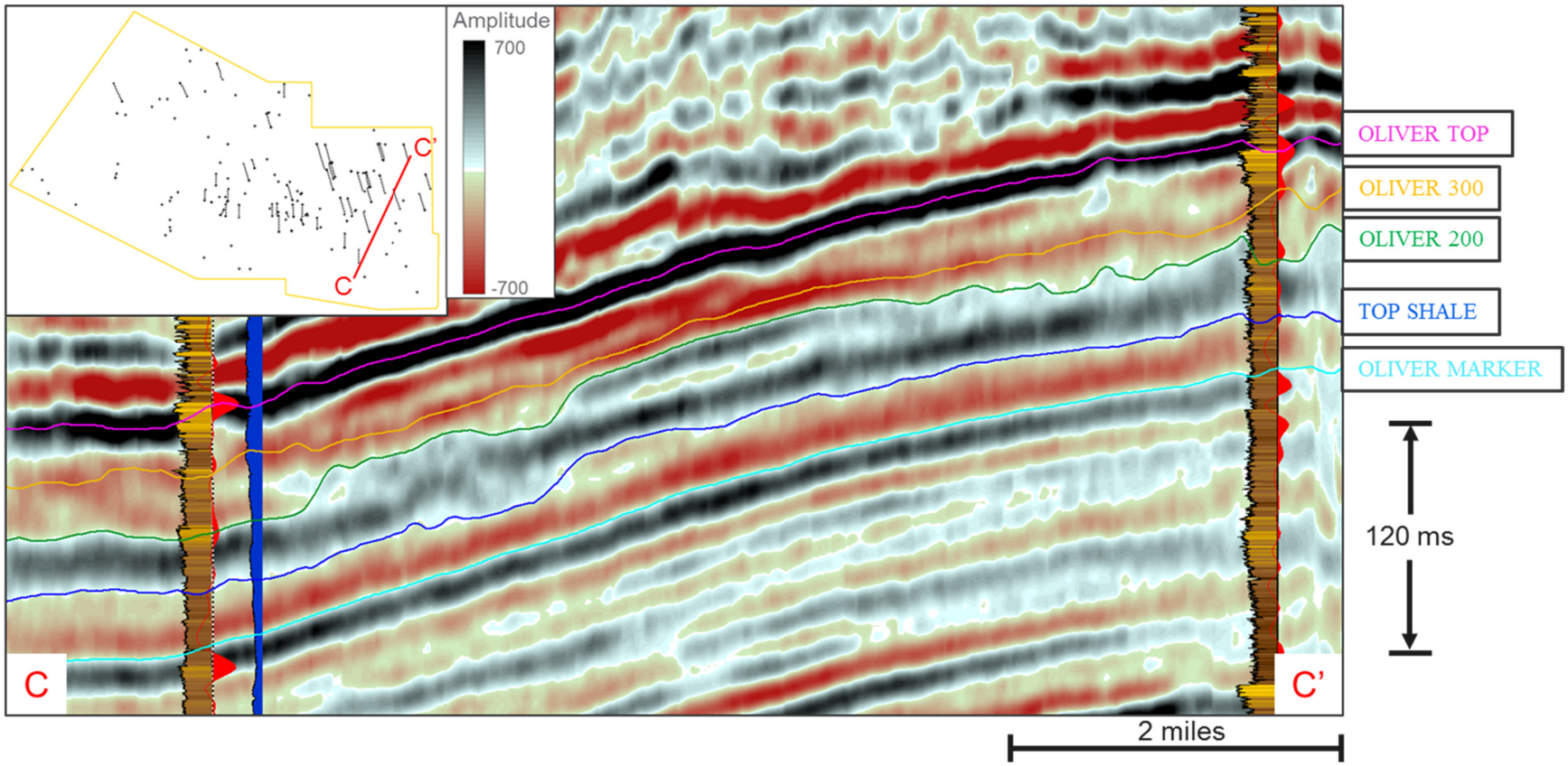

Figure 8. Well ties in the east part of the survey show that the Oliver pick has changed to a peak. This change in the phase of the pick across the study area indicates a change in the depositional environment across the survey**.**

Data Conditioning

The raw data set contains a significant amount of footprint, predominantly in the inline direction as well as a secondary set of footprint with a northwest-southeast orientation (Figure 9). The severity of the footprint is greatly reduced in the enhanced data, and the overall signal-to-noise ratio and smoothness of amplitudes are superior to that of the raw data. Due to the quality of the enhanced data, I initially ran attributes over that volume.

The first step in calculating seismic attributes requires computing inline and crossline dip volumes. Input parameters include average rock velocity and maximum dip values. A value of ~12,000 ft/s was obtained for velocity by averaging slowness over three sonic logs and converting the units to velocity. This value is reasonable for a clastic sedimentary basin and consistent with expectations. Maximum dips for the seismic survey were estimated by calculating the slope between a selected formation top at two different wells (one well located on the structurally higher part of the basin margin and one well down dip from this, located near the base of the margin structure). The calculated slope was 73 percent (~36^{o} dip), but to account for dip variations between the two wells and to assure improved imaging near the basin margin, a value of 45 degrees is used in the dip calculations. A dip increment of 3^{o} was used to provide a good estimation of the dip magnitude but still maintain efficient computation time. In an effort to further reduce computation time and minimize the usage of storage space, the volume was trimmed from 5 seconds to 3 seconds, which is reasonable since acoustic basement was reached at ~3 seconds and no coherent reflectors exist deeper than this.

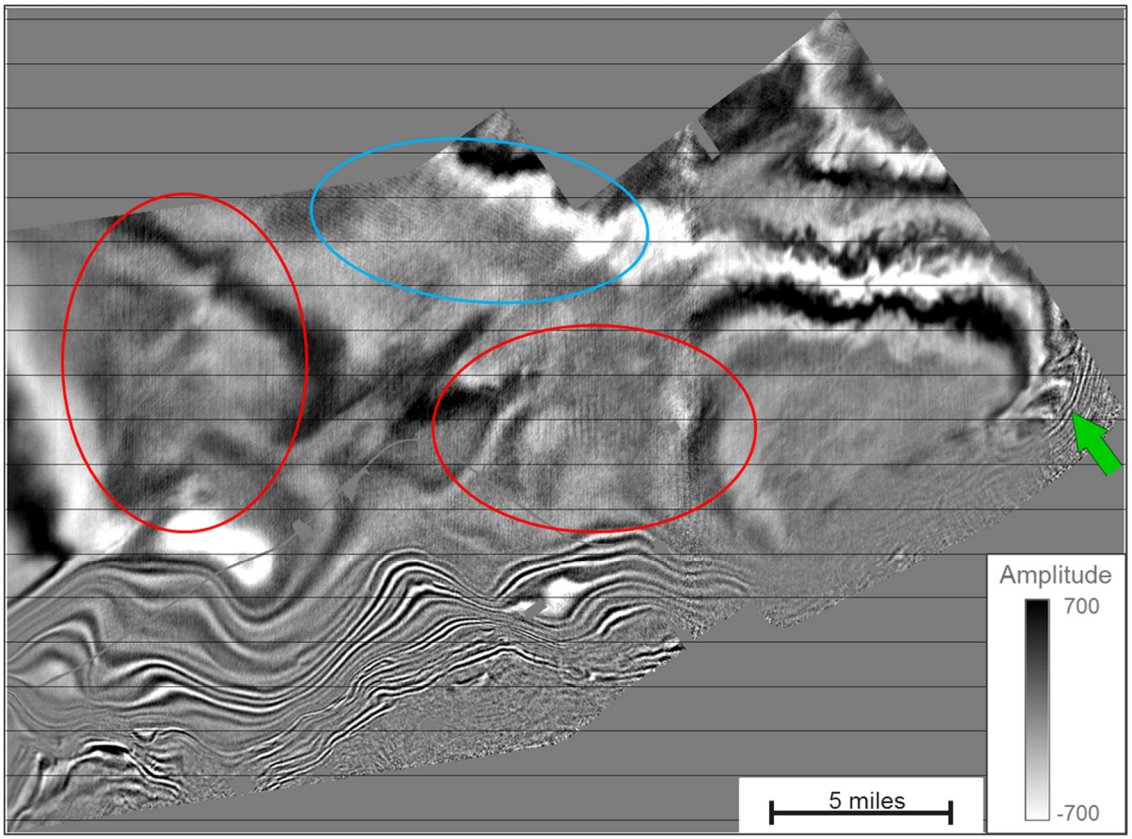

Figure 9. Time slice at t= 2.5s through the seismic amplitude volume. Red circles show the strong footprint in the inline direction, the blue circle highlights a secondary set of footprint trending northwest-southeast.

After the dip calculation, many iterations of structural attributes were run to identify any noise issues. Structural attributes are useful for highlighting both coherent noise (e.g. footprint) and incoherent noise because of their sensitivity to small fluctuations in phase, amplitude, and/or dip. Reviewing the negative curvature calculations on the enhanced volume revealed large swaths of high frequency noise at 1.5 seconds (the approximate time of the Oliver sandstone interval) which hindered the interpretability over much of the survey (Figure 10). Subsequent testing of different parameters for both the dip and curvature calculations continued to yield undesirable results. Panning through time slices it appeared that high magnitude noise at 3 seconds

(i.e. the base of the volume) correlated to the exact areas of noise contaminating the volume near the zone of interest at 1.5 seconds (Figure 11). The issue was presumably caused by the discontinuous reflectors present near the base of the volume, which caused the large magnitude curvature features to propagate throughout the volume (Figure 12).

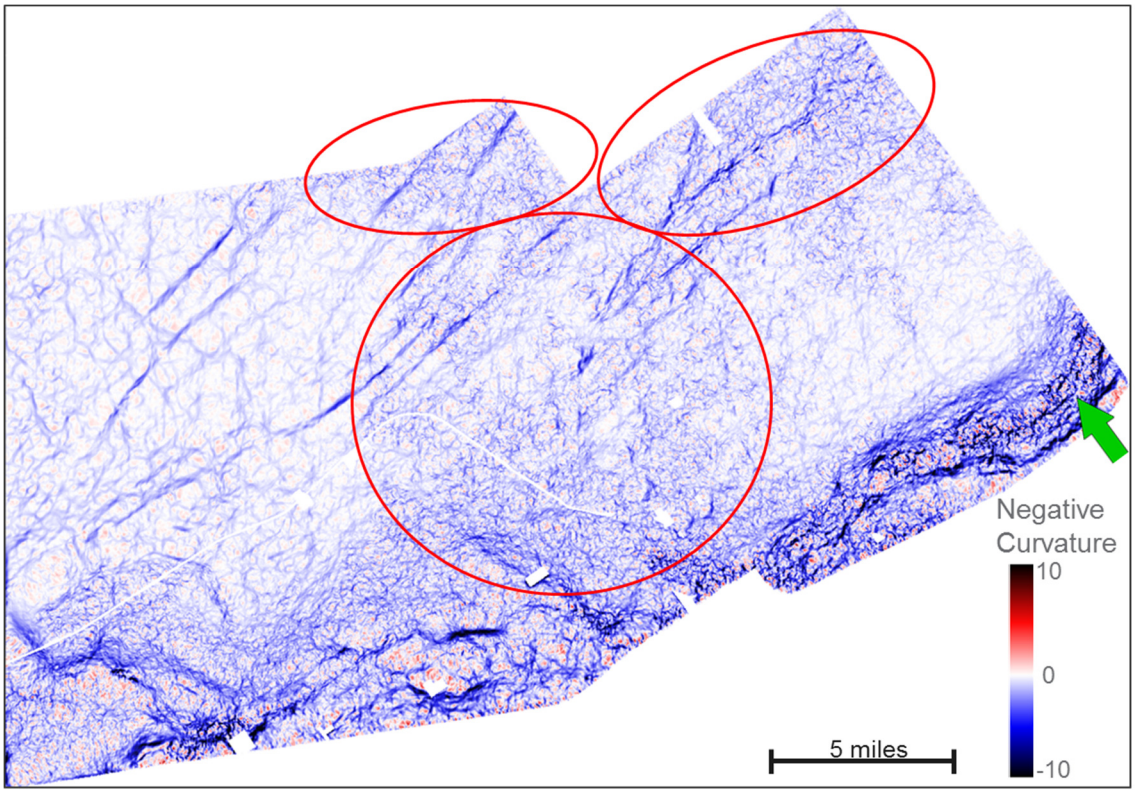

Figure 10. Time slice a t=1.5 s through the most negative curvature volume. Regions contaminated with noise are circled with red.

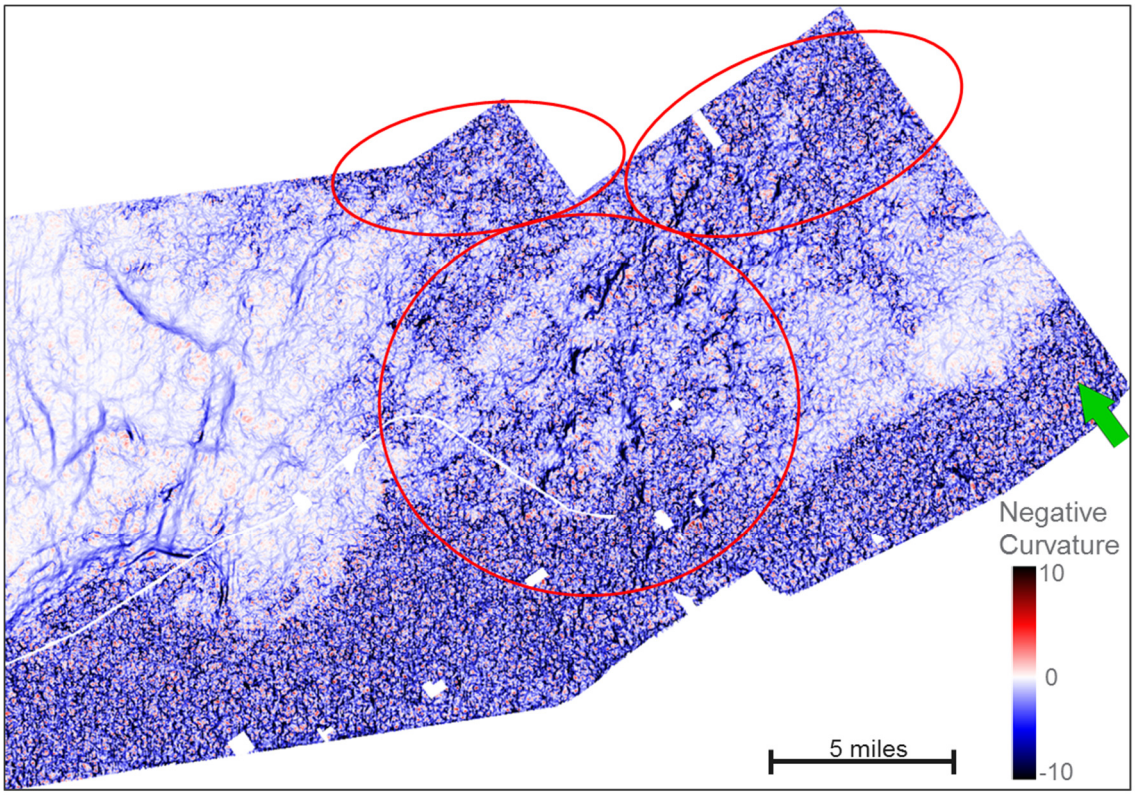

Figure 11. Time slice at t=3.0 s through the most negative curvature volume. The noise at 3 seconds is much worse and in the exact location as shown in Figure 14. This leads me to believe the high frequency noise in the basement at 3 seconds is bleeding up through the entire volume.

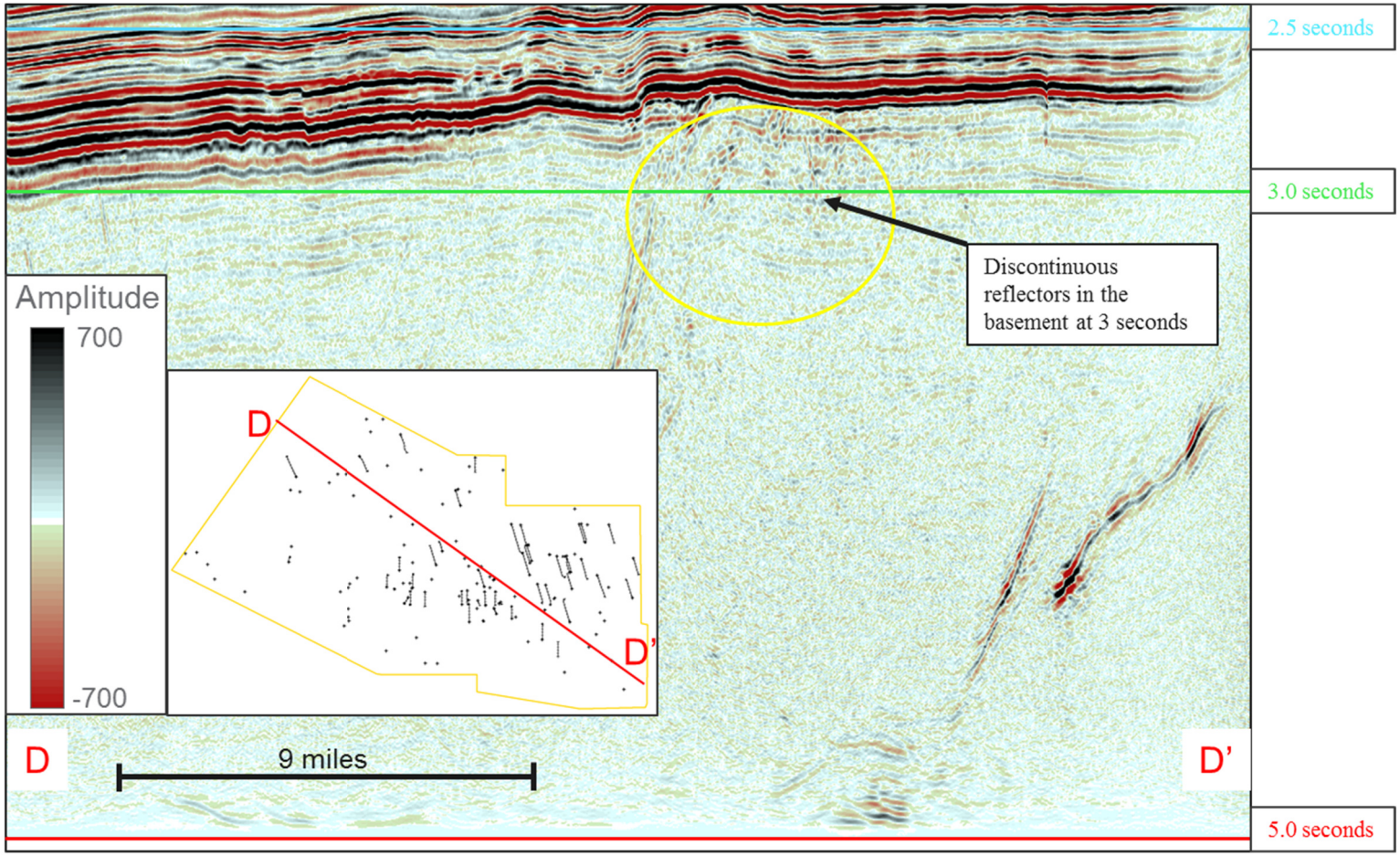

Figure 12. Crossline through seismic amplitude with 2.5 s, 3.0 s, and 5.0 s demarcated. The 3.0 second line cutting across some incoherent reflectors in the basement is likely sourcing the noise in the curvature maps. To alleviate this we try a 2.5 second crop and a 5.0 second crop. The top of the volume has been cropped in this image to focus on the lower portion of the volume.

To eliminate this issue the volume was re-cropped using two different approaches. The first approach was trimming the volume to 2.5 seconds to put the base of the volume in closer proximity to more coherent reflectors, in an effort to reduce noise smearing throughout the volume by avoiding noisy regions in the basement. The second approach included using the full 5 second volume to put the base of the data much deeper than the problematic zone at 3 seconds, allowing the noise to attenuate across the length of a longer trace. Both the shallower (2.5 second) time cut-off and the deeper (5 second) time cut-off resulted in superior interpretability when compared to the 3 second trimmed volume (Figure 13 and 14).

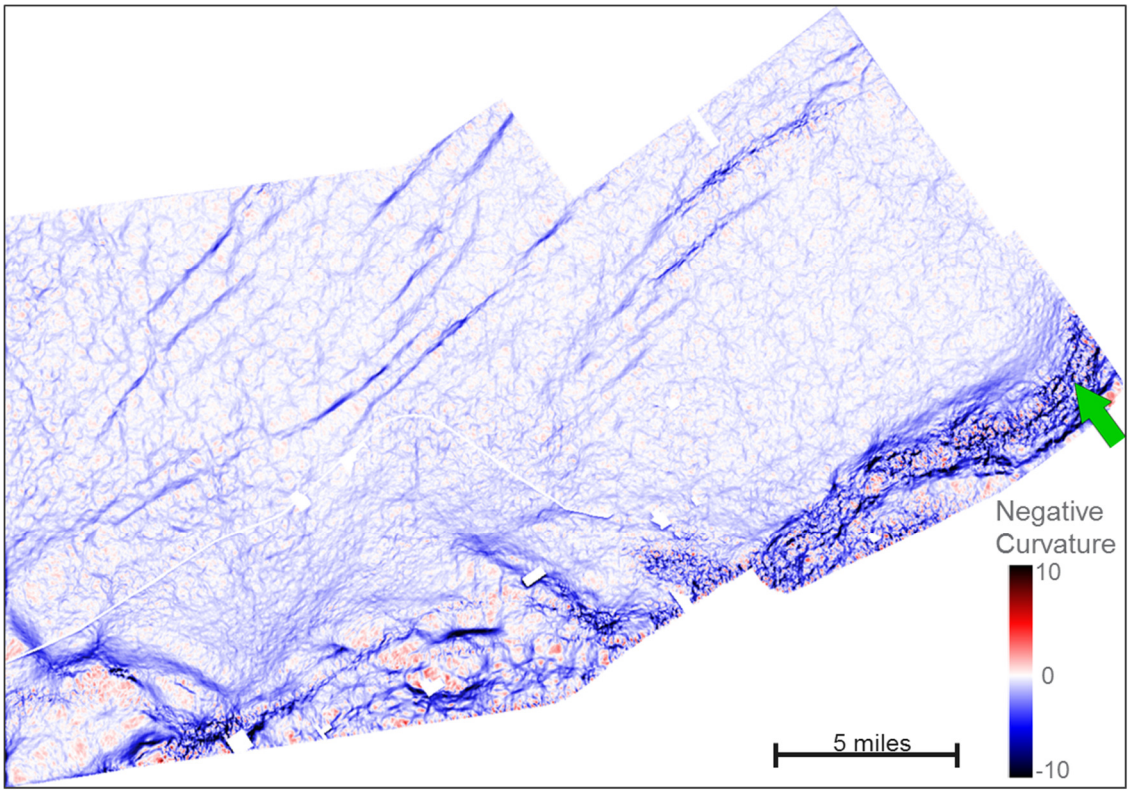

Figure 13. Time slice at t=1.5s through the most negative curvature volume cropped at 5 seconds. This iteration is superior to the 3 second cropped version in figure 14, placing the base of the volume much deeper than the noisy basement reflectors shown in Figure 12.

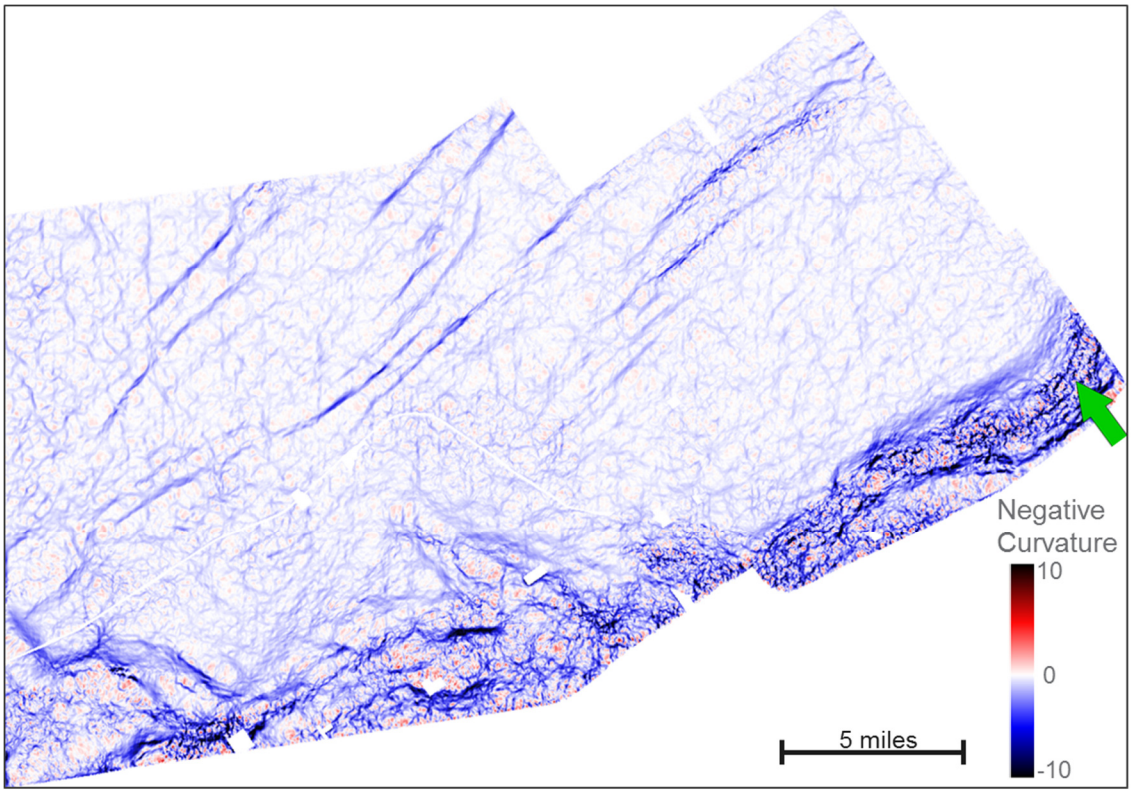

Figure 14. Time slice at t=1.5s through the most negative curvature on the 2.5 second cropped volume. This version also provides a cleaner result than Figure 14 by cutting across shallower coherent reflectors as shown in Figure 12.

In addition to running attributes on the newly improved volumes, I also tested attributes with the raw data as an alternate option. Time slices of the attributes in the raw survey provide significantly better detail of fine features compared to the same attributes in the enhanced survey. Because spectral attributes are a key input into the neural network, the raw data is preferential since the enhanced dataset has a whitened spectrum where frequencies have been artificially boosted. To avoid using the enhanced data, a footprint suppressions workflow was implemented on the raw seismic volume to improve the quality and salvage the data for use in the remainder of the project. The data were transformed to the f-k domain, where the seismic data are now viewed with respect to frequency and wave number as opposed to time and spatial distance. Time

slices were analyzed until the coherent footprint clusters were easily identified in the f-k plot (Figure 15a). The coherent noise was most identifiable on shallower time slices and these spots were then filtered out of the data (Figure 15b), thus suppressing the expression of acquisition footprint (Figure 16).

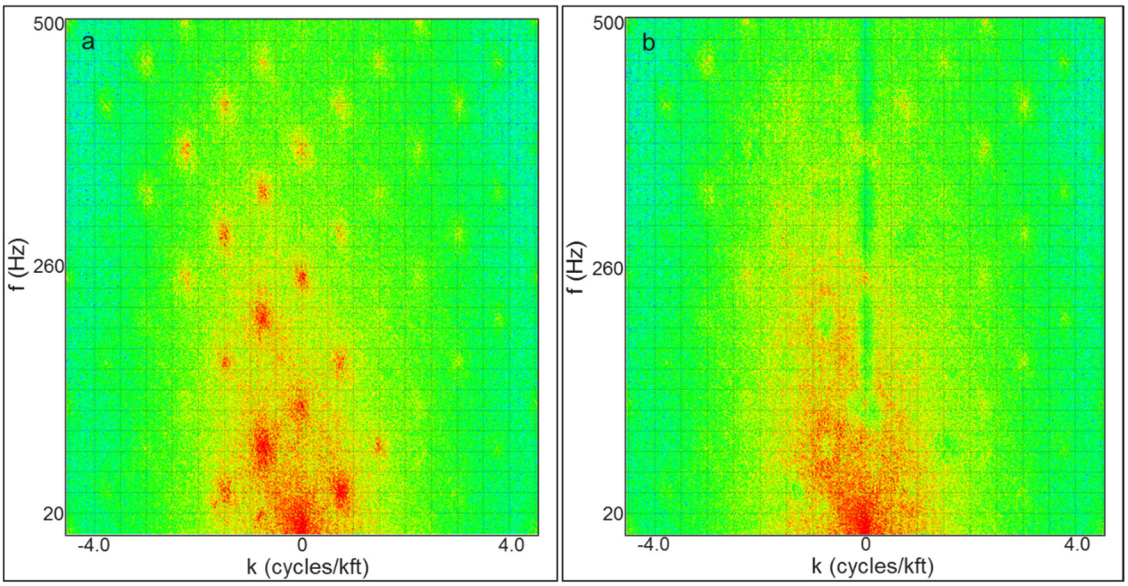

Figure 15. (a) f-k plot of the raw data to show clusters of regularly spaced coherent noise perpendicular to the inline direction. (b) The f-k plot following the noise filtering.

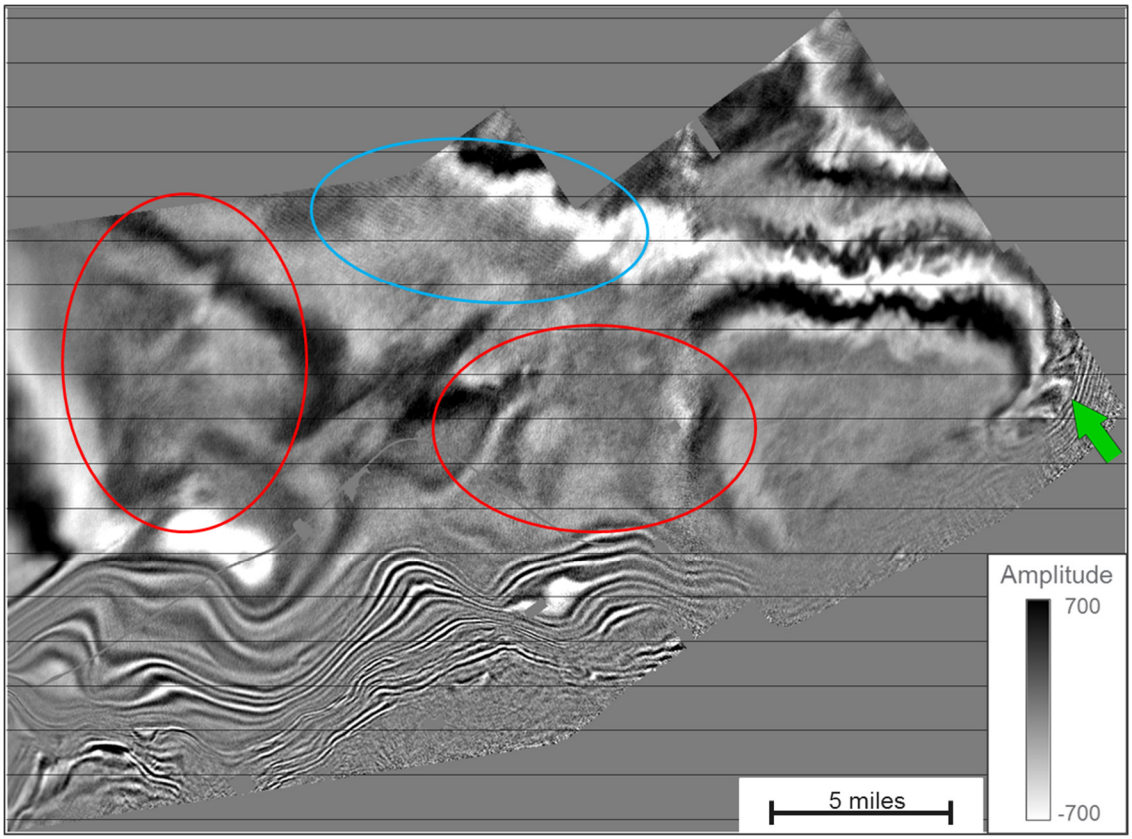

Figure 16. The same time slice shown in Figure 9 after footprint suppression. The inline footprint has been removed but the secondary footprint direction (highlighted in blue) is still present.

The first pass of structure oriented filtering (SOF) was run on the noise suppressed data keeping the first two principal components in order to preserve the signal. Random noise still contaminated the similarity attributes after the first pass of principal component filtering, so a second pass SOF median filter was applied to the data. This removed the noise on the similarity attributes but preserved the fine-scale details of interest, improving the final curvature image (Figure 1), and providing an acceptable amplitude volume to use for the remainder of the project.

Seismic Attributes

In total, 63 attributes were calculated from the final conditioned volume primarily using the AASPI software as well as some attributes calculated in Petrel (Table 1). Extensive work has been carried out on the interpretation of seismic attributes and the importance of their role in reservoir characterization (Chopra and Marfurt, 2007). Understanding the goals of the project is essential for determining which attributes to feed into a neural network. A key attribute for the neural network in this project is acoustic impedance because it is influenced by porosity and the output we want from the neural network is a predicted porosity volume. Other inputs that were considered included, amplitude related attributes (envelope, coherent energy, etc.), frequency attributes (peak frequency, spectral components, peak phase, etc.), and GLCM textural attributes (entropy, mean, homogeneity, etc.) among a suite of others that maybe be supplemental to these (e.g. cosine phase, derivative volumes, etc.). All of these seismic attributes have shown sensitivity to imaging depositional environments and can potentially image differences in rock properties, such as lithology (which could correlate to changes in porosity) or thickness. I hypothesize that even if a small portion the attribute response is influenced by changes in porosity, the neural network will be able to delineate that complexity through its nonlinear analysis.

Structural attributes are calculated to further investigate the contribution of fractures or faulting to the losses. Primary attributes of interest are principal curvatures, similarity, and shape index. The additional structural interpretation will provide a more comprehensive look at the problem and might explain any outliers in the correlations with porosity.

Seismic Attribute List	
Attribute	**Software**
Inline Dip	AASPI
Crossline Dip	AASPI
Dip Magnitude	AASPI
Dip Azimuth	AASPI
GLCM Contrast	AASPI
GLCM Dissimilarity	AASPI
GLCM Homogeneity	AASPI
GLCM Energy	AASPI
GLCM Entropy	AASPI
GLCM Mean	AASPI
GCLM Correlation	AASPI
Positive Principal Curvature	AASPI
Negative Principal Curvature	AASPI
Strike of Positive Principal Curvature	AASPI
Srike of Negative Principal Curvature	AASPI
Minimum Curvature	AASPI
Maximum Curvature	AASPI
Gaussian Curvature	AASPI
Dome	AASPI
Saddle	AASPI
Ridge	AASPI
Valley	AASPI
Bowl	AASPI
Shape Index	AASPI
Structural curvedness	AASPI
Rotation about Normal	AASPI
Reflector Convergence Magnitude	AASPI
Reflector Convergence Azimuth	AASPI
Positive Amplitude Curvature	AASPI
Negative Amplitude Curvature	AASPI
Strike of Positive Amplitude Curvature	AASPI
Strike of Negative Aplitude Curvature	AASPI
Gaussian Amplitude Curvature	AASPI
Mean Amplitude Curvature	AASPI
Dome (Amplitude)	AASPI
Ridge (Amplitude)	AASPI
Saddle (Amplitude	AASPI
Valley (Amplitude)	AASPI
Bowl (Amplitude)	AASPI
Amplitude Shape Index	AASPI
Amplitude Curvedness	AASPI
Peak Frequency	AASPI
Peak Phase	AASPI
Peak Magnitude	AASPI
Peak Magnitude Above Average	AASPI
Total Energy	AASPI
Coherent Energy	AASPI
Aberrancy Toatal Azimuth	AASPI
Aberrancy Maximum Azimuth	AASPI
Aberrancy Minimum Azimuth	AASPI
Aberrancy Interval Azimuth	AASPI
Energy Ratio Similarity	AASPI
Outer Product Similarity	AASPI
Sobel Filter Similarity	AASPI
Inline Energy Gradient	AASPI
Crossline Energy Gradient	AASPI
First Derivative	Petrel
Second Derivative	Petrel
Relative Acoustic Impedance	Petrel
Sweetness	Petrel
Apparent Polarity	Petrel
Cosine Phase	Petrel
Envelope	Petrel

Table 1. List of seismic attributes considered for the neural networks.

Neural Networks and Self Organizing Maps

A neural network is a statistical prediction tool that many geoscientists have utilized for predicting reservoir properties (e.g. Cersòsimo et al., 2016, Konaté et al., 2014, Lashin et al., 2012 etc.). Artificial Neural Networks (ANN) were first introduced in 1943 by Warren McCulloch and Walter Pitts who used electrical circuits to model how neurons in the brain operate (van der Baan, 2000). ANN applications to geophysics did not take place until the late 1980's and early 1990's when the first papers were written about the role of neural nets in first break picking and trace editing (Russell, 2005). The basic elements of a neural network are layers of neurons (or nodes) which contain activation functions that find non-linear statistical relationships in the data. As input data passes through the network, weights are applied that connect each node to the next in order to find the right contribution of each element to the output. This generalized structure is well demonstrated by the traditional multilayer feed forward network (MLFN) (Figure 17) which contains an input layer, an output layer, and one or more hidden layers (Hampson et al., 2001). Many different types of artificial neural networks exist, which can be divided based on the type of problem they attempt to solve and the fashion in which they are trained (Russell et al., 2003).

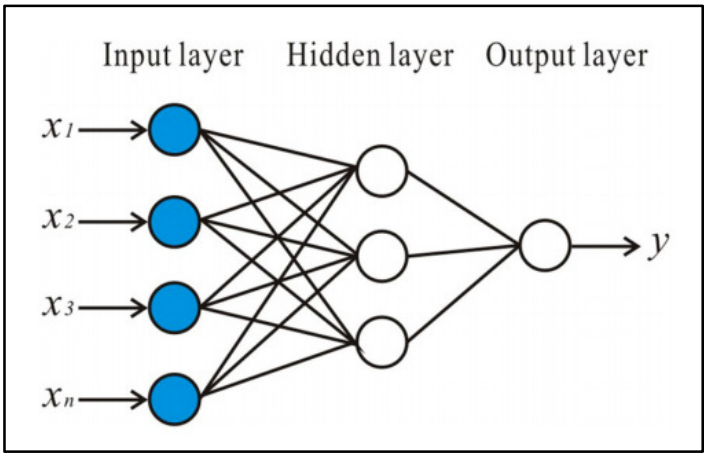

Figure 17. Standard neural network architecture with inputs x_1-x_n feeding into hidden layer nodes and then to our output node (y). (After Konaté et al., 2014).

Two types of problems commonly addressed using neural networks are prediction and classification. In a classification type network the user provides an input sample which is assigned to one of several output classes (Russell et al., 2003); in geoscience, this type of network is often used in lithologic classification in which the output classes consist of different facies (e.g. sand, shale, limestone). Prediction problems make use of statistical relationships to assign a specific property value to the output (e.g. porosity, impedance, etc.) (Russell et al., 2003).

Another important aspect of neural networks is their ability to be trained. A neural network "learns" in one of two ways: supervised or unsupervised. A supervised neural net requires human interaction in a training process where the user provides expected output values to help the neural network learn the relationships between input data and the known results at specific locations. A neural network is considered to be trained, meaning it has developed the appropriate weights, determined the optimal contribution of each input, and arrived at an accurate estimation of the given output data. At this point the ANN is able to apply that learned association to the entire data

set. Unsupervised methods include Self Organized Mapping (SOM), K-Means clustering and other statistical methods which do not require training on known data points but instead employ identification of trends based on clustering of data clouds in multi-dimensional vector spaces. The focus of this study utilizes both unsupervised SOM to investigate facies and architectural elements of the Oliver, as well as supervised Radial Basis Function Neural Network (RBFN), Probabilistic Neural Network (PNN), and Multilayer Feed-forward Network (MLFN) algorithms to predict the porosity of the Oliver sandstone. Multiple seismic attributes are used as inputs for the SOM and ANN algorithms but the attributes are utilized in different ways between the two methods. For ANN, the basis of the training method is built upon the relationship between several seismic attributes and the porosity logs at well locations (Figure 18). During the training process the neural network will work to reduce the error between its output (i.e. the weighted combination of the seismic attribute values at those well locations) and the actual porosity values of the well logs. Once the error is reduced to an acceptable threshold the training is complete and the next step is to feed the network the suite of seismic attributes over the entire seismic volume (constrained to our zone of interest in the time domain) which will yield our porosity volume for the Oliver Sandstone.

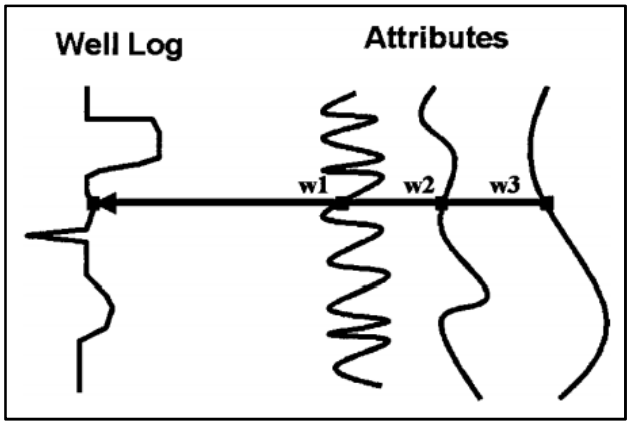

Figure 18. Conceptual drawing showing how the weighted set of input attributes can be related to the target well log (Hampson et al., 2001).

Self-Organized Maps (SOM)

Self-organized maps, developed by Teuvo Kohonen (Kohonen, 1982), translate multiple data inputs into an *n*-dimensional vector space where clusters of data are classified by models or prototype vectors which have similar input vectors (Figure 19) (Kohonen, 2013). These prototype vectors are organized by a lower-dimensional (2D) latent space (Wallet et al., 2009) where each model or SOM node and its neighbors are updated based on a minimum distance computation outlined by Kohonen (2001). The end result is a map that represents several attributes at once. If implemented correctly SOM can provide superior interpretational value compared to looking at individual attributes. Much of the work done with SOM shows its value as a facies classification tool (Zhao et al., 2016).

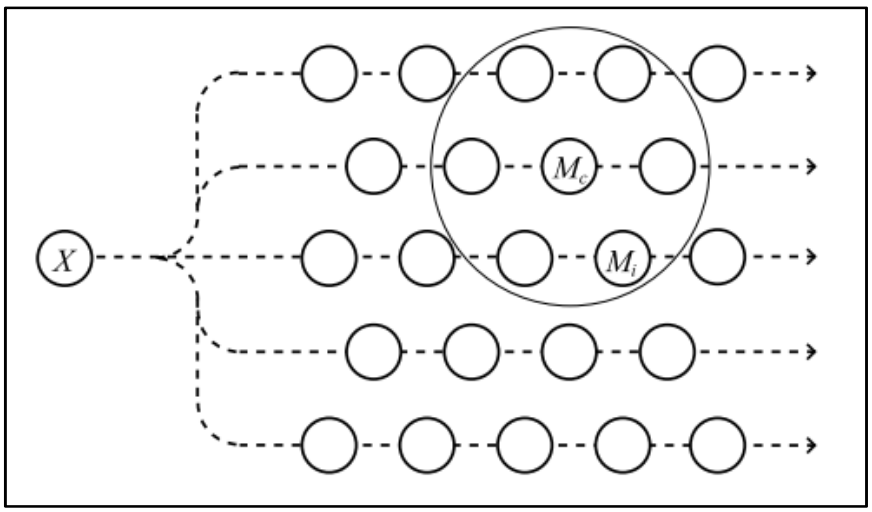

Figure 19. Image from Kohonen (2013) displaying the conceptual SOM architecture. The input X is mapped to a best matching prototype vector (M_c). Neighboring nodes (M_i) that lie within the neighborhood (larger circle) are updated.

Multilayer Feedforward Neural Networks (MLFN)

Multilayer Feed Forward Networks, also referred to as Back Propagation Networks, are one of the most popular forms of neural nets. These networks calculate the error between predicted values and the desired values of the training set. This error is then iteratively back propagated though the network to adjust the weights until the error between the training data and the predicted network outputs is minimized (Walls et al., 2002). The method of backpropagation is a form of gradient descent and has the flaw of slow convergence and being prone to getting stuck in local minima. Newer methods for error minimization show that the process is best handled by a scaled conjugate gradient approach (van der Baan, 2000), simulated annealing (Hampson et al., 2001), or the Levenberg–Marquardt algorithm (LMA) (Konaté et al., 2015). These methods guarantee convergence of the network to an error minimum within a certain number of iterations which improves the speed and reliability of the computation.

Radial Basis Function Neural Networks (RBFN)

Radial Basis Function Neural Networks (closely related to Generalized Regression Neural Networks) are a single pass neural network where the weights of the inputs are not iteratively recalculated as in the back propagation technique. Instead, they are pre-computed using a matrix inversion of Gaussian Basis Functions weighted by the training values (Russell et al., 2003). Once the weights are determined they are applied to the resultant data to provide the final predicted dataset (Russell et al., 2003).

Probabilistic Neural Network (PNN)

The probabilistic neural network differs from the MLFN and RBFN in that is doesn't utilize hidden nodes and is actually a type of mathematical interpolation that is applied to the data using a neural network architecture (Hampson et al., 2001). For the PNN, the target log is considered to be a linear combination of the input attributes and the distance between the target and input points is scaled by a set of smoothing parameters until the result reaches the lowest validation error (Hampson et al., 2001).

Statistics

Making statistically relevant correlations of depth-related data (i.e. mud losses) to seismic properties can be a challenge due to the need for a time-depth relationship to map the two data sets into the same domain. Once the time-depth relationship is determined we need a way to analyze the attribute values over the zone of interest. To solve this problem I implement the Cigar Probe module in AASPI, where I input deviation surveys for my mud loss wells, sampled in time rather than depth; this way I can leave all of my attributes in time. With my wells converted to the time domain I can simply take an attribute, define my interval of interest with horizons (i.e. Oliver Top

and Oliver maker), and the cigar probe will extract a set of statics (weighted average, weighted median, and weighted percentile) quantifying the attribute along the borehole using a distance-weighted scheme. The number of samples incorporated into the statistics is based on the sample interval in the depth/time domain and the radius of investigation. For my analysis I set the radius to 110 feet (i.e. one bin) giving me a neighborhood of 5 traces, and I provide a deviation point every 2 ms giving me a ~25 ft sample rate. All correlations involving seismic attributes, including the generated porosity volume, utilized these same parameters.

Chapter 5: Analysis

Hypothesis 1: Channels

A potential cause for the mud losses in the Oliver is that the wellbores are drilling through sand-filled channels. Examining Figure 20 note that several channels are well-imaged in the western portion of the study area. Small feeder channels are visible and can be tracked until their confluence with the larger fluvial complex that ultimately flows out into a delta deposit. Figure 21 shows the well-developed lobe shape of the delta which implies an absence of strong littoral currents during Oliver deposition that would otherwise have oriented the delta parallel to depositional strike (Coleman 1975). This indicates that the Oliver is not a wave dominated delta environment. Additionally, the lobate geometry is much different than the depositional model for a tidally dominated system as shown in Figure 22, suggesting that Oliver is a fluvial-dominated system. The high tidal ranges experienced by tidally-dominated deltas typically produce sand filled channels (Coleman 1975) whereas those environments that have low tidal ranges (i.e. fluvial dominated) normally have clay filled channels. Looking at the impedance extracted along the Oliver horizon in Figure 23, the impedances of the channels are slightly higher than that of the surrounding coastal plain, indicating higher density mud fill, corroborating the geologic reasoning from Coleman (1975). Although the spatial extent of the channels in the west is well defined, the channel features in the east are less clear. One cause for this is that channels can be seismically "invisible" due to low impedance contrast with surrounding units and thicknesses that are below tuning (Barber, 2010).

Reexamining Figure 23, the impedance contrast in the east is much lower, with only discontinuous pieces of channels identifiable. Drawing a seismic cross section through the high-loss-volume wells gives a better interpretation than looking at the horizon slice (Figure 24). The mud loss wells have no visual correlation to the presence of channels although detailed modeling could be done on the eastern side of the survey to try and identify channel responses near the problematic wells.

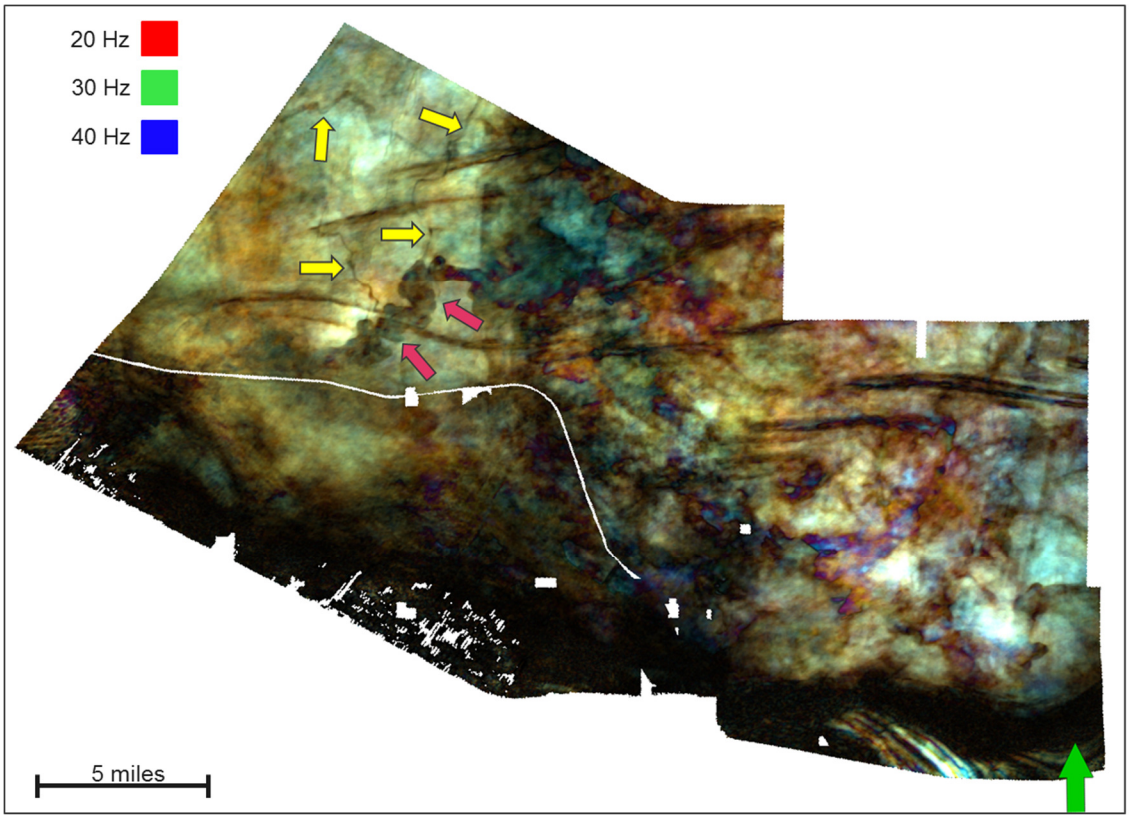

Figure 20. RGB co-blend of 20 Hz, 30 Hz, and 40 Hz spectral magnitude components. The decomposition window ranged from 20 ms above to 30 ms below the Oliver Top. Yellow arrows indicate small tributary channels feeding into the larger fluvial complex highlighted by the pink arrows.

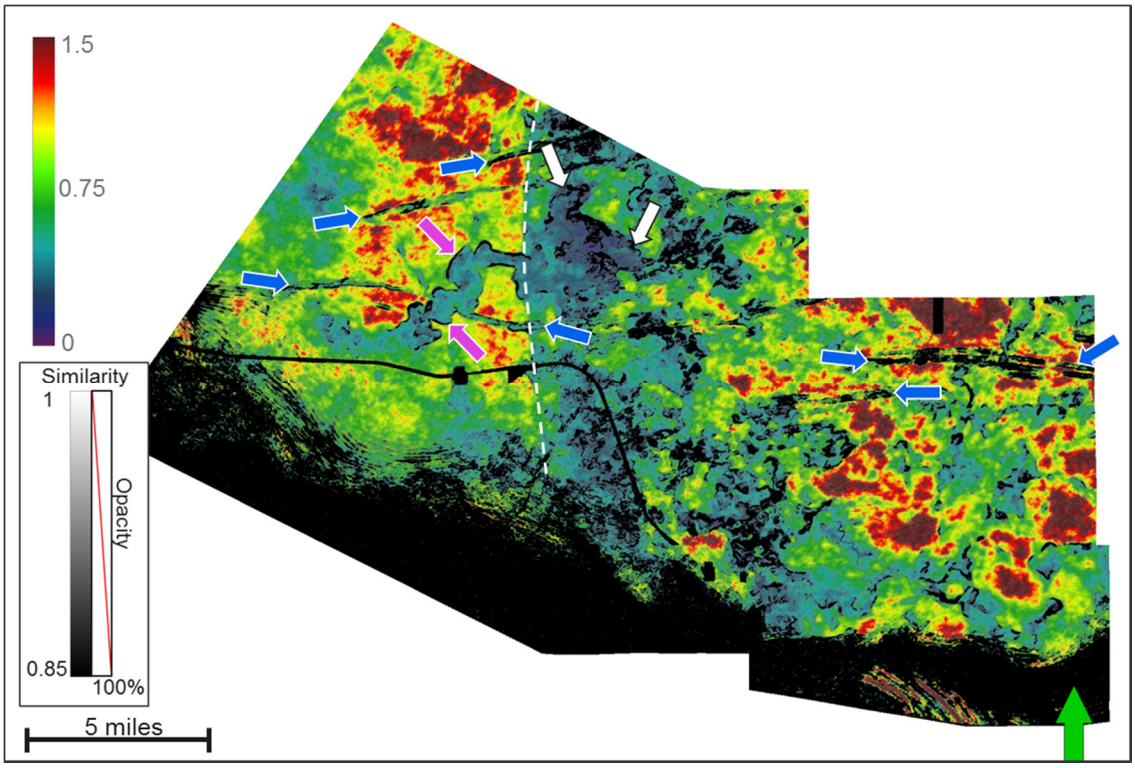

Figure 21. Horizon slice at the Oliver Interval through sweetness volume. Blue arrows indicate wrench faults, pink arrows indicate a large fluvial system in the western portion of the survey, and white arrows indicate slumping features off the distal edges of the delta deposit. A sharp break between the coastal plain environment and the shoreface is highlighted by the white dashed line.

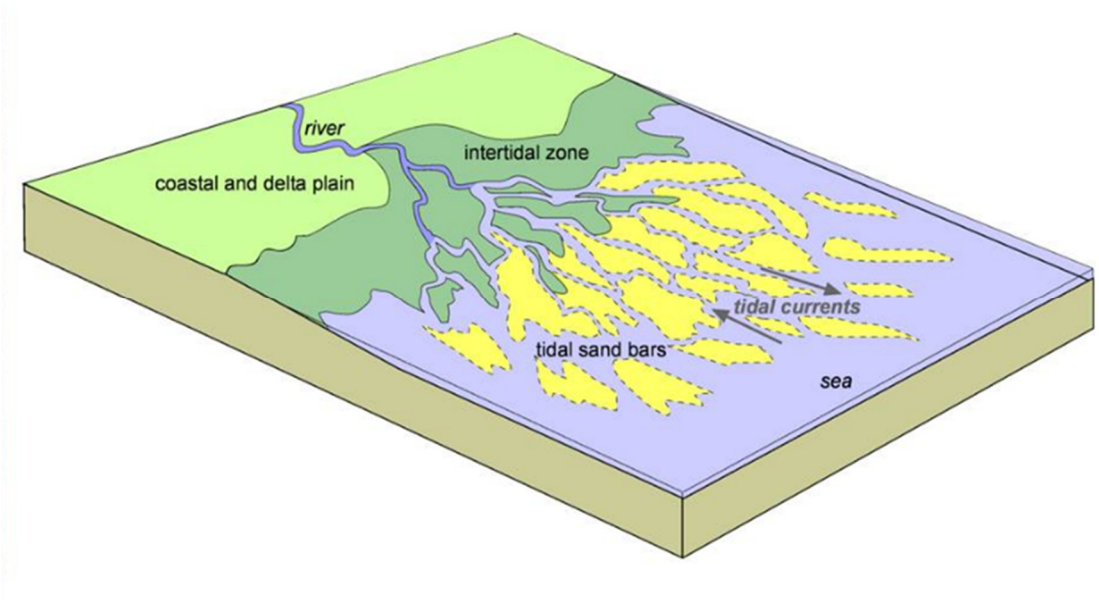

Figure 22. Conceptual animation of a tidally dominated delta that has many different sand bars broken up by tidal currents and a large intertidal zone separating this from the coastal plain (Nichols, 2009). This contrasts greatly with the seismic images we have and confirms that the Oliver is not tidally dominated.

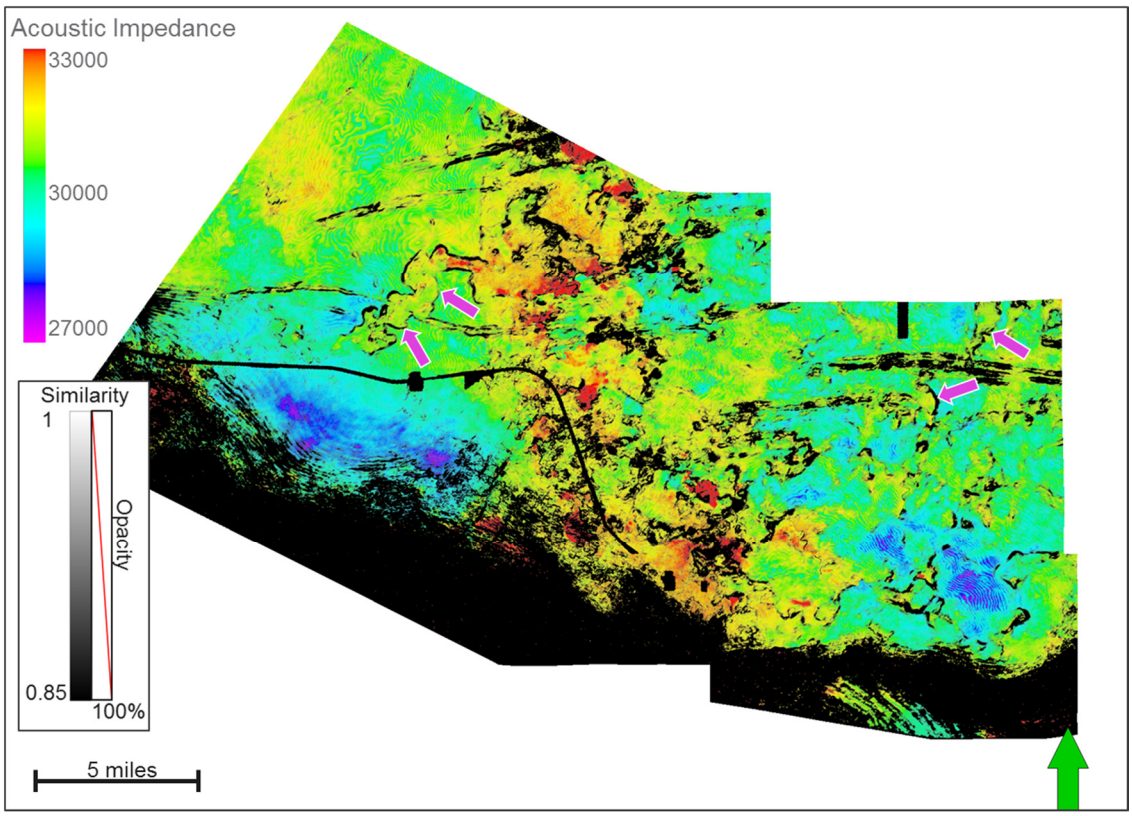

Figure 23. RMS extracted impedance with a +/-10ms window around the Oliver Top. Pink arrow indicate the higher impedance of the channels which means they may be more dense mud-filled channels, and thus do not pose a drilling risk.

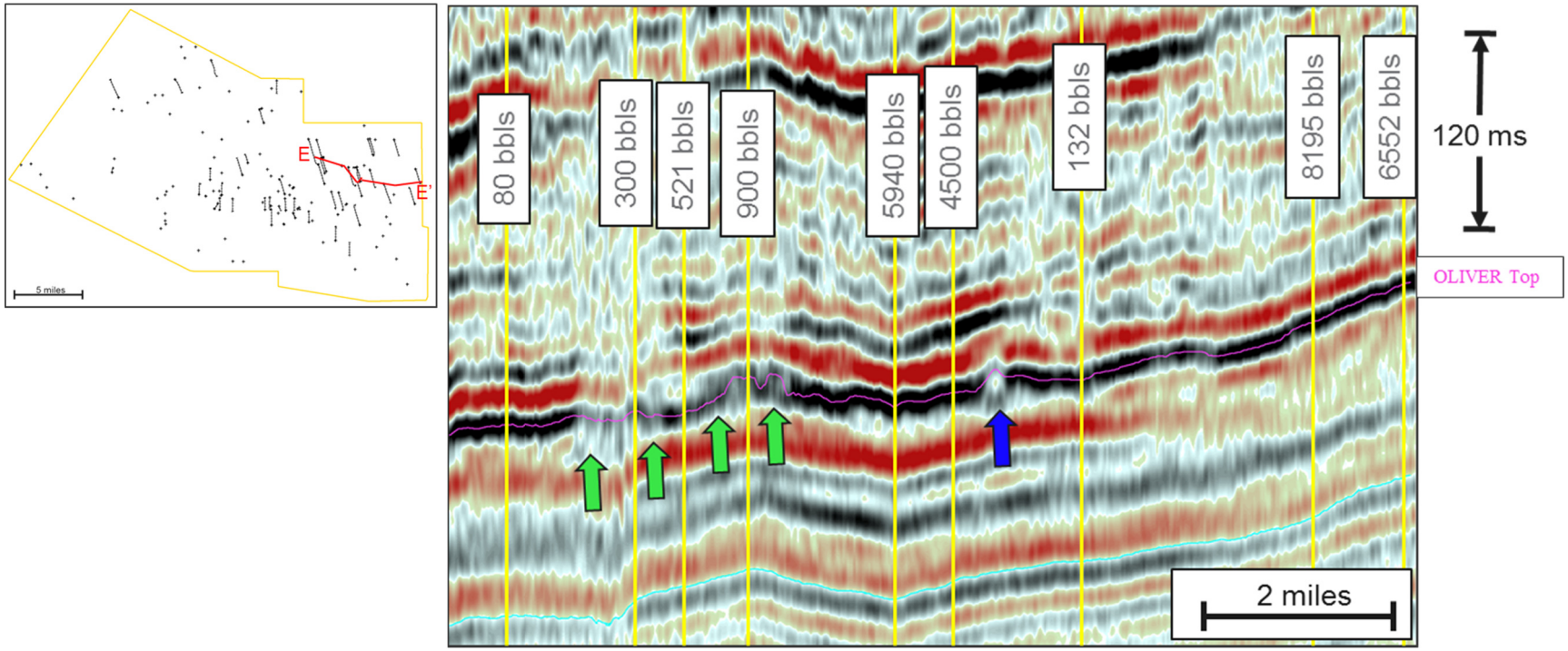

Figure 24. Yellow lines represent the locations of wells that experienced losses with the volume lost for each well posted on the wellbore. The blue arrow indicates a channel feature while the green arrows indicate disruptions of the reflector from wrench faulting. It appears that none of the high loss wells are drilled into a channel feature but the two wells just left of the channel did lose a large amount of mud. From this I conclude that the losses are not impacted by channels, although we cannot rule out a channel contribution for every well.

Hypothesis 2: Porous Zones in the Oliver

Porosity is a second potential cause of losses within the Oliver Sandstone. Studies have shown that if the pore size is more than three times larger than the mud particles, the probability of experiencing losses increases (Rahman, 2010). The coarsening upward motif of the Oliver sandstone is a prime candidate for larger grain and pore size, especially near the top of the maximum regressive surface. To investigate porosity of the Oliver, the acoustic impedance volume is used in a neural network with other attributes to generate a porosity volume over the zone of interest (Appendix B). The results show high porosity zones (>16%) throughout the area and characterize channels as exhibiting lower porosity (~10%) (Figure 25) confirming the impedance results. Extracting weighted average porosity values from the Oliver gross interval and cross plotting against loss volume (Figure 26) shows no correlation. Cross plotting P-wave impedance with mud losses provides no significant correlation and confirms that the poor correlation with porosity is not simply due to errant prediction by the neural network (Figure 27).

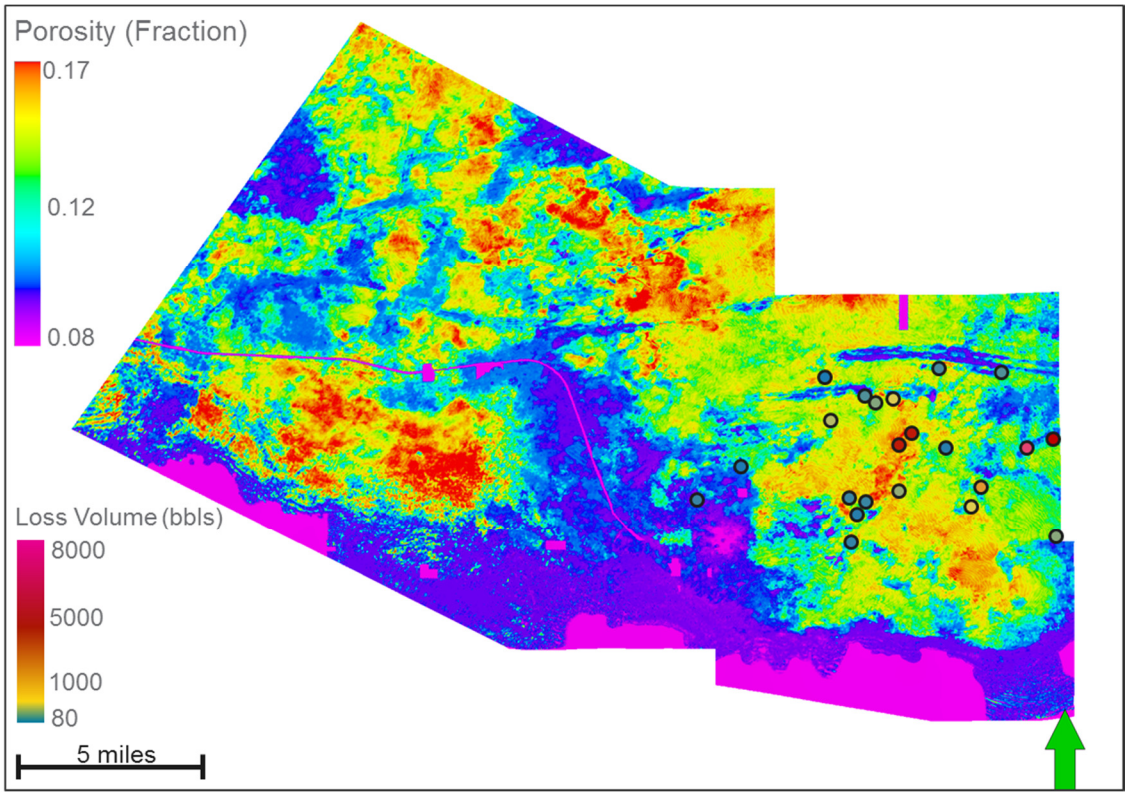

Figure 25. RMS porosity from the neural network prediction, using a +-5 ms window around the Oliver top.

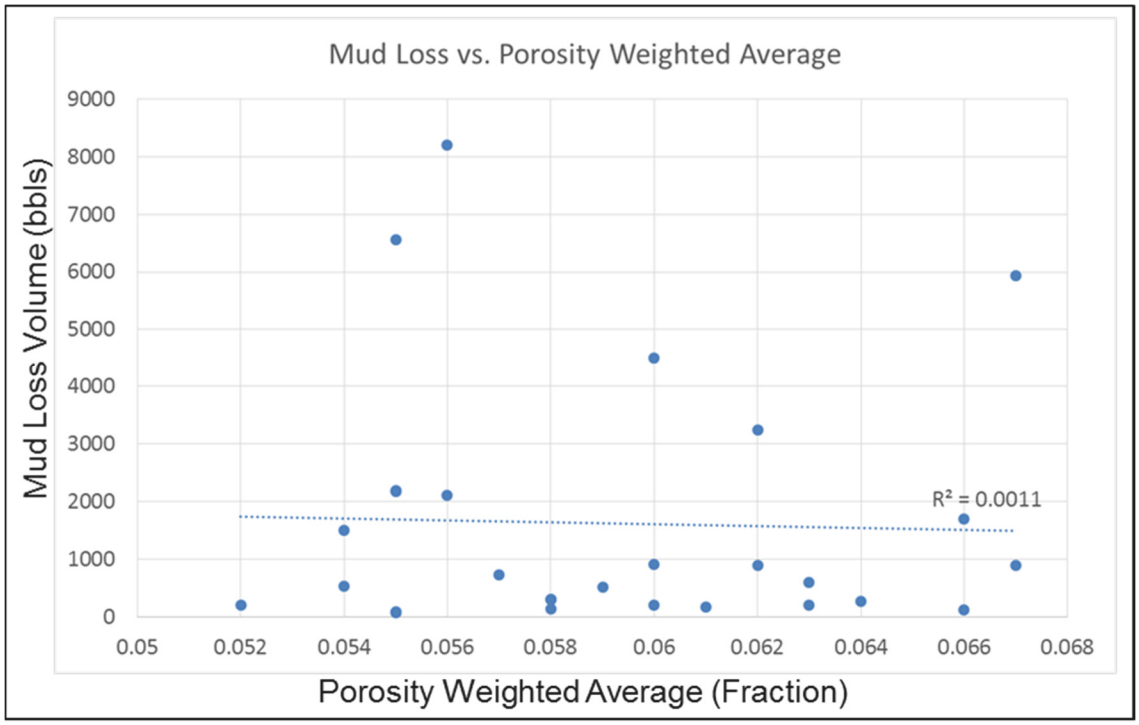

Figure 26. This figure displays the extremely poor correlation between mud losses and porosity over the Oliver interval.

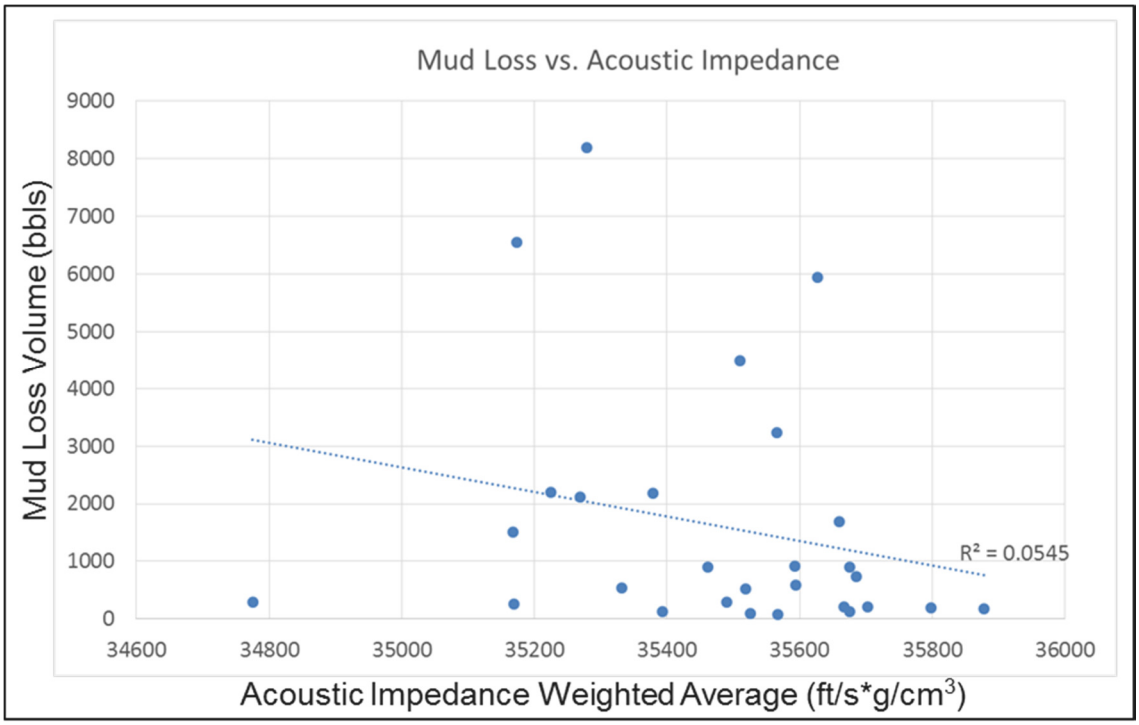

Figure 27. Cross plot of the weighted average impedance against the mud loss volume. No correlation exists between mud loss and impedance which reaffirms the bad correlation with porosity.

Hypothesis 3: Proximity to Faults and Flexures

Regions of faulting or fracture enhanced permeability have been associated with some of the most costly instances of mud losses in other basins (Rahman, 2010). Certain characteristics of mud loss rate over time can indicate if the mud losses experienced are fracture induced. For example, Rahman (2010) states that initially, drilling mud invasion into empty natural fracture will be rapid, causing the mud loss rate to spike. As the fractures fill, leak-off of the mud filtrate through fracture walls increases the mud viscosity, which subsequently damages the permeability of the formation and decreases the rate of loss (Rahman, 2010). Because we do not have this kind of data for our study, we will rely on visual and statistical correlations to the structural attributes. Plotting losses on a curvature map reveals that although some of

the lower loss volumes are in proximity to structurally deformed areas they do not show any strong trend with the overall losses or the associated volumes (Figure 28). To obtain a more quantitative correlation, I use the Cigar probe to output the distance weighted average of most negative curvature around the wellbore in the Oliver. This plot in Figure 29 exhibits a very weak correlation and is insignificant compared to the trend I am trying to identify. To investigate other structural features, the cigar probe calculation is executed on both the structural shape index attribute as well as the energy ratio similarity. The shape index results in Figure 30 have a low R^2 but I interpret two negative correlation trends, one for the higher volume losses and another for intermediate losses (>1,000 bbls and <5,000 bbls). The lowest loss volumes (<1,000 bbls) have no trend with the shape index. The energy ratio similarity has no correlation to the losses and affirms that the losses are not caused by any discrete discontinuities such as faults (Figure 31).

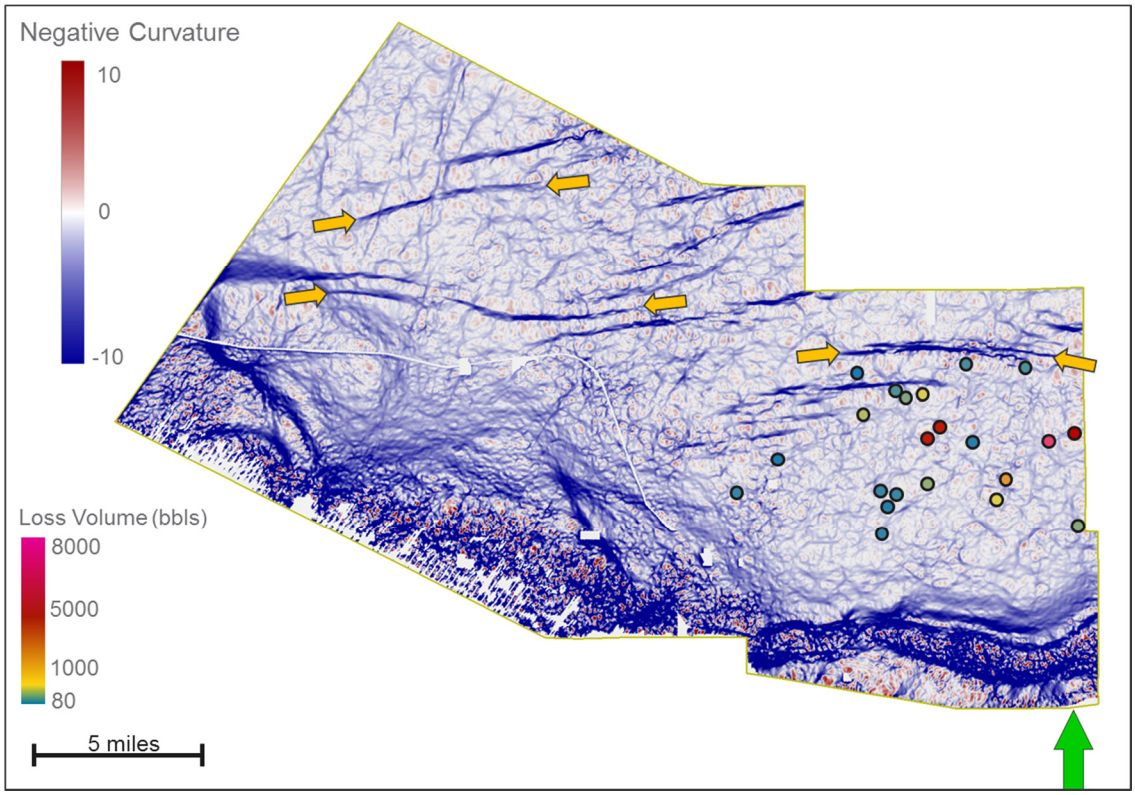

Figure 28. Negative curvature map extracted at the Oliver Top. Orange arrows indicate several of the wrench faults. Colored circles represent wells that experienced mud losses. There is no visual correlation between the losses and proximity to flexures. Although some losses are seen near the wrench faults a majority of them are not located near any major flexure.

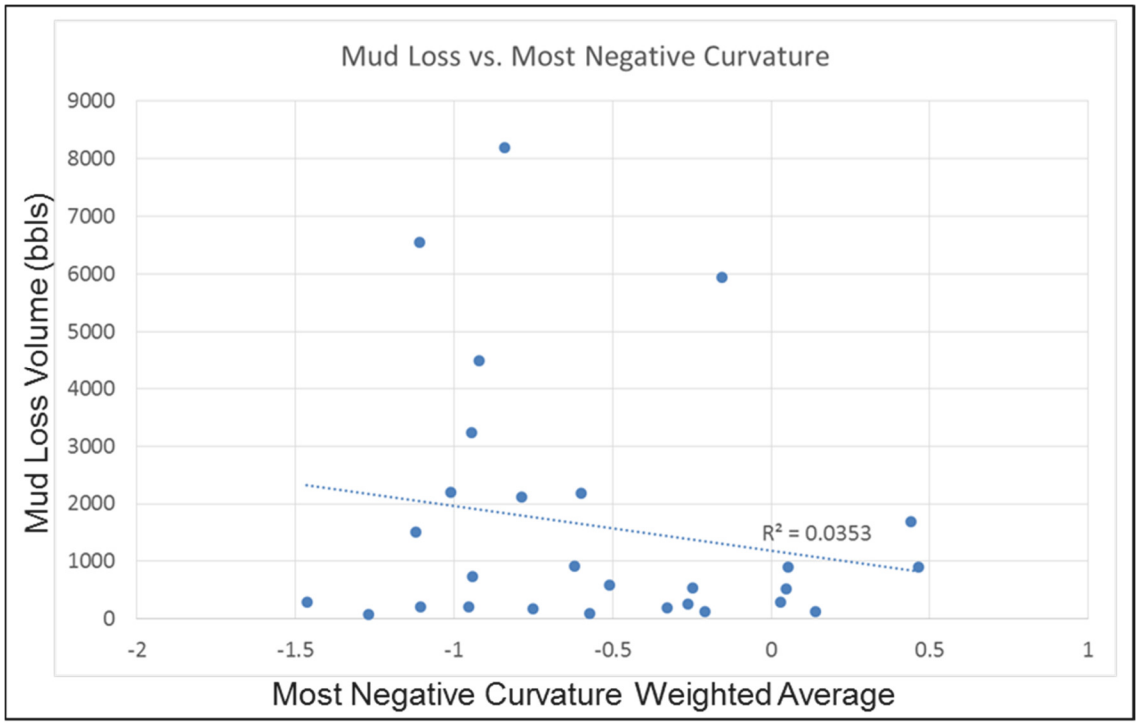

Figure 29. This figure shows no statistical correlation between negative curvature in the Oliver and mud losses which corroborates our visual inspection.

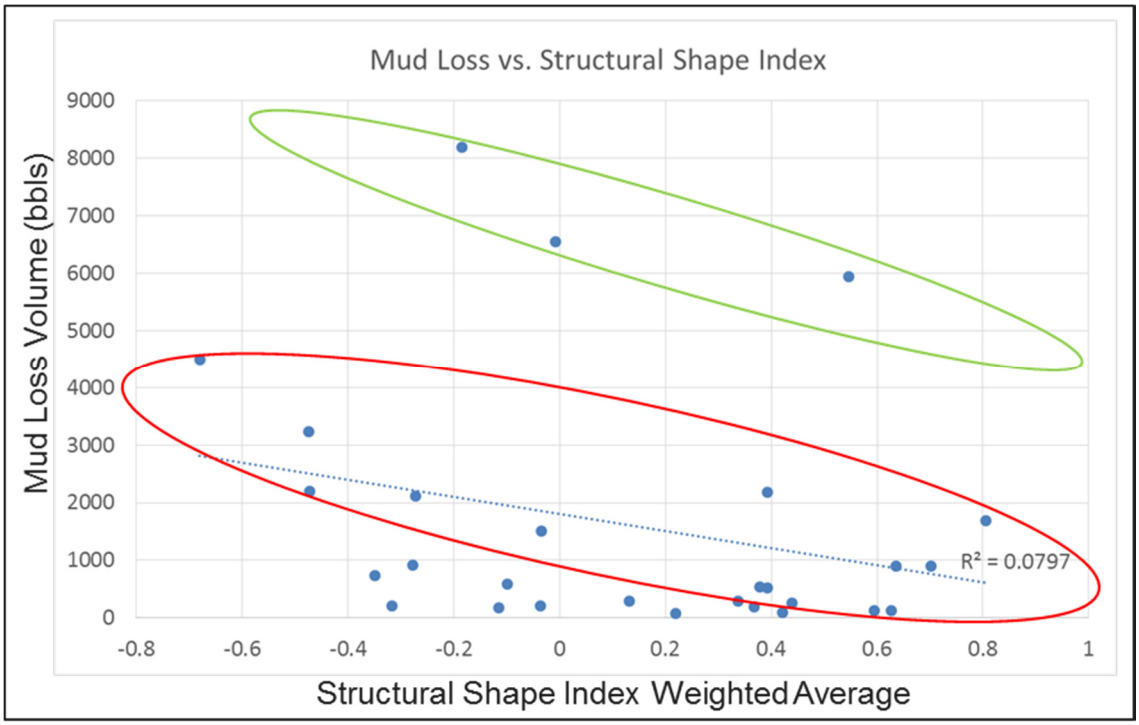

Figure 30. Cross plot between mud loss and shape index. Although the correlation is low there are some trends to the high (>5,000 bbls) and intermediate (>1,000 bbls) loss volumes.

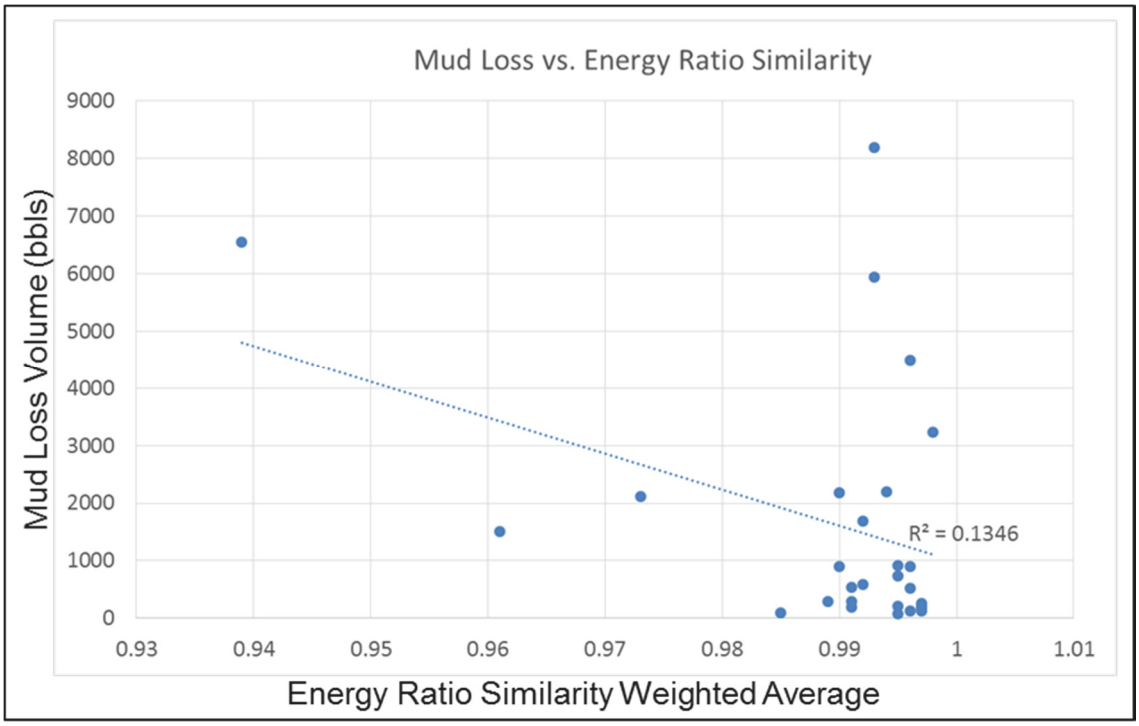

Figure 31. Cross plot between Energy ratio similarity and mud loss volume. Even though the R^2 value is much higher, this correlation is very poor. All the data clustered below 1,000 bbls and between 0.99 and 1 similarity is causing the correlation to be artificially high.

Hypothesis 4: Problematic Layers in the Oliver

Initial examination of the stratigraphy suggests that the location of losses on the east side of the survey may correlate with the development of an additional progradational wedge above the Oliver 500 (e.g. equivalent to Oliver 600) as seen in Figure 32. Cross plotting the isopach thickness with the mud loss volumes at well locations yields the best correlation so far. Although the R^2 isn't a particularly strong correlation (even with an exponentially fitted trend line, Figure 33) upon closer inspection it appears that there maybe two trends to the data, possibly associated with two geologic facies. Recall that there was no correlation of losses with curvature, even when limiting the analysis to the higher loss wells. In an effort to improve the

correlation with the upper isopach thickness, I multiply the map by the RMS extracted porosity map to arrive at a PHIH (porosity*thickness) map (Figure 34). Cross plots of the mud losses against PHIH only marginally improve the correlation from the original isopach (Figure 35). Addtionally, SOM results cataloged in Appendix C provide further evidence of the development of the Oliver 600 in the east and its seismic response in the facies classification.

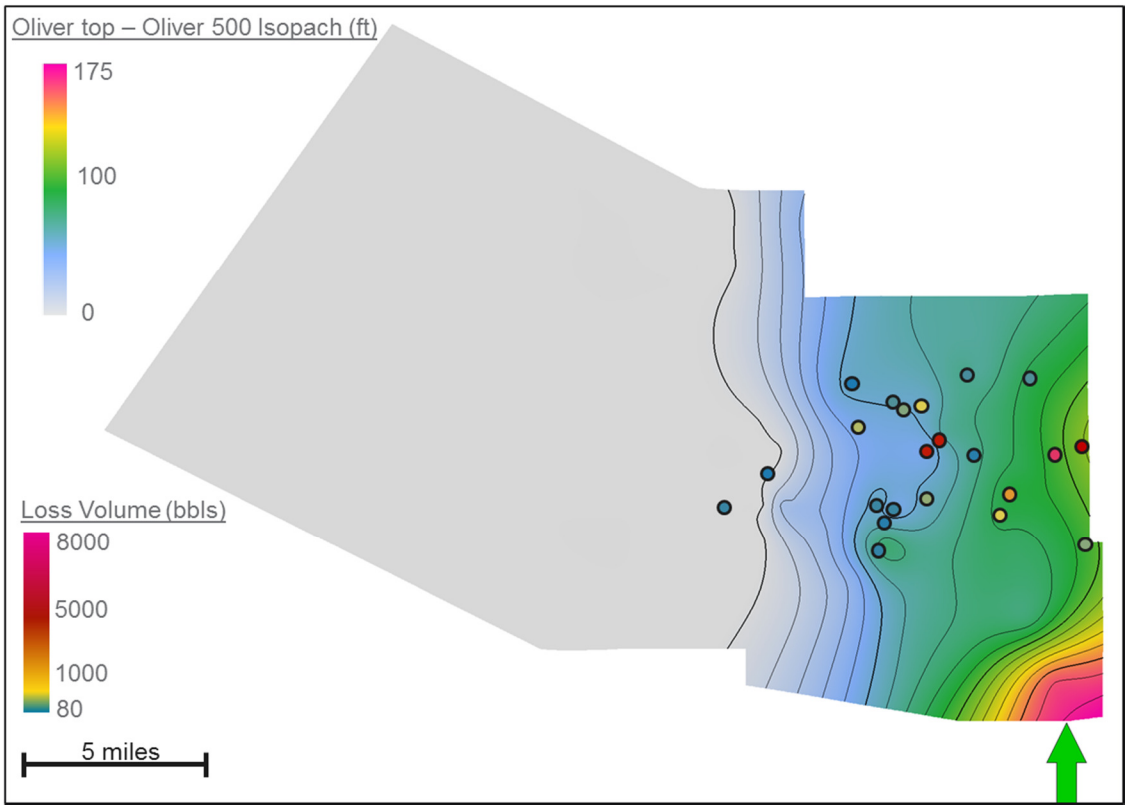

Figure 32. Isopach thickness from the Oliver Top to the Oliver 500, plotted with loss volumes. Not only do the mere occurrence of losses correlate well with the presence of this upper sand package but there is also a visual correlation of greater mud loss with greater thickness to the east.

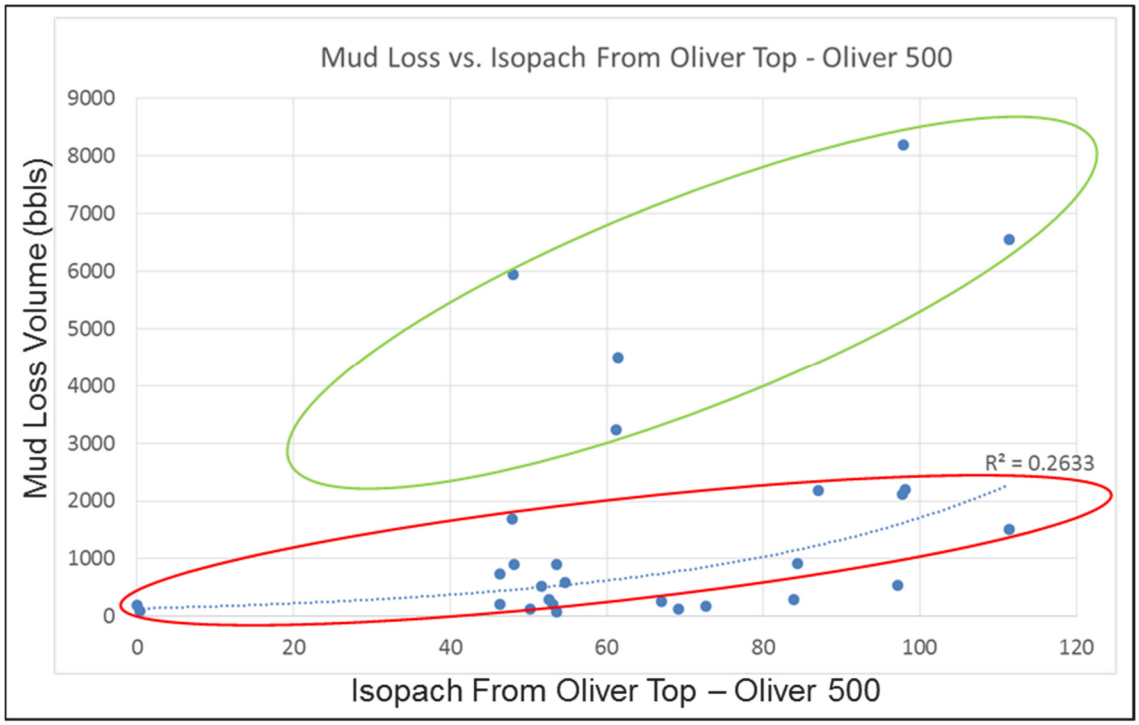

Figure 33. Cross plot of mud loss volume vs. isopach thickness of the Oliver top – Oliver 500 showing two potential trends in the data and revealing that the progradation of sands above the Oliver 500 have some correlation to the losses although it is weak.

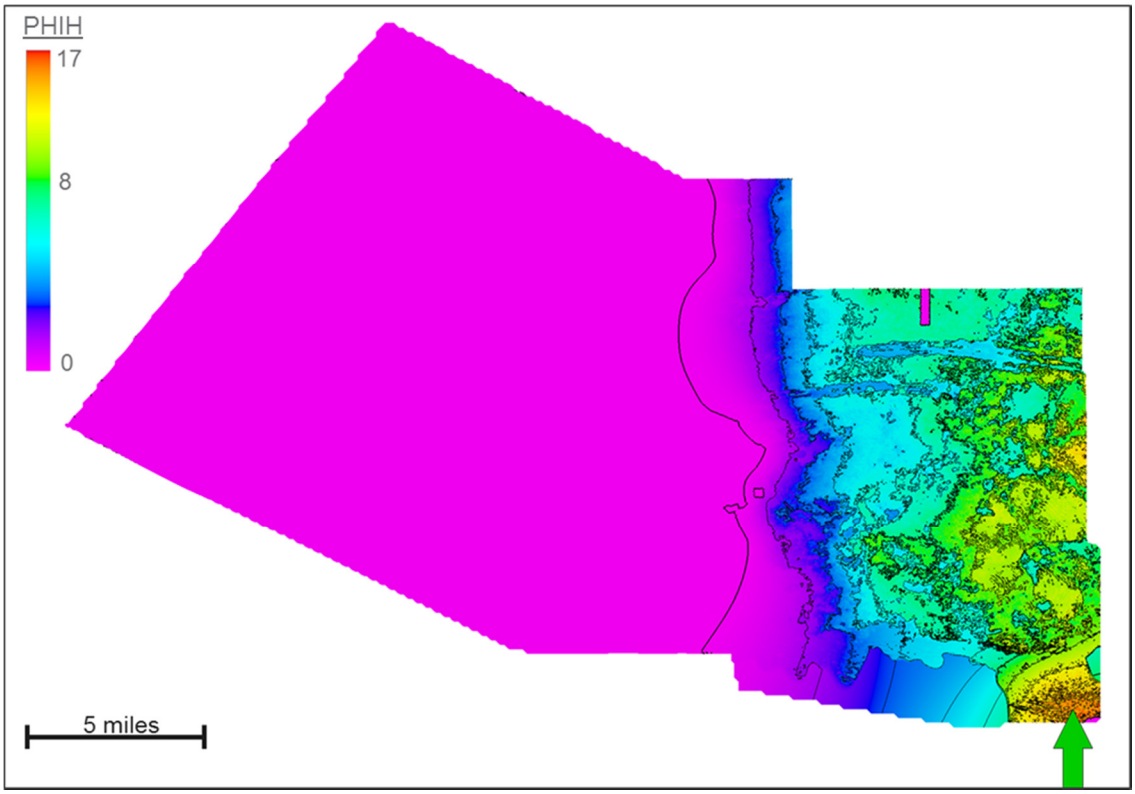

Figure 34. PHIH map calculated from the Oliver Top – Oliver 500 isopach and the RMS predicted porosity map in Figure 25.

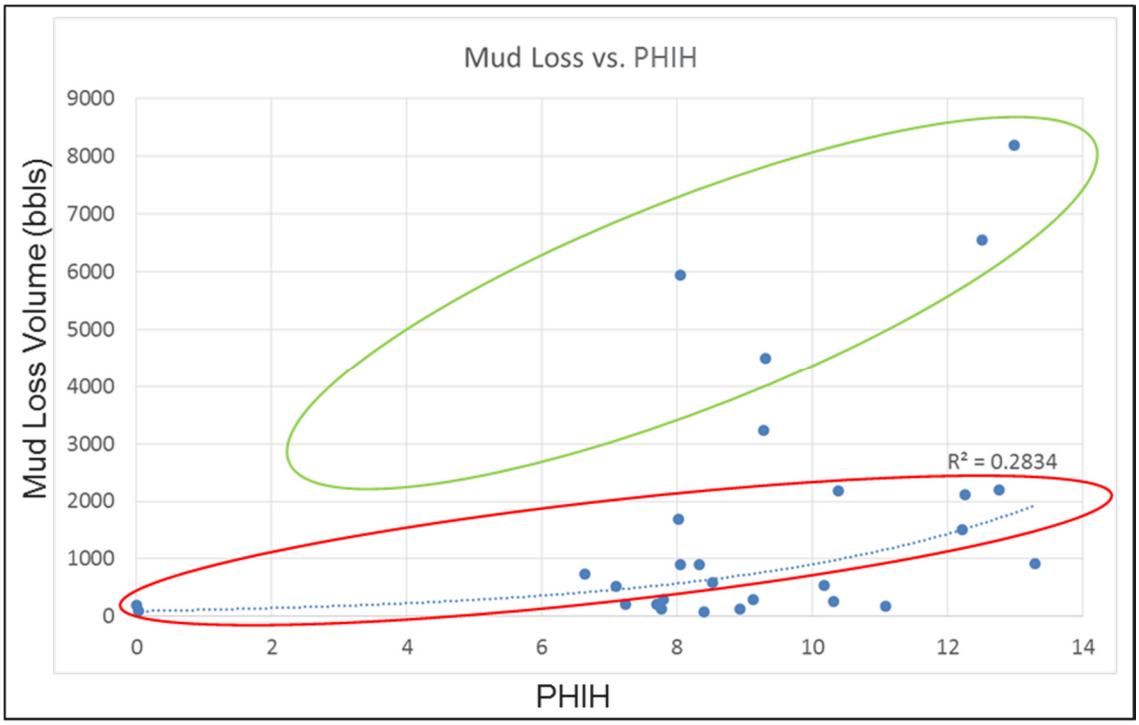

Figure 35. Correlation between PHIH and mud loss volume. The correlation improves slightly over the isopach but the same two trends are still identifiable.

Chapter 6: Discussion

Although no statistical correlation could be made between mud loss volume and seismic attributes or porosity, there is a compelling correlation to the development of the Oliver 600 sand which could be driving higher net-to-gross ratios in the region experiencing losses. Some complexities in the data may also be driving low correlations in the statistics. For example, even though mud losses are recorded at depths throughout the Oliver interval there is some reason to believe that the first instance of losses could be the driving force of all losses in the zone (e.g. if 50 barrels of mud is lost at 6000 ft then 50 more barrels is lost at 6500 ft, the second instance of losses may still be associated with the zone at 6000 ft since the borehole is still open to that formation). This theory would also suggest that mud losses recorded deeper than the Oliver, which have been associated with other problematic formations, could actually be losses originating in the Oliver but have been falsely attributed to another sandstone formations simply based on the bit depth. This could greatly skew our data, since in this study I only investigated mud loss volumes that were definitively attributable to the Oliver, and did not consider adding in deeper loss volumes. Caveats like this as well as variables that can effect mud loss volume such as drilling parameters (e.g. rate of penetration, drilling mud weight, use of lost circulation material, etc.), impart challenging uncertainty in the direct correlations of mud losses to geologic or geophysical phenomena. To avoid some of these issues, future analyses may involve breaking out the statistical comparisons into smaller zones (i.e. only looking at the Upper Oliver sand) instead of the entire Oliver interval. One consideration may be extracting attributes only at the exact depths of the recorded losses, but the

observational error in the recorded depth of the mud losses (i.e. lag time between the occurrence of the loss at depth and its response at the surface, misreporting, etc.) is not amenable to such analysis. Also, a majority of the basin development has taken place on the eastern side of the survey, thus increasing the probability of seeing losses in this area. Although the correlation between an *occurrence* of losses and Oliver 600 isopach may be coincidentally due to this disproportionate drilling across the study area, this still would not explain the delineation of two trends and the correlation to the volumes themselves.

Chapter 7: Conclusion

This study employs a neural network for porosity prediction but extends previous work by taking the prediction results and attempting to characterize a hazardous zone known as the Oliver Sandstone. Detailed information on the methodologies used to conduct this research show the contribution of each step of the process: using stratigraphy to develop initial relationships between log properties, conditioning seismic data to aid in visual interpretations, calculating attributes for structural interpretations as well as for inputs into the neural networks, executing the neural networks with differing structures and supervision methods to investigate their impact on the results, and ultimately using all these findings to draw a correlation between the sand deposition in the Oliver Sandstone and the mud losses that have been experienced while drilling. Thorough discussions of possible pitfalls, implications of results, and additional improvements are included to set out guidelines for continued work.

Neural network prediction of porosity and multi-attribute classification using SOM are useful techniques in analyzing the fluvial deltaic nature of the Oliver Sandstone. The inverted P-impedance volume correlates well with porosity logs and gives us reasonable confidence in the neural network generated porosity volume. SOM maps show how differing facies in the system may be classified in broad groups, providing additional interpretive value compared to other singular attributes. No correlations could be drawn between the mud losses and seismic attributes or porosity. In contrast, the stratigraphic work shows that there is a significant trend between the mud loss volumes and the isopach thickness of the Oliver 600 sand. This depositional

correlation is a prime candidate for future work and observation. Restricting our statistical analysis to the Oliver 600 zone may delineate the two trends we observe in the correlation and further work could be done researching the mud loss depths and grouping them in different ways to draw connections to more specific intervals.

References

Alsouki, M., R.Taifour, and O. Al Hamad, 2014, Delineating the fluvial channel system in the upper Triassic formation of the Elward Area in the Syrian Euphrates Graben using 3-D Seismic Attributes: Journal of Petroleum Exploration and Production Technology, v. 4, p. 123-132.

Aminzadeh, F., J. Barhen, C.W. Glover, and N.B. Toomarian, 2000, Reservoir parameter estimation using a hybrid neural network: Computers & Geosciences, v. 26, p. 869-875.

van der Baan, M.D., and C. Jutten, 2000, Neural networks in geophysical applications: Geophysics, v. 65, p 1032-1047.

Barber, R., 2010, Challenges in mapping seismically invisible Red Fork channels, Anadarko Basin, Oklahoma: M.S. Thesis, The University of Oklahoma.

Blackstone, D.L. Jr., 1988, Thrust faulting: Southern margin Powder River Basin, Wyoming: Thirty-Ninth Field Conference Wyoming Geological Association Guidebook, p.35-44.

Chopra, S., and K.J. Marfurt, 2007, Seismic Attributes for Prospect Identification and Reservoir Characterization, Tulsa, OK: Society of Exploration Geophysicists.

Cersósimo, D.S., C.L. Ravazzoli, and R.G. Martínez, 2016, Prediction of lateral variations in reservoir properties throughout an interpreted seismic horizon using an artificial neural network, The Leading Edge, v. 35, p. 265-269.

Chentouf, R., C. Jutten, M. Maignan, and M. Kanevsky, 1997, Incremental Neural Networks for Function Approximation, Nuclear Instruments and Methods in Physics Research Section A: Accelerators, Spectrometers, Detectors and Associated Equipment, p. 268-270.

Coleman, J.M. and L.D. Wright, 1975, Modern river deltas: variability of processes and sand bodies: AAPG Bulletin, v. 57, p. 99-149.

Dyman, T.S., E.A. Merewether, C.M. Molenar, W.A. Cobban, J.D. Obradovich, R.J. Weimer, and W.A. Bryant, 1994, Stratigraphic transects for Cretaceous rocks, Rocky Mountains and Great Plains regions: The Rocky Mountain Section SEPM, Mesozoic systems of the Rocky Mountain region, p. 365-392.

Eichkitz, C.G., J. Amtmann, and M.G. Schreilechner, 2013, Calculation of grey level co-occurrence matrix-based seismic attributes in three dimensions, computers & geosciences, v. 60, p. 176-183.

Hampson, D.P., J.S. Schuelke, and J.A. Quirein, 2001, Use of multiattribute transforms to predict log properties from seismic data, geophysics, v. 66, p. 220-36.

Hart, B.S., 2008, Channel detection in 3-D seismic data using sweetness: AAPG Bulletin, v. 92, p. 733-742.

Henderson, T., 1985, Geochemistry of ground-water in two sandstone aquifer systems in the northern Great Plains in parts of Montana and Wyoming: U. S. Geological Survey, Professional Paper, v. 1402-C, p. C1-C84.

Henson, H., and J.L. Sexton, 1991, Premine study of shallow coal seams using high□ resolution seismic reflection methods: Geophysics, v. 56, p. 1494-1503.

Iturrarán-Viveros, U., 2011, Smooth regression to estimate effective porosity using seismic attributes: Journal of Applied Geophysics, v. 76, p. 1-12.

Kohonen, T., 2013, Essentials of the self-organizing map: Neural Networks, v. 37, p. 52-65.

Kohonen, T., Self-organizing Maps, 2001, 3rd ed. Berlin: Springer.

Kohonen, T., 1982, Self-organized formation of topologically correct feature maps: Biological Cybernetics, v. 43, p. 59-69.

Konaté, A.A., H. Pan, N. Khan, and J.H. Yang, 2014, Generalized regression and feed-forward back propagation neural networks in modelling porosity from geophysical well logs: Journal of Petroleum Exploration and Production Technology, v. 5, p. 157-166.

Lashin, A., and S.S. El Din, 2012, Reservoir parameters determination using artificial neural networks: Ras Fanar Field, Gulf of Suez, Egypt: Arabian Journal of Geosciences, v. 6, p. 2789-2806.

Leite, E.P., and A.C. Vidal, 2011, 3D porosity prediction from seismic inversion and neural networks: Computers & Geosciences, v. 37, p. 1174-1180.

Lindsay, R., and R.V. Koughnet, 2001, Sequential Backus averaging: upscaling well logs to seismic wavelengths: The Leading Edge, v. 20, p. 188-191.

Matos, M.C., M. Yenugu, K.J. Marfurt, and S.M. Angelo, 2011, Channel delineation and chert reservoir characterization by integrated seismic texture segmentation and cluster analysis: 12th international congress of the Brazilian Geophysical Society, Rio De Janeiro, Brazil, 15–18 August 2011, p. 801-806.

Mullen, D. M., and Barlow and Haun, Inc., 1993, Powder River Basin (Section FS-1), in Hjellming, C. A., ed., Atlas of major Rocky Mountain gas reservoirs: New Mexico Bureau of Mines and Mineral Resources, Geological Survey of Wyoming, Colorado

Geological Survey, Utah Geological Survey, Barlow and Haun, Intera, and Methane Resources Group, Ltd., p. 70
Nichols, G., 2009, Sedimentology and Stratigraphy (2nd Edition). Chichester, UK ; Hoboken, NJ: Wiley-Blackwell.

Ogiesoba, O.C., 2010, Porosity prediction from seismic attributes of the Ordovician Trenton-Black River Groups, Rochester Field, Southern Ontario: AAPG Bulletin, v. 94, p. 1673-1693.

Pranter, M.J., M.F. Vargas, and T. L. Davis, 2008, Characterization and 3D reservoir modelling of fluvial sandstones of the Williams Fork Formation, Rulison Field, Piceance Basin, Colorado, USA: Journal of Geophysics and Engineering, v. 5, p. 158-172.

Pranter, M.J., and N. K. Sommer, 2011, Static connectivity of fluvial sandstones in a lower coastal-plain setting: an example from the upper Cretaceous Lower Williams Fork Formation, Piceance Basin, Colorado: AAPG Bulletin, v. 95, p. 899-923.

Rahman, H., 2010, Detection, mechanism and control of lost circulation in drilling: M.S. Thesis, Dalhousie University.

Russell, B.H., L.R. Lines, and D.P. Hampson, 2003, Application of the radial basis function neural betwork to the prediction of log properties from seismic attributes: Exploration Geophysics, v. 34, p. 15-23.

Russell, B., 2005, Neural network applications in geophysics: CSEG National Convention, p. 339-41.

Sun, L., X. Zheng, H. Shou, J. Li, and Y. Li, 2010, Quantitative prediction of channel sand bodies based on seismic peak attributes in the frequency domain and its application: Applied Geophysics, v. 7, p. 10-17.

Tiab, D., and E.C. Donaldson, 2004, Petrophysics - Theory and Practice of Measuring Reservoir Rock and Fluid Transport Properties (2nd Edition), p. 105-112.

Trappe, H., and C. Hellmich, 2000, Using neural networks to predict porosity thickness from 3D seismic: First Break, v. 18, p. 377-384.

Wallet, C. B., M. C. Matos, and J. T. Kwiatkowski, 2009, Latent space modeling of seismic data: An overview: The Leading Edge, 28, 1454-1459.

Walls, J.D., M.T. Taner, G. Taylor, M. Smith, M. Carr, N. Derzhi, J. Drummond, D. Mcguire, S. Morris, J. Bregar, and J. Lakings, Seismic reservoir characterization of a U.S. Midcontinent fluvial system using rock physics, poststack seismic attributes, and neural networks: The Leading Edge, v. 21, p. 428-436.

Xia, S., J. Liu, J. Deng, P. Li, Y. Ren, Y. Chang, Q. Li, and J. Liu, 2013, River channel sand body prediction by means of integrating well log and seismic attribute analysis in dense well patterns: A case study of the Eastern Beierxi Block in the Sabei Development Area of Daqing Oilfield, China: Arabian Journal of Geosciences, v. 6, p. 4607-4617.

Zhao, T., J. Zhang, F. Li, K.J. Marfurt, 2016, Characterizing a turbidite system in Canterbury Basin, New Zealand, using seismic attributes and distance-preserving self-organizing maps: Interpretation, v. 4, p. 79-89.

Appendix A: Petrophysics

All gamma ray logs were normalized using equation A1. Density and sonic logs also were despiked (Figures 36 and 37). I recalculated all density porosity logs using equation A2 to ensure consistency and tailor the log specifically for the Oliver interval. Density values for the Oliver are not well documented although quartz has been identified as a dominant constituent (Henderson, 1985) so I use the standard quartz density 2.65 g/cm^3 for the matrix density. In the case of the water density we use 10,000 ppm base on observations from a lab samples that yielded values between 8,000 and 12,000 ppm; this is in line with Henderson's study where he shows that water salinity values in the Oliver are in the range of 3000 ppm on a shallow flank of the northern part of the basin, but salinity will increase as you go deeper in the basin to the southwest, where our study area is located. Calculated porosities for both normalized and non-normalized density logs show that the there is little benefit to using the normalized set (Figure 9a-9c), and because we are investigating a large area (~320 sq. mi.) the non-normalized set is used to preserve any regional porosity trends due to the geology.

$$L_{ij} = \frac{MODE(\mu) - 2MODE(\sigma) + MODE(\sigma)}{\sigma_j \times (L_j - \mu_j + 2\sigma_j)} \quad \text{(A1)}$$

Where,
L_j = the value of the log j at sample i
σ_j = Standard Deviation of Lij in the analysis window
μ_j = Mean of Lij in the analysis window
MODE(σ) = The peak standard deviation of all logs
MODE(μ) = Mean mode of all selected logs

$$\phi_{calculated} = \frac{\rho_{ma} - \rho_{log}}{\rho_{ma} - \rho_{fl}} \quad \text{(A2)}$$

Where,
ρ_{ma} = the matrix density of the formation
ρ_{log} = the density value of the input log
ρ_{fl} = the density of formation fluid

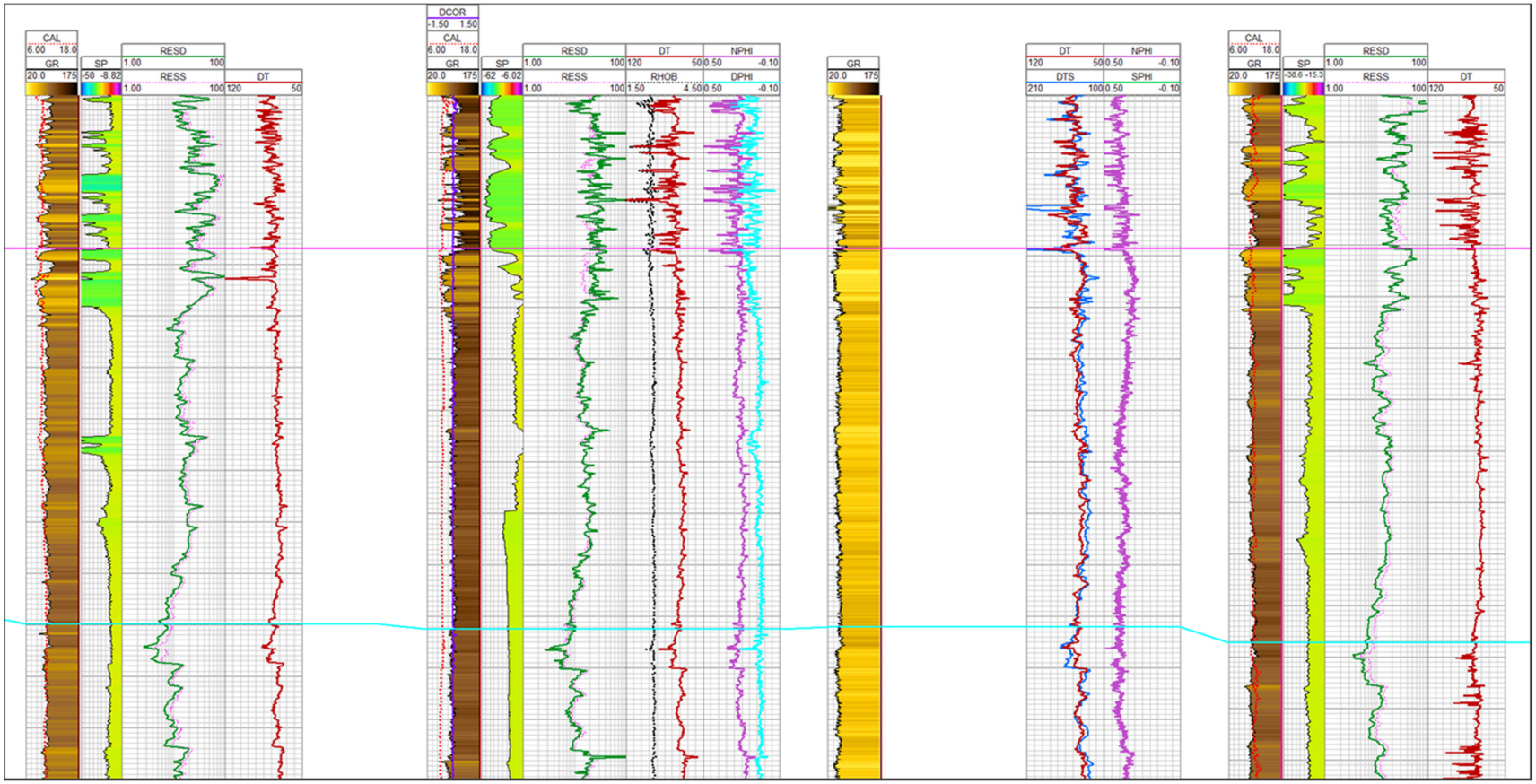

Figure 36. Set of four logs prior to despiking and normalization**.**

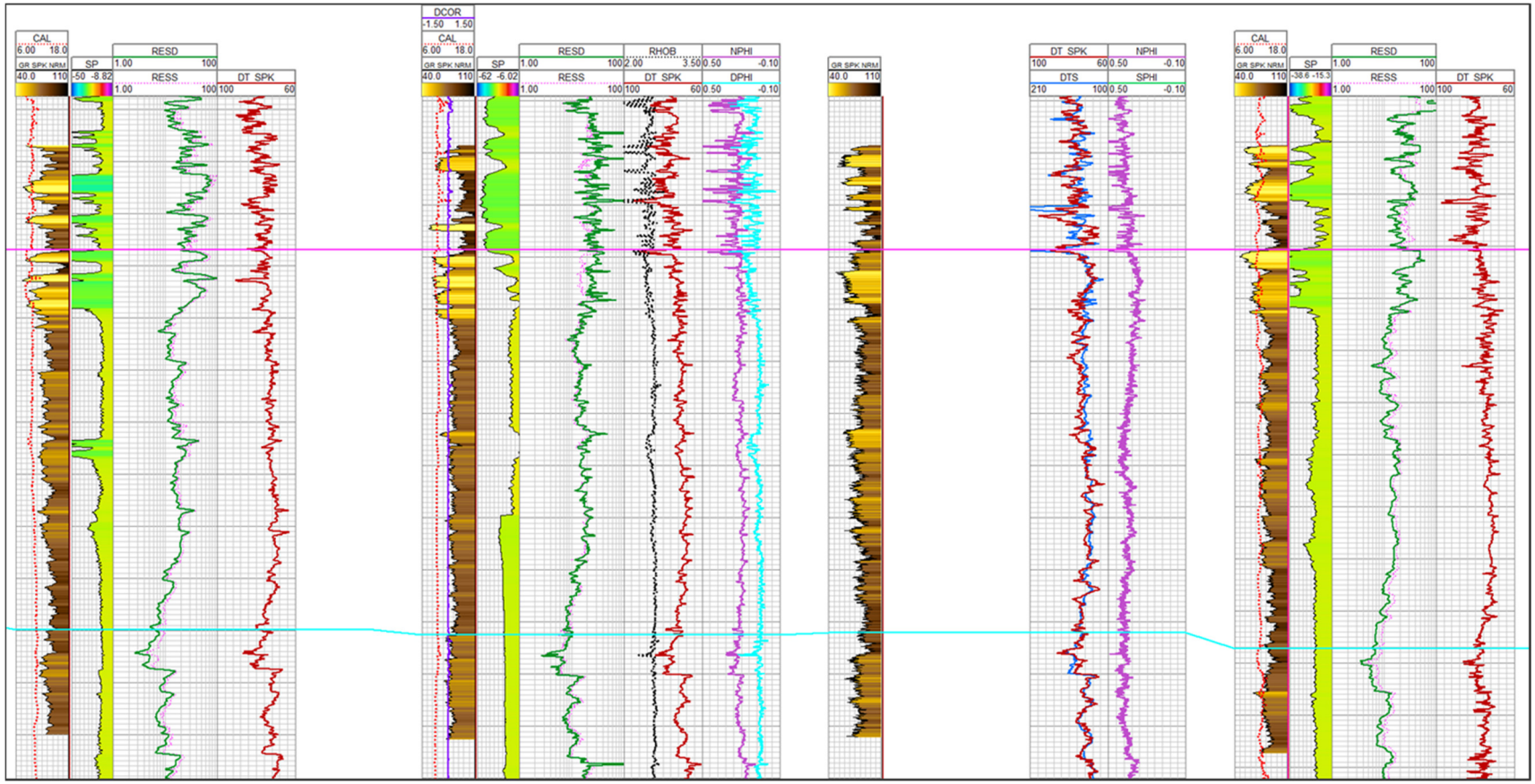

Figure 37. Same set of logs shown in Figure 36, after despiking and normalization.

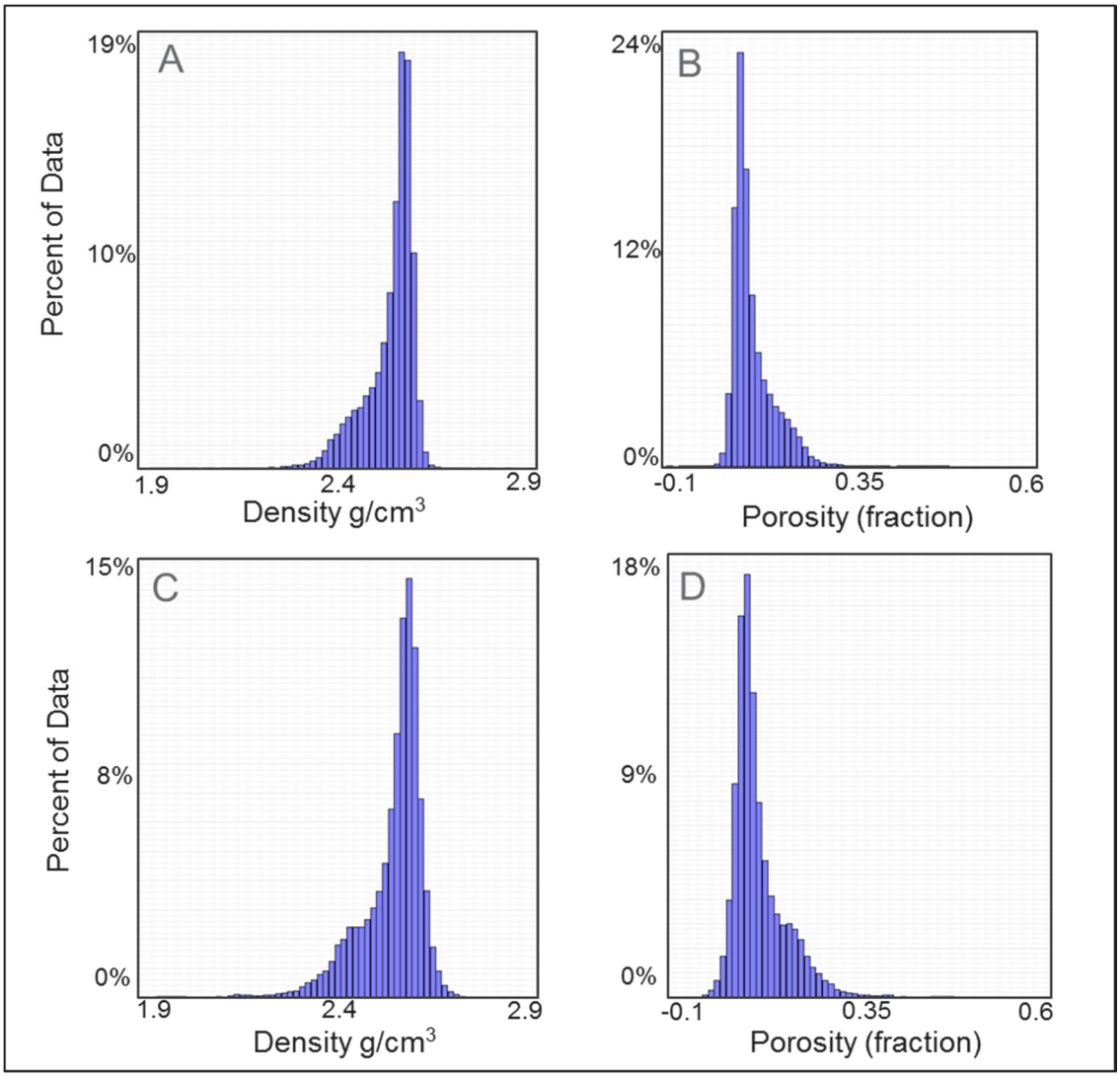

Figure 38. (A) Histogram of the normalized density curves over the Oliver interval. (B) The associated histogram for the porosity calculated from the normalized density using equation A2. (C) The non-normalized density has a well behaved distribution and a majority of the calculated porosities (D) fall within the expected range (i.e. 8-21%) indicating that the non-normalized density curves are suitable to use for the inversion and neural networks.

Appendix B: Inversion

In order to arrive at the desired porosity volume over the Oliver, I must first generate an acoustic impedance (also known as Z_p) volume. Porosity is one of the main drivers of impedance because of its inverse relationship to density and velocity (e.g. In the general case, increases in porosity decrease density and velocity. This suggests that the inverted P-impedance volume should contain the most information about porosity and will thus be a critical input for the neural networks. The first step in estimating impedance is to identify wells that contain good sonic and density data over the Oliver interval. There are 22 wells in the study area that have the necessary log coverage (green highlighted wells in Figure 3) to invert for impedance. After extracting a wavelet from our seismic data over the zone of interest (Figure 39), I use sonic logs to make well ties to align the log response with the seismic response.

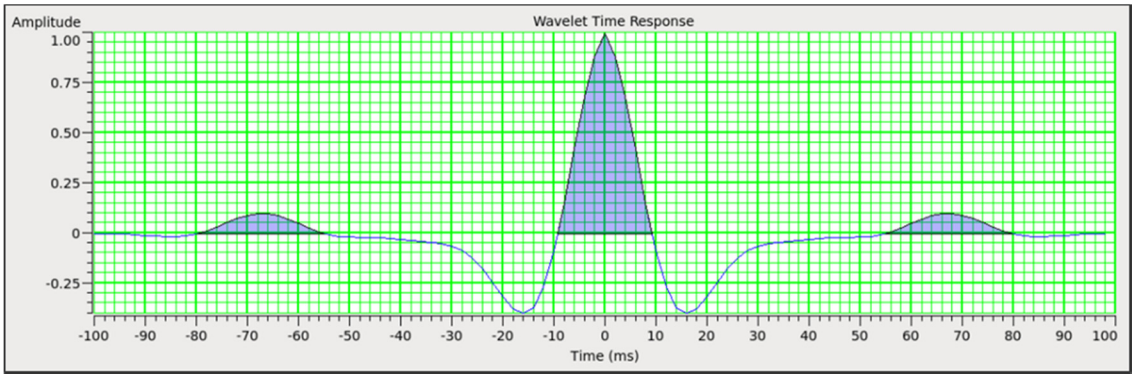

Figure 39. Wavelet extracted over the Oliver interval.

Next, I build an initial low frequency model using the sonic and density logs at the well locations (Figure 40). This model generates an acoustic impedance log which is convolved with the wavelet to create a synthetic seismic response. Then it is compared to the actual seismic response for the well in figure 40, where the synthetic

has a 98% correlation to the real seismic data. Once the wells have all been checked for a sufficiently high correlation I use this modeled relationship to invert the entire seismic volume into an acoustic impedance volume (Figure 41). The output inversion data falls within the range measured by the well logs, 27000-33000 (ft/s)*(g/cm^3). These values are close to the base line impedance one would obtain by computing an average velocity of 12,000 ft/s and multiplying by a quartz density of 2.65 g/cm^3, or Z_p = 31800 (ft/s)*(g/cm^3).

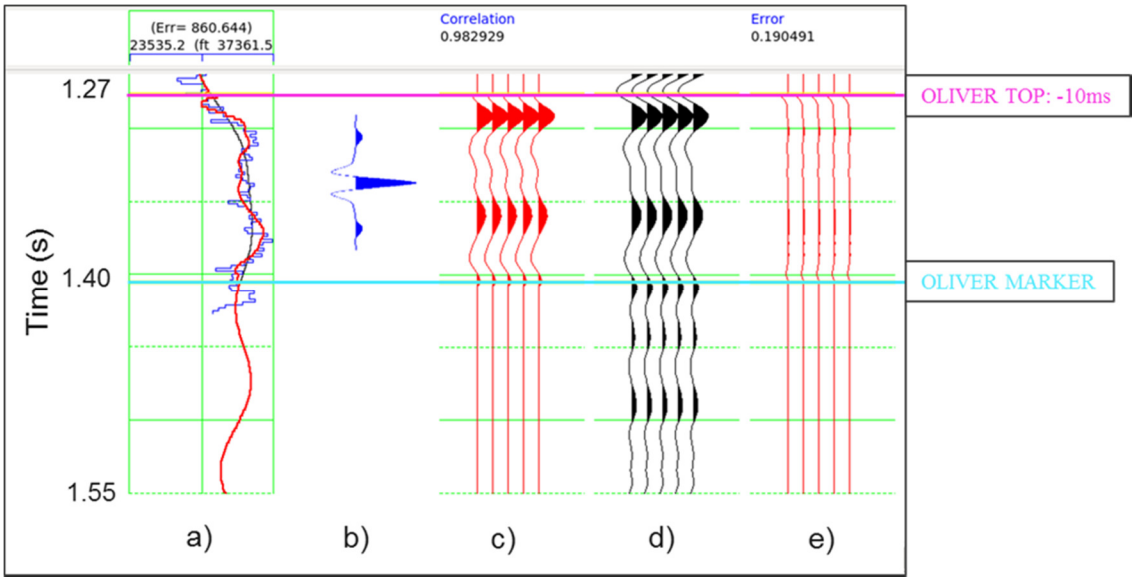

Figure 40. (a) Modeled impedance log (red curve), (b) seismic wavelet, (c) synthetic seismic data from convolving (a) and (b), (d) real seismic data, (e) Error between the synthetic and real seismic data at this well location. The 98% correlation of the synthetic and real data provides a good foundation for the inversion.

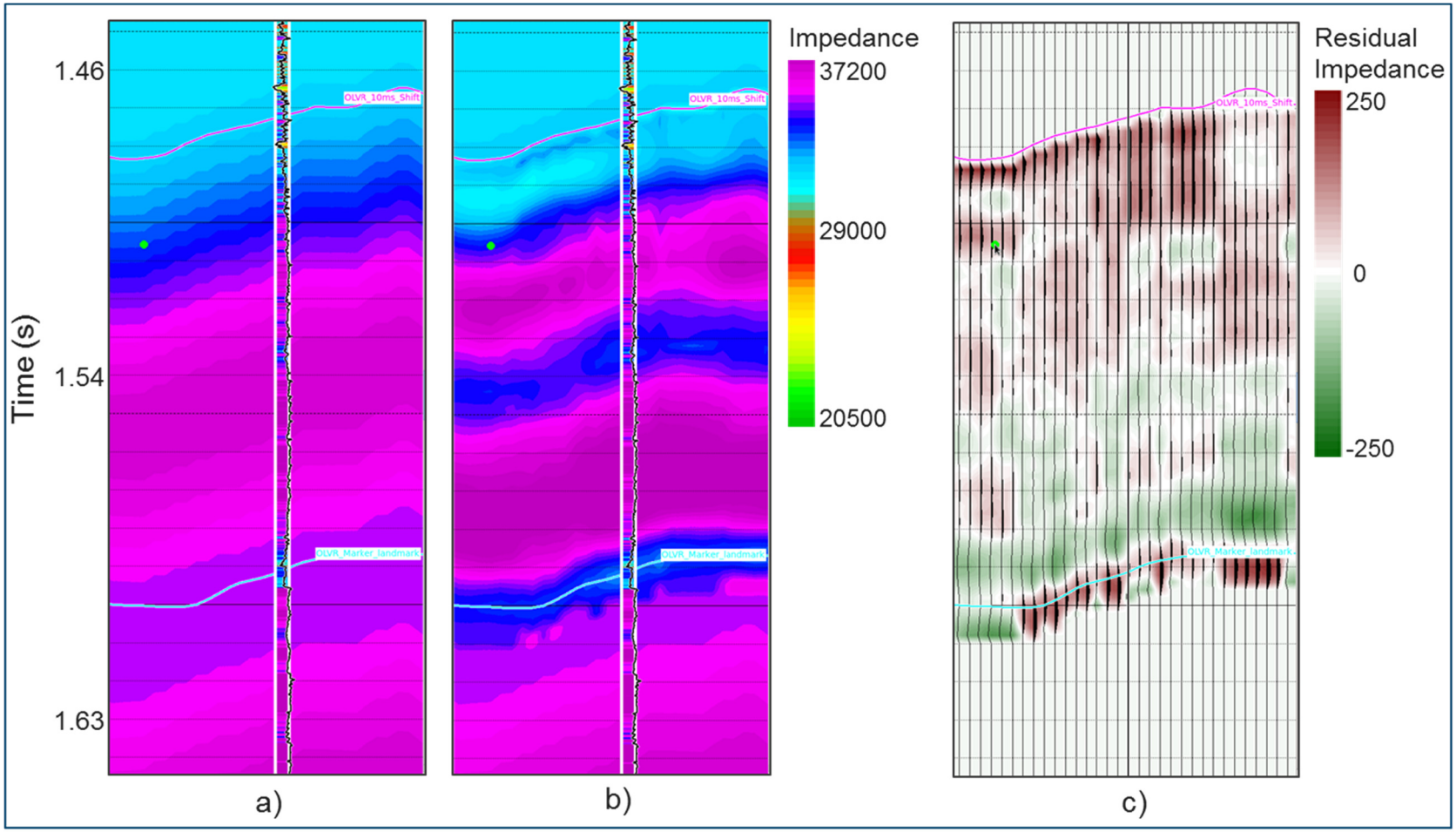

Figure 41. (a) Low frequency model built from the well logs. (b) P-Impedance volume from the inverted seismic. (c) Difference between the low frequency model and the inverted impedances.

Appendix C: Exploratory Data Analysis

Artificial Neural Networks

Once the impedance volume is created I begin using ANN to create our porosity volume. Using the Emerge package in Hampson Russell I take all the generated seismic attributes, including Z_p, and determine if there is a relation between my porosity logs and individual attributes. Emerge creates a single attribute regression for each volume, overlays the regression with the porosity logs, and populates a list of each attribute's correlation and error. As anticipated, the impedance volume has a significantly higher correlation (67.6 %) than any other attribute (Figure 42). Analyzing each attribute's correlation I determine which data sets provide the best trends with the porosity logs. Some attributes have statistically good correlations that need to be rejected. For example, (Figure 43) amplitude curvedness isn't a good choice because it seems to track the upper portion of the log response but is too smooth to be a good representation for the rest of the curve. The low frequency filtered data (Filter 5/10-15/20) provides a good broad trend to the data (Figure 44) which should supplement the higher frequency match of the impedance. Other attributes I thought would be good to incorporate based on the single attribute analysis were GLCM Mean and Amplitude weighted cosine phase (Figures 45 and 46).

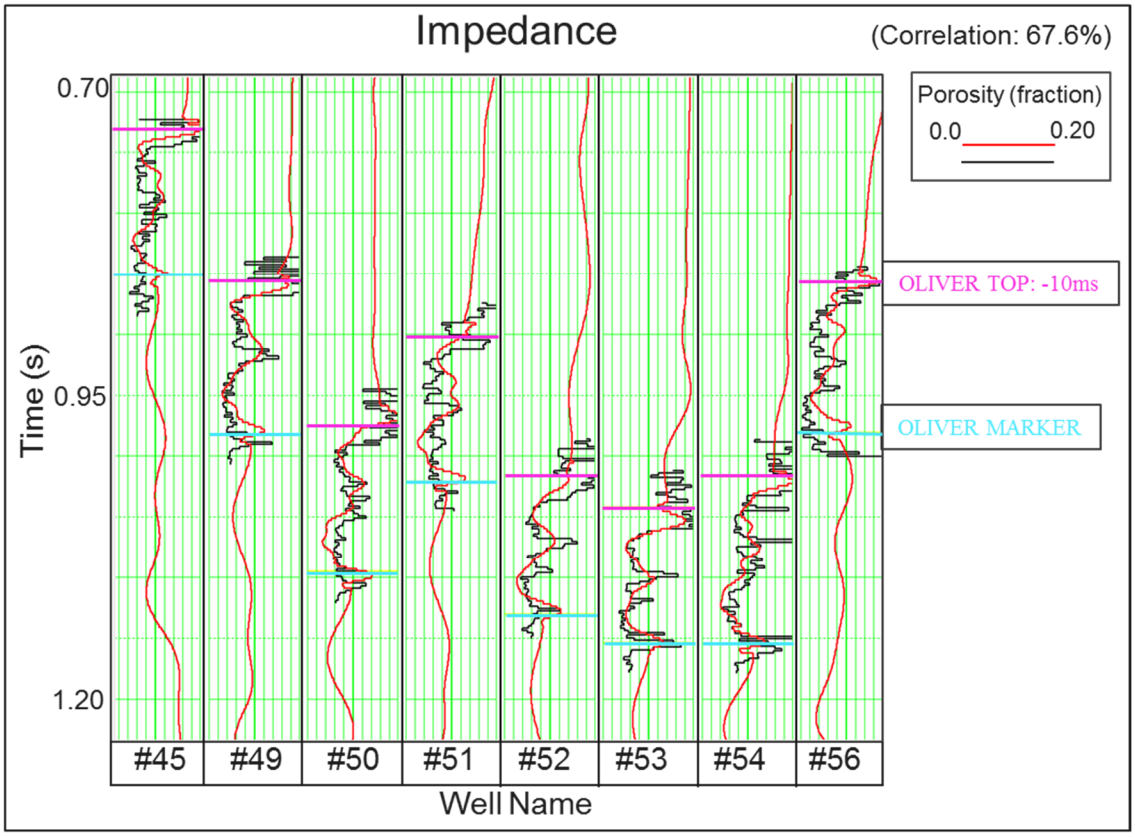

Figure 42. Impedance prediction of porosity using a single attribute regression, for 8 wells in the study area. The red curve is the predicted porosity and the black curve is the original porosity log. As anticipated impedance is the best match to our porosity with a 67% correlation coefficient. The original log curves are in black and the modeled porosity log from Zp is in red.

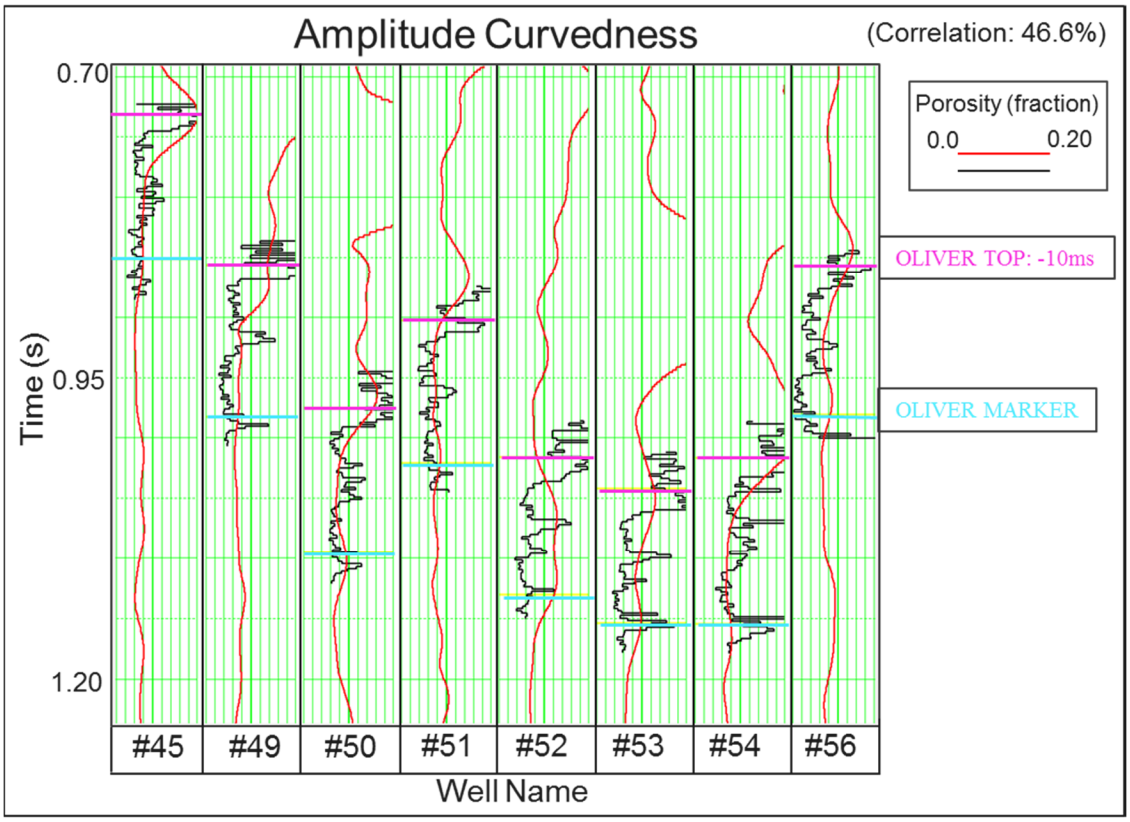

Figure 43. This figure shows the correlation of amplitude curvedness to porosity, the correlation is actually the second highest after Zp but looking at the actual trend of the modeled curves it's apparent that amplitude curvedness I not a good predictor of porosity.

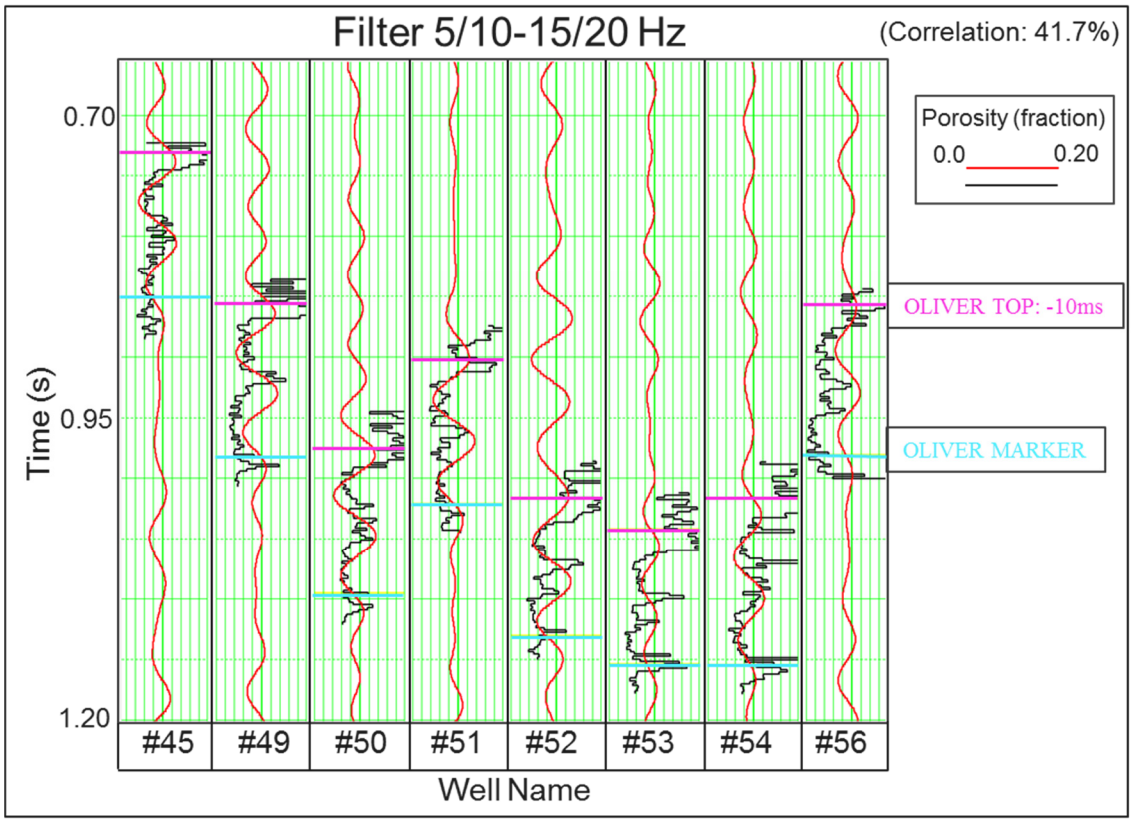

Figure 44. The low frequency filtered data (Filter 5/10-15/20 Hz) has a good trend with the porosity curves and I think it will complement the Zp attribute in the neural network.

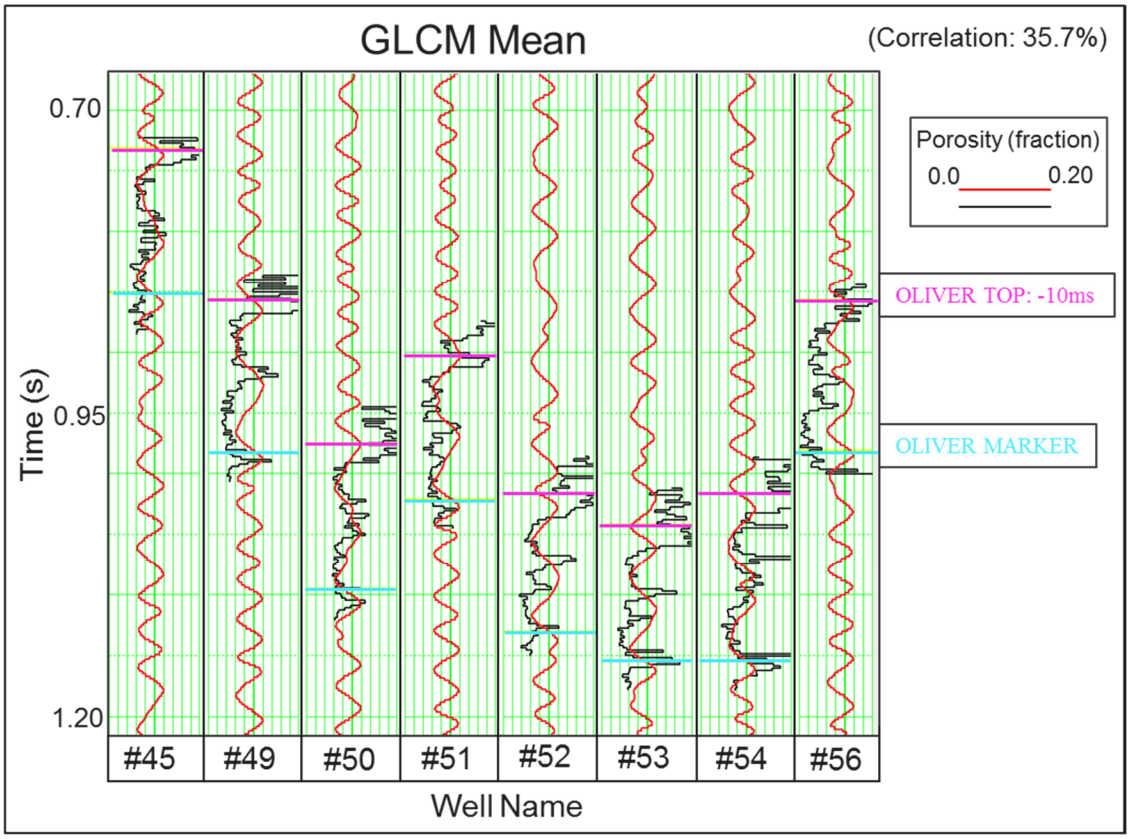

Figure 45. The GLCM mean attribute doesn't have an impressive correlation (36%) but looking at the modeled logs they are generally close to the actual porosity trend (with the exception of well #56 on the right side of the plot).

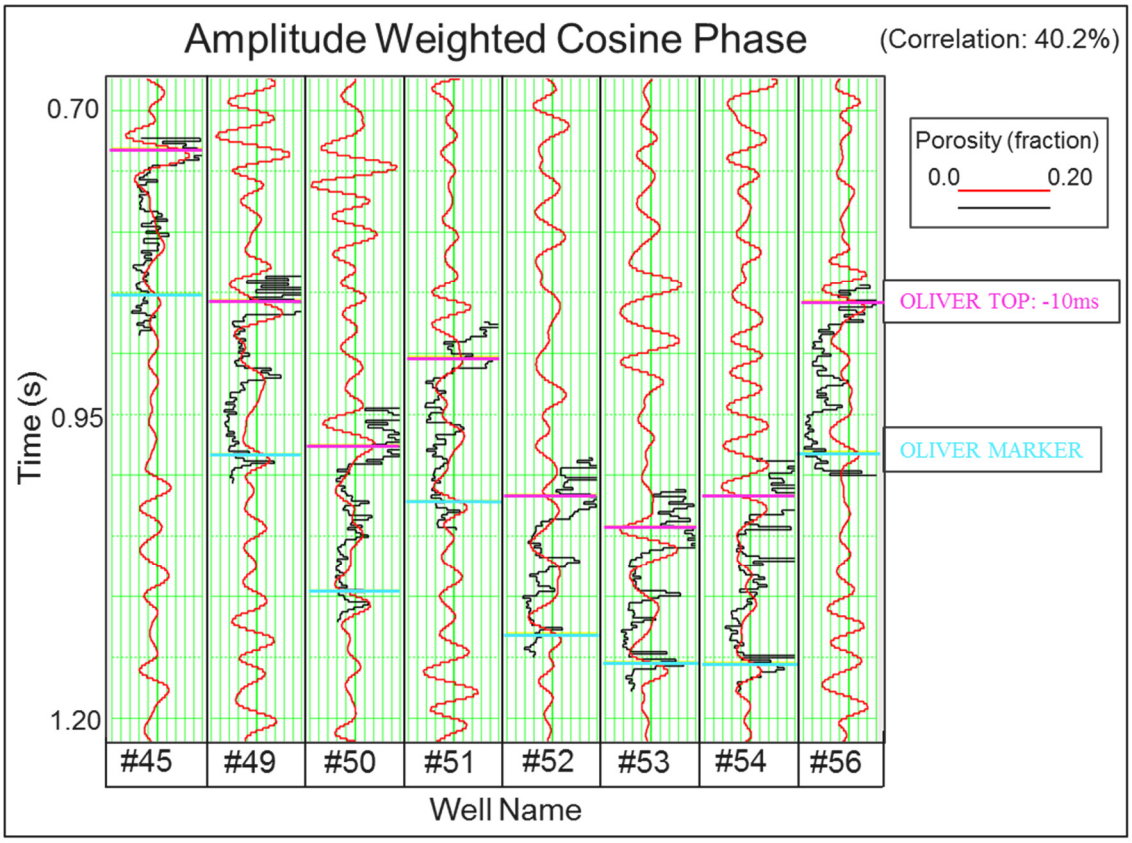

Figure 46. Above is the plot for Amplitude Weighted Cosine Phase. Like GLCM mean this attribute seems to provide a good trend to the porosity and would be a much better fit in the neural network than the statistically determined amplitude curvedness.

Moving on to the multi-attribute regression in Emerge, I input all of our volumes and give the analysis a 10 attribute maximum to consider. The resulting output in Figure 47 shows the best 10 attribute combination to use. However, the validation error increases after the 8th attribute which is an indication of overtraining the dataset (Hampson, 2001). So considering only the top 8 attributes chosen by Emerge I find that the observations from my single attribute analysis are confirmed by the multi attribute output, with Z_p and the low frequency filtered data at the top of the list. Reexamining the validation error, note that the error curve shallows significantly after the 3rd attribute

(Peak magnitude CWT). To be conservative, I consider this the point at which overtraining begins. Furthermore, attributes that reside after this are not logical picks to determine porosity and do not have good correlations in the single attribute comparison. Thus, we keep the first 3 attributes and experiment further by adding in Amplitude Weighted Cosine Phase, GCLM Mean, and even amplitude curvedness to see what results from the multi attribute output (Figure 48). Once again, the first 3 attributes are doing all the work to reduce the validation error and even though my interpretive eye liked certain volumes from the single attribute analysis, it appears that they are actually causing over training and increasing the validation error at well locations.

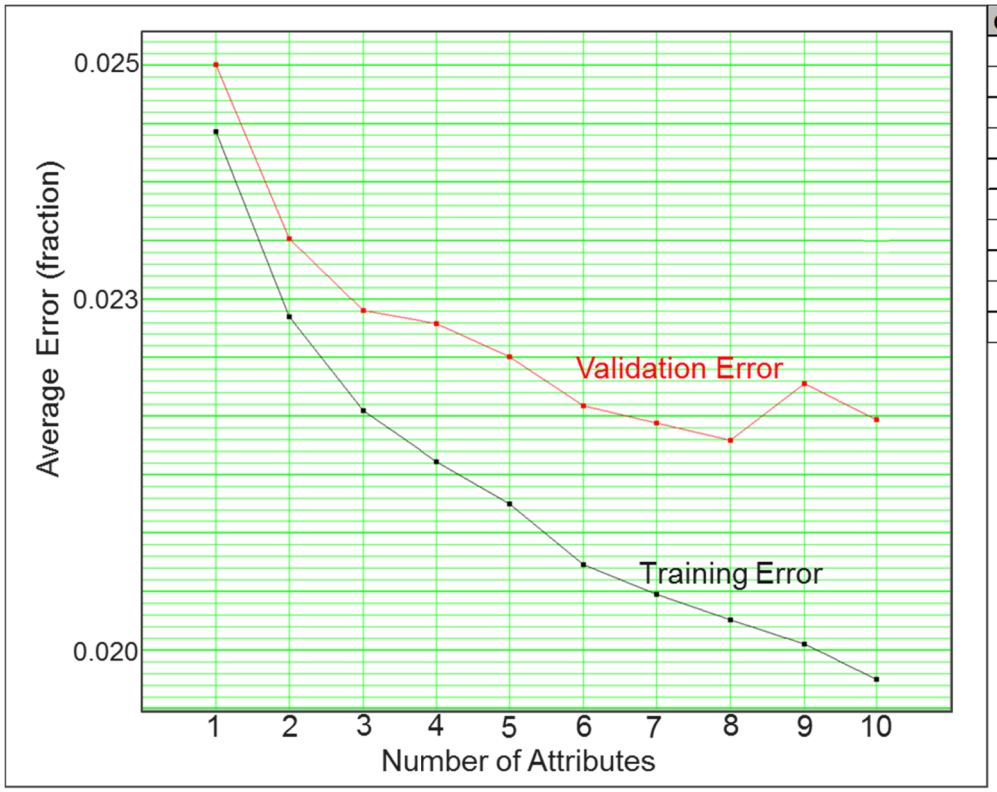

Order	Attribute	Training Error
1	Acoustic Impedance	0.024435
2	Filter 5/10 - 15/20	0.022859
3	Peak Magnitude CWT	0.022052
4	Peak Magnitude Above Average	0.021619
5	Reflector Convergence Magnitude	0.021254
6	Most Negative Principal Curvature	0.020738
7	Second Derivative	0.020484
8	Derivative of Instantaneous Amplitude	0.020264
9	Dip Magnitude	0.020058
10	Inline Dip	0.019754

Figure 47. Training error (in black) and validation error (in red) for the 10 best attributes selected from exploratory data analysis. Validation shows that error increases after the 8th attribute which indicates the point where overtraining of the network begins. The validation curve shallows significantly after the 3rd attribute and investigating the single attribute correlations for the bottom 7 attributes results in a poor match to the porosity. To ensure we do not overtrain the network I will only consider the top three attributes as candidates for the ANN.

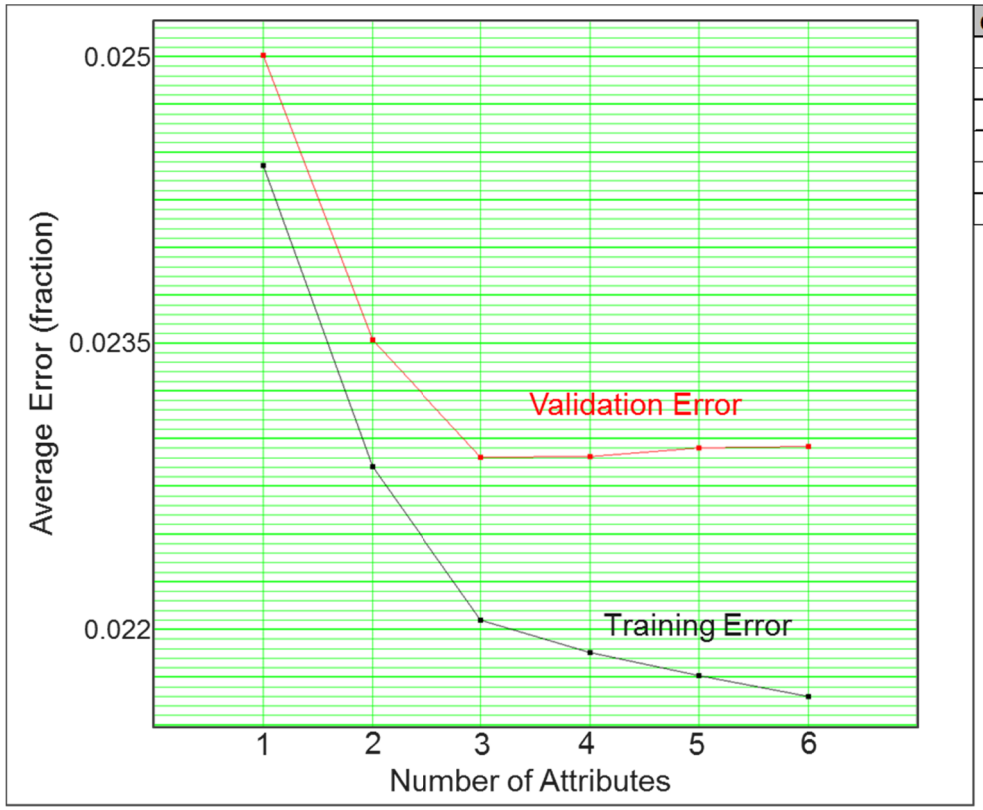

Order	Attribute	Training Error
1	Acoustic Impedance	0.024435
2	Filter 5/10 - 15/20	0.022859
3	Peak Magnitude CWT	0.022052
4	Amplitude Weighted Cosine Phase	0.021883
5	Amplitude Curvedness	0.021764
6	GLCM Mean	0.021652

Figure 48. In this iteration the top three attributes are the same as the last and the additional inputs that we liked for our single attribute analysis actually increase the validation error and cause the network to be over trained.

I feed these three attributes (Zp, Filter 5/10-15/20, and CWT peak magnitude) into a training process for differing types of neural networks to determine which one best predicts my porosity curves. The MLFN with 10 nodes in the hidden layer and using a 7 sample convolutional operator yields a good result (Figure 49) and matches some of the finer detail of the porosity curve. Experimenting with fewer nodes has the effect of making the resultant prediction more "blocky" (Figure 50) because the higher number of nodes in the hidden layer functions similarly to a higher order polynomial making the result smoother. Applying a RBFN to the same data with the same parameters gives a much smoother result since the activation functions of the nodes are smooth Gaussian curves (Figure 51). Overall the RBFN matches well but I prefer to see the level of detail that was obtained with the MLFN. Finally, testing the probabilistic neural network I obtain another smooth result (Figure 51) because the PNN applies a smoothing function for every input attribute in order to minimize error, but appears to capture slightly more detail than the RBFN. After this analysis, I choose the MLFN as my final network. After training the network, it must be validated. The Hampson Russell software employs a cross-validation technique, whereby the network iteratively removes a well from the set, the network predicts the porosity at that location and compares it to the real log. This is done for all 22 wells in the data set and results in a true prediction error between wells. I find that the correlation decreases slightly (Figure 53) by removing a well, since it intrinsically diminishes the predictive power of the network (Hampson et al, 2001). The validation result is still rather good and we can now apply the trained network to the entire seismic volume to generate the final porosity volume shown in Figure 27.

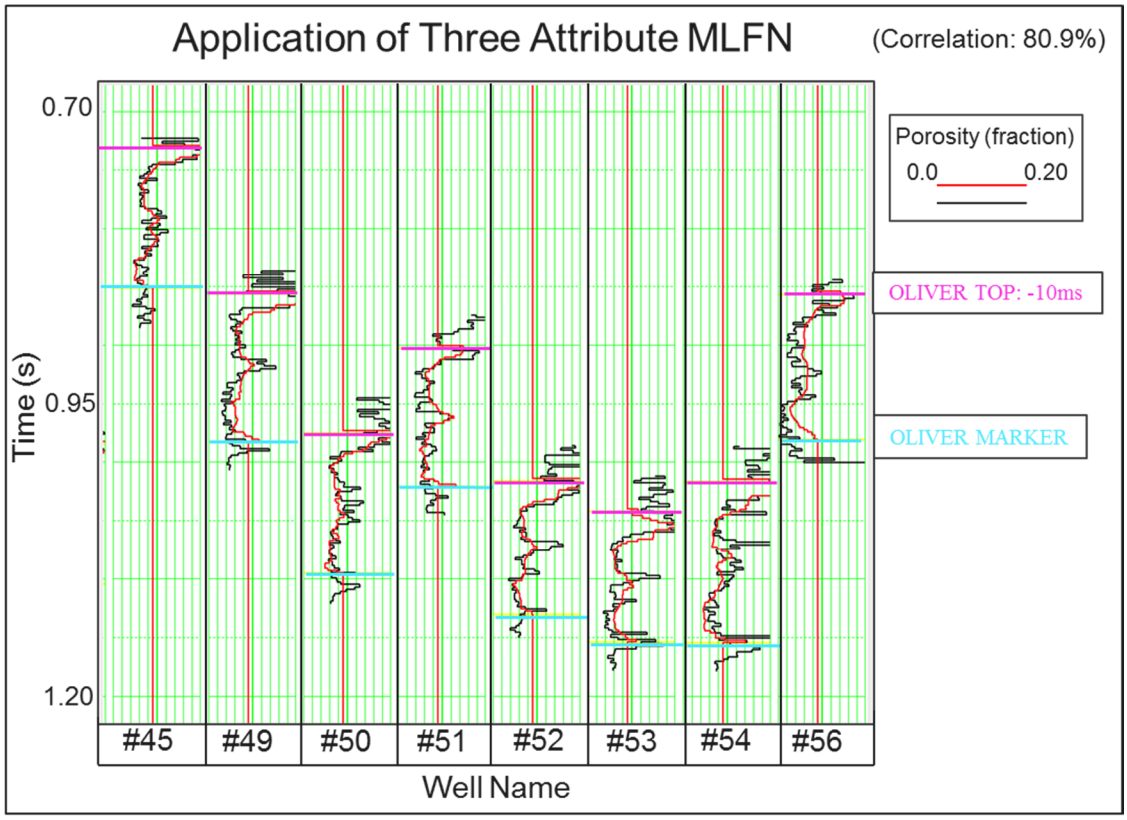

Figure 49. Prediction of porosity using a multi-layer feed-forward neural network, showing a ~81% correlation.

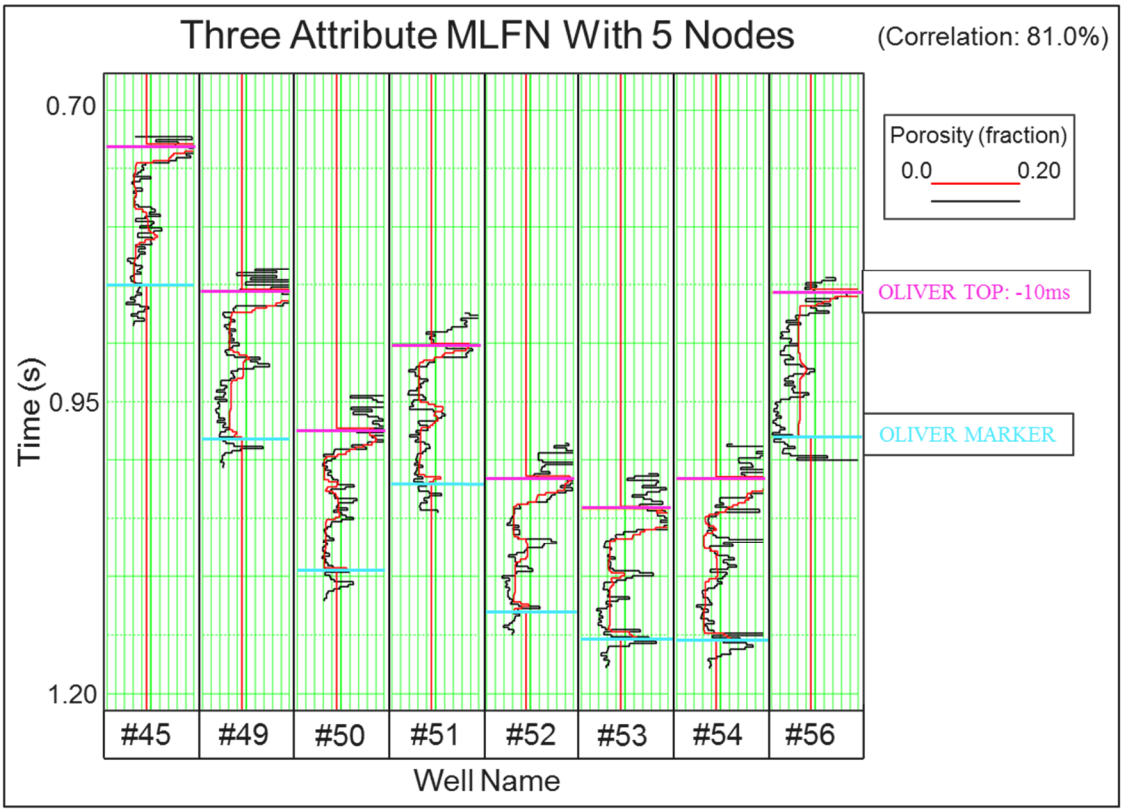

Figure 50. The effect of reducing the number of hidden nodes from 10 to five. The prediction is now blocky compared to the previous prediction using ten nodes.

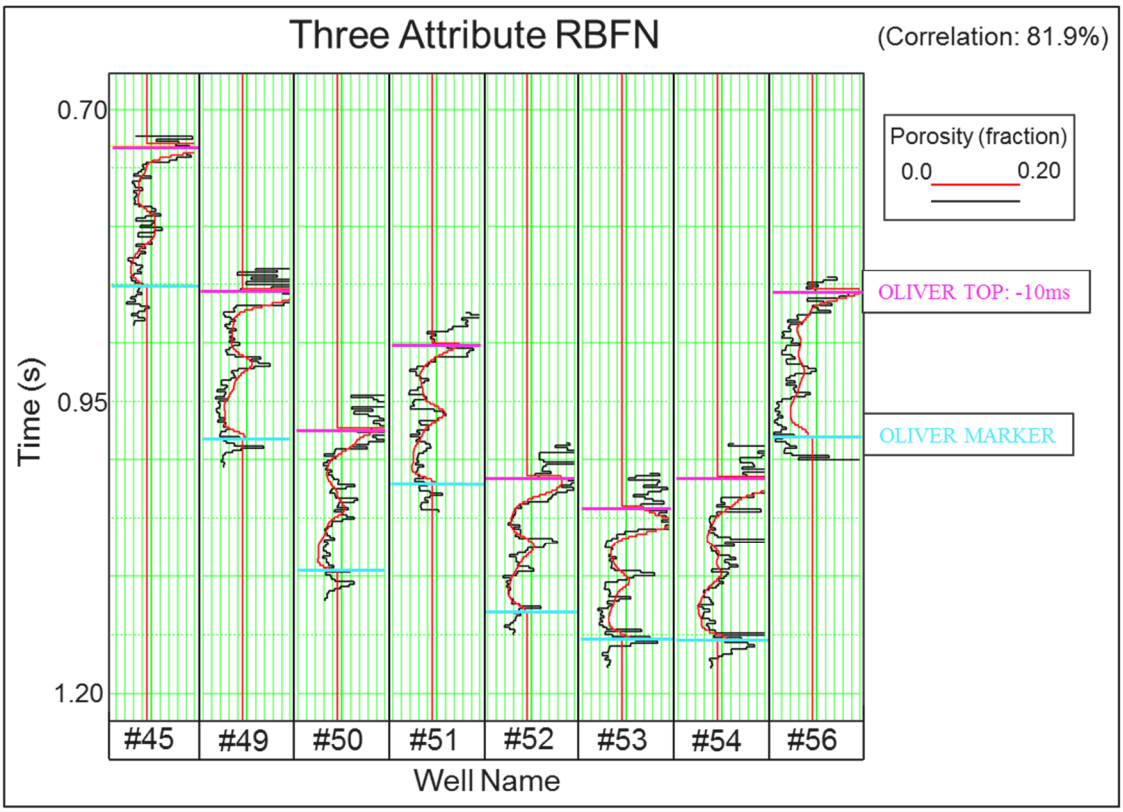

Figure 51. The results of the radial basis function neural network, displaying a much smoother porosity prediction compared to the MLFN.

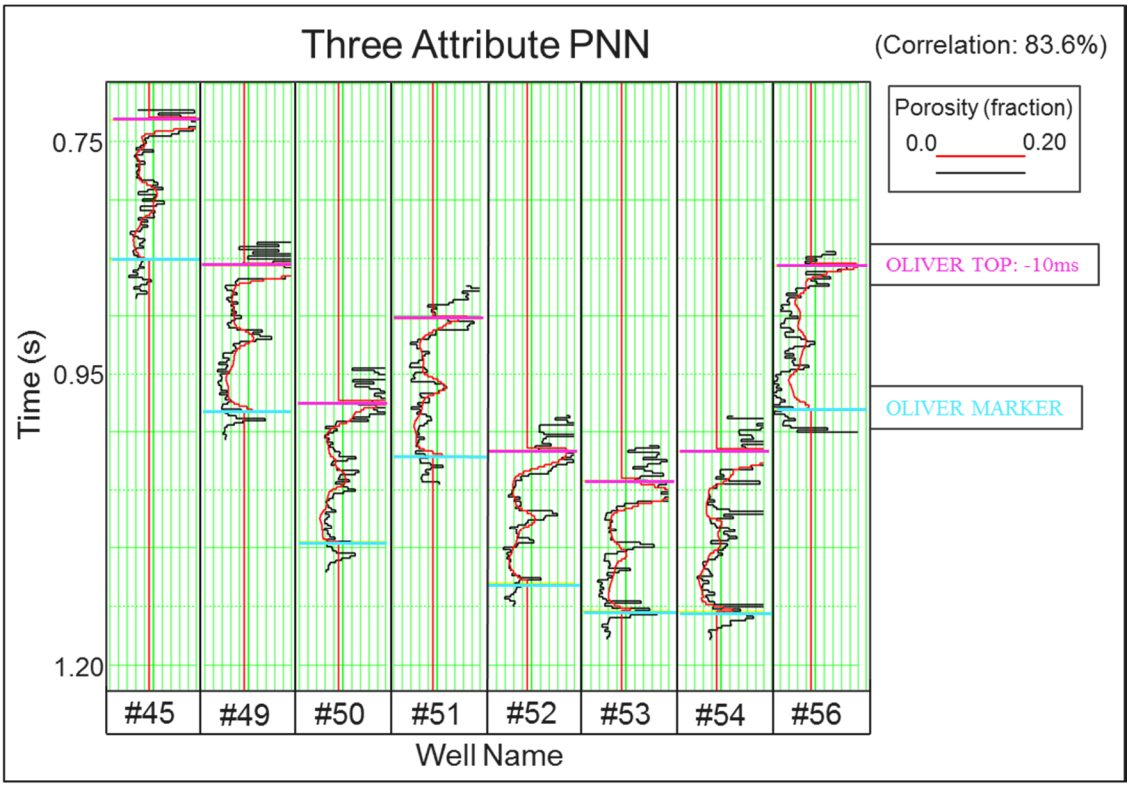

Figure 52. The porosity prediction results of the probabilistic neural network. Similar to the radial basis function neural network it provides a smoother fit of the porosity data, with an overall good prediction (83% correlation).

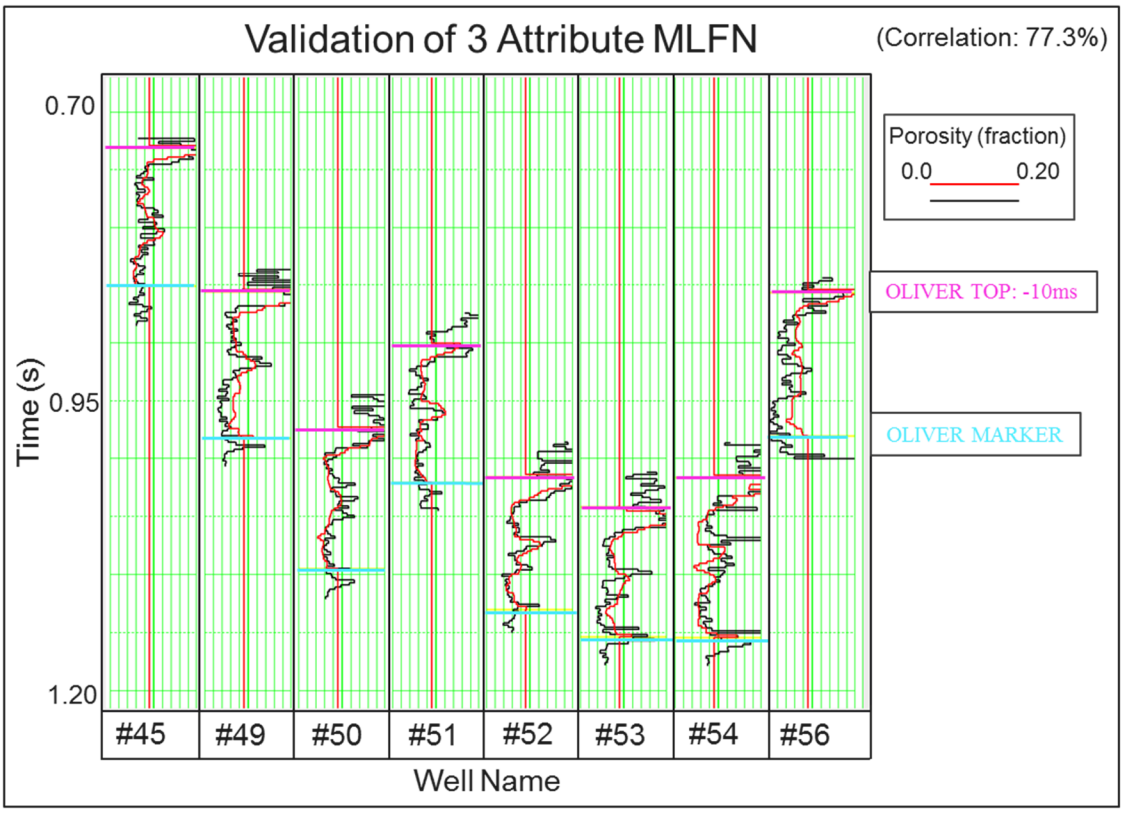

Figure 53. Validation results of the porosity prediction for the 10 node MFLN are slightly lower (77%) than the correlations in the training because the cross-validation technique intrinsically lowers the correlation since we are calculating the prediction with one less well.

SOM

To run the SOM application in the AAPSI software I select a suite of attributes whose relationships are independent of one another (Zhao et al, 2016), which allows the SOM algorithm to freely classify data clusters without using redundant attributes that may predetermine our result. To identify which attributes to use, I employ a combination of visual interpretation and statistical cross plotting of the attributes. Looking at attribute extractions at the top of the Oliver help delineate what attributes may be of the best value in classifying different elements of the depositional environment (Figures 54-58). Statistical correlations of each pair of attributes

constrained to the Oliver interval prevents redundancy (Figure 59). In the initial SOM I chose Coherent Energy, GLCM mean, and Peak Frequency as three of the inputs because of their uniqueness in mapping the depositional features of the Oliver. The other two attributes (Dip magnitude and GCLM correlation) were used as structural inputs to aid in classification of faulted areas and the edges of fine features. The resulting volume (Figure 60) shows three distinct classifications; orange facies corresponding to the coastal plain environment, green facies corresponding with the fluvial and more chaotic middle shoreface regions, and the purple classification corresponding to the distal portions of the system that may be related to silty or muddy facies. Note that the two previously observed channel systems are classified as two different colors. This is likely the result of the differing dimension of the two channels which produce different frequency responses (Figure 57). Since I used peak frequency as an input, the effect of this frequency response is reflected in the SOM. Although we are getting some discrimination between feature types, the SOM is heavily dominated by the coherent energy attribute. Looking at Figure 54, the areas of high coherent energy (red and yellow regions) have strong visual correlation to the orange coastal plain facies in Figure 60; and the areas of low coherent energy have a strong visual correlation to the green chaotic facies. It also appears that the GLCM correlation is actually causing a lot of high frequency noise in the map. Examining Figure 55, the GLCM correlation has a lot of color variation over a small region, and this manifests as a high frequency disruption between the orange and green facies colors (Figure 60). Running a second iteration of the SOM using slightly different attributes (Figure 61)

results in a much different image that is less dominated by the coherent energy (Figure 62).

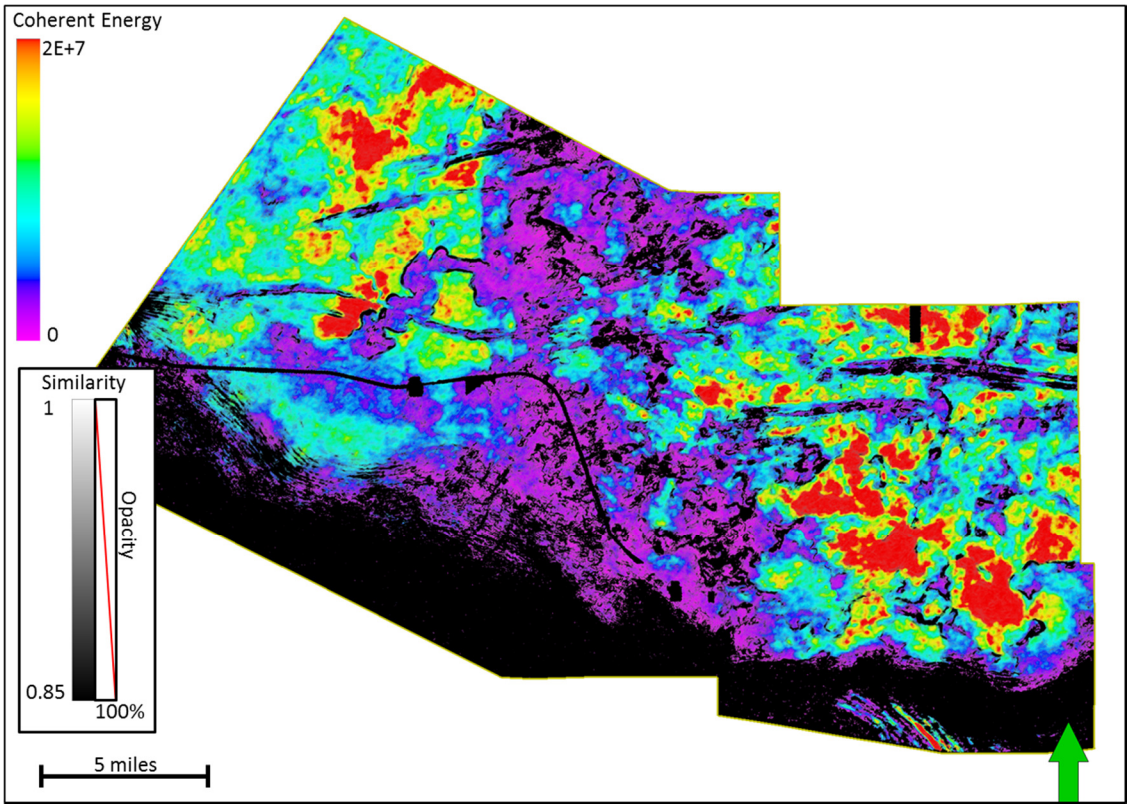

Figure 54. Horizon slice at the Oliver top, through coherent energy co-rendereed with Sobel filter similarity

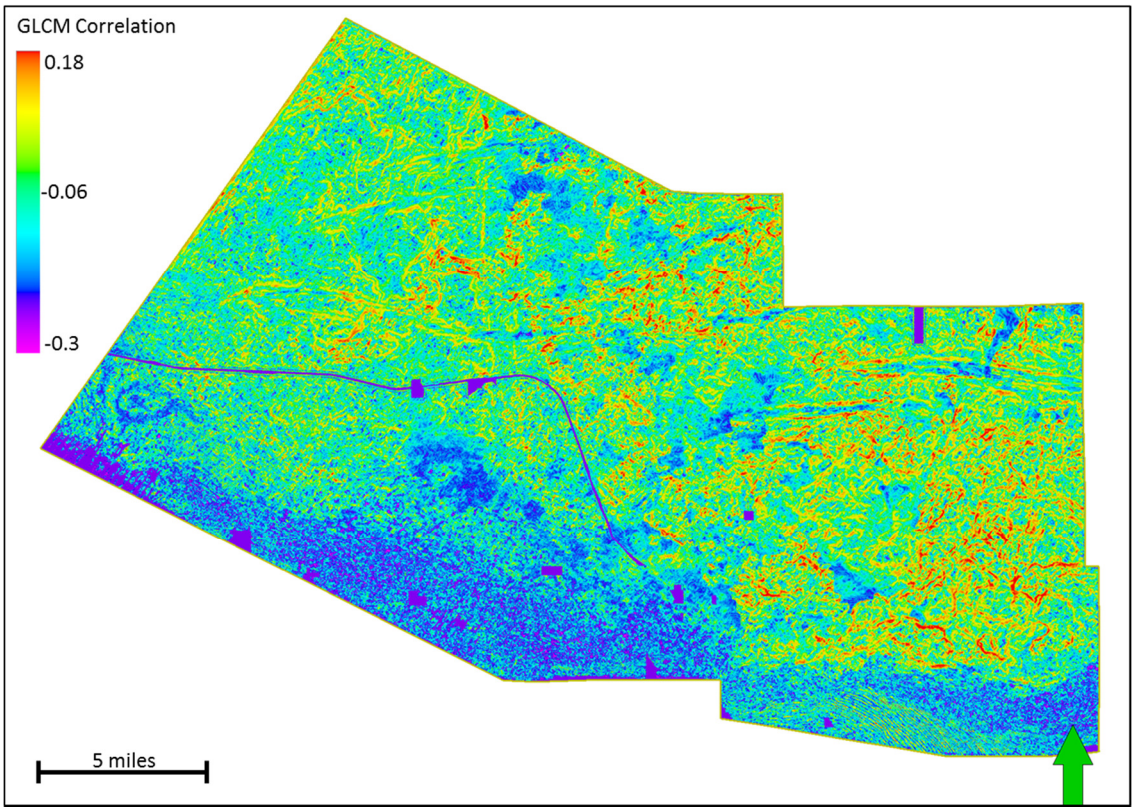

Figure 55. Horizon along the Oliver top through the GLCM correlation volume.

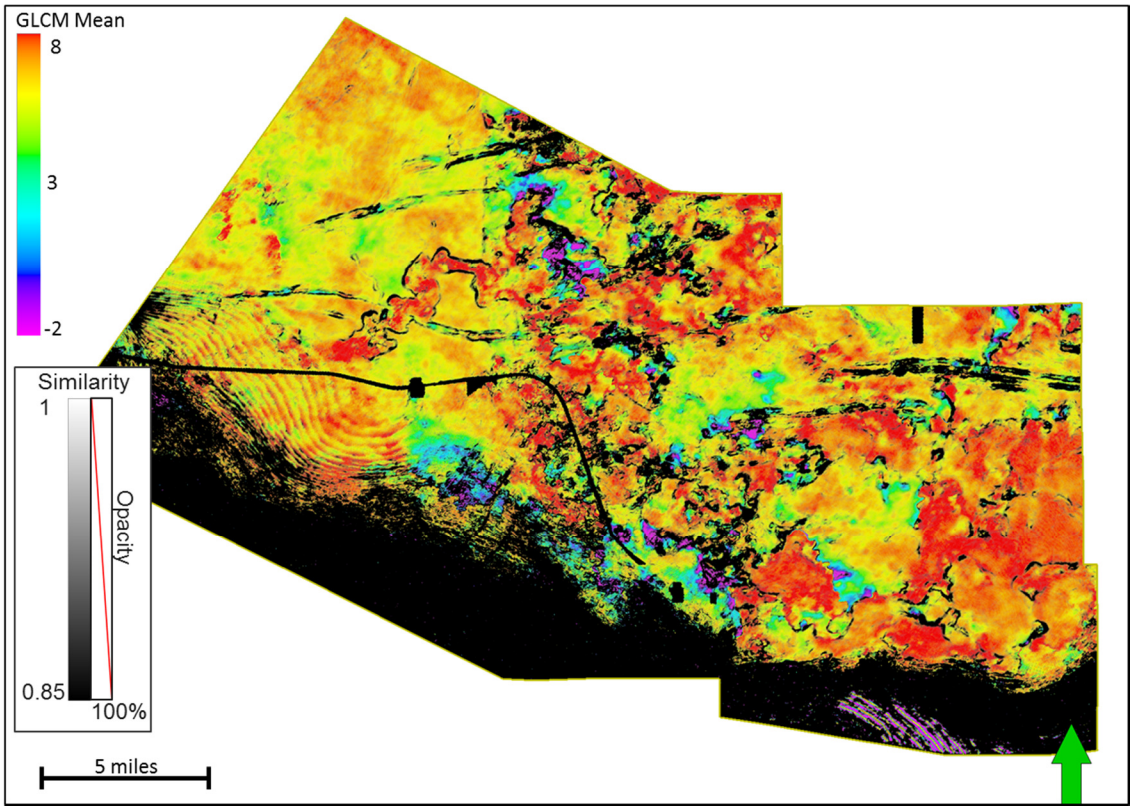

Figure 56. Oliver Top horizon slice through GLCM Mean co-rendered with Sobel filter similarity.

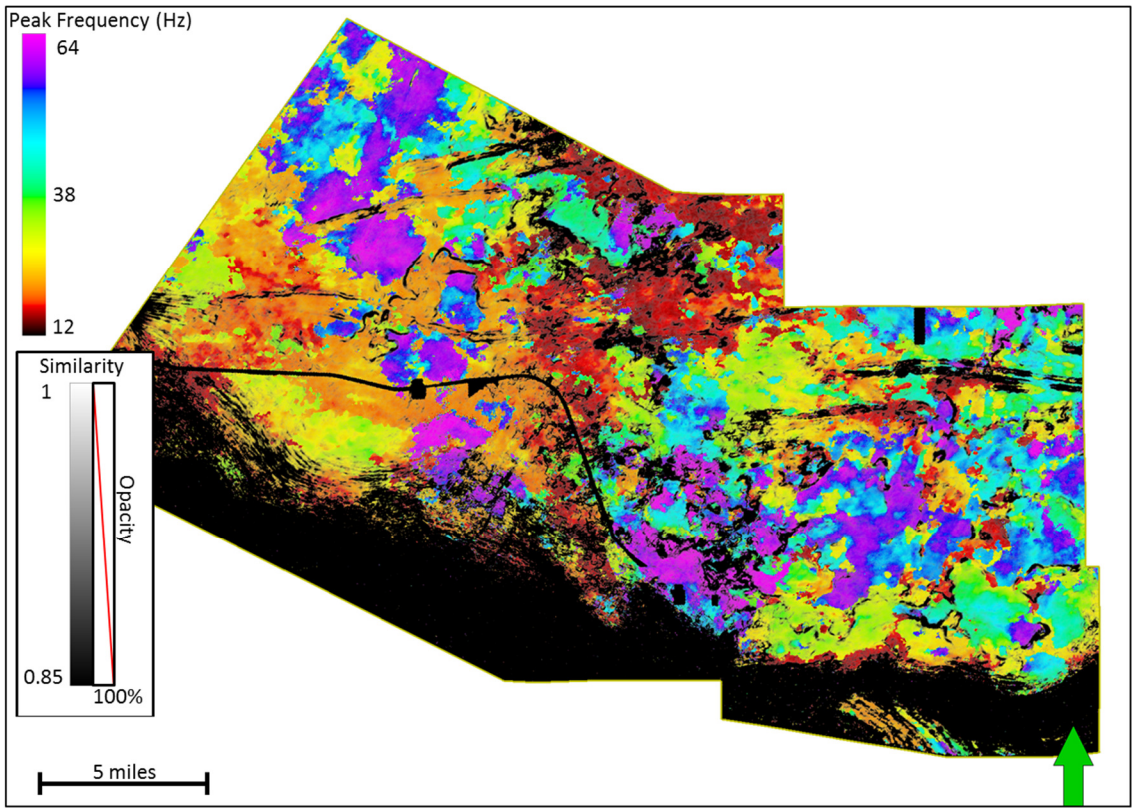

Figure 57. Oliver top horizon slice through CWT Peak frequency co-rendered with Sobel filter similarity. White arrows point out the higher frequency response of the eastern channel feature (narrow channel, which translates to shallower channel depth, causing higher frequency). The black arrows point to the lower frequency response of the western channel (wider channel, translates to deeper channel scour, causing lower frequency).

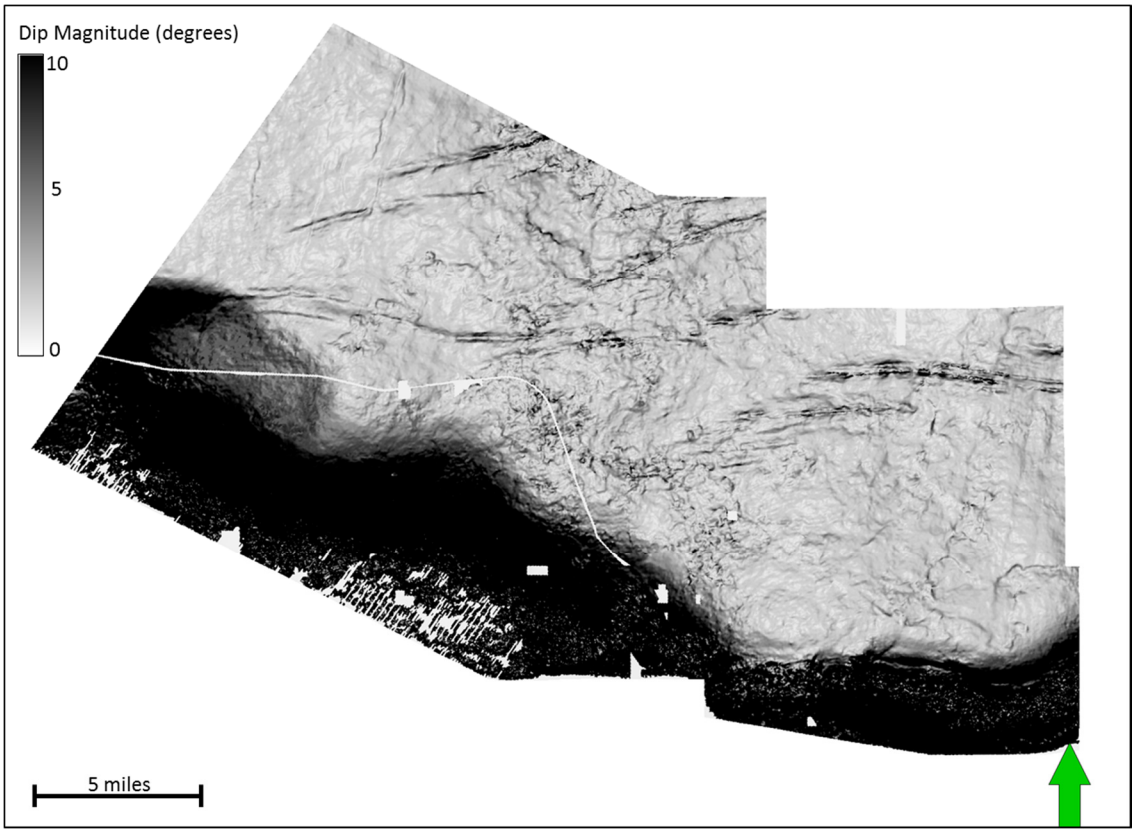

Figure 58. Dip magnitude extracted on the Oliver Top, displaying higher dip along the basin margin in the south and along the wrench faults.

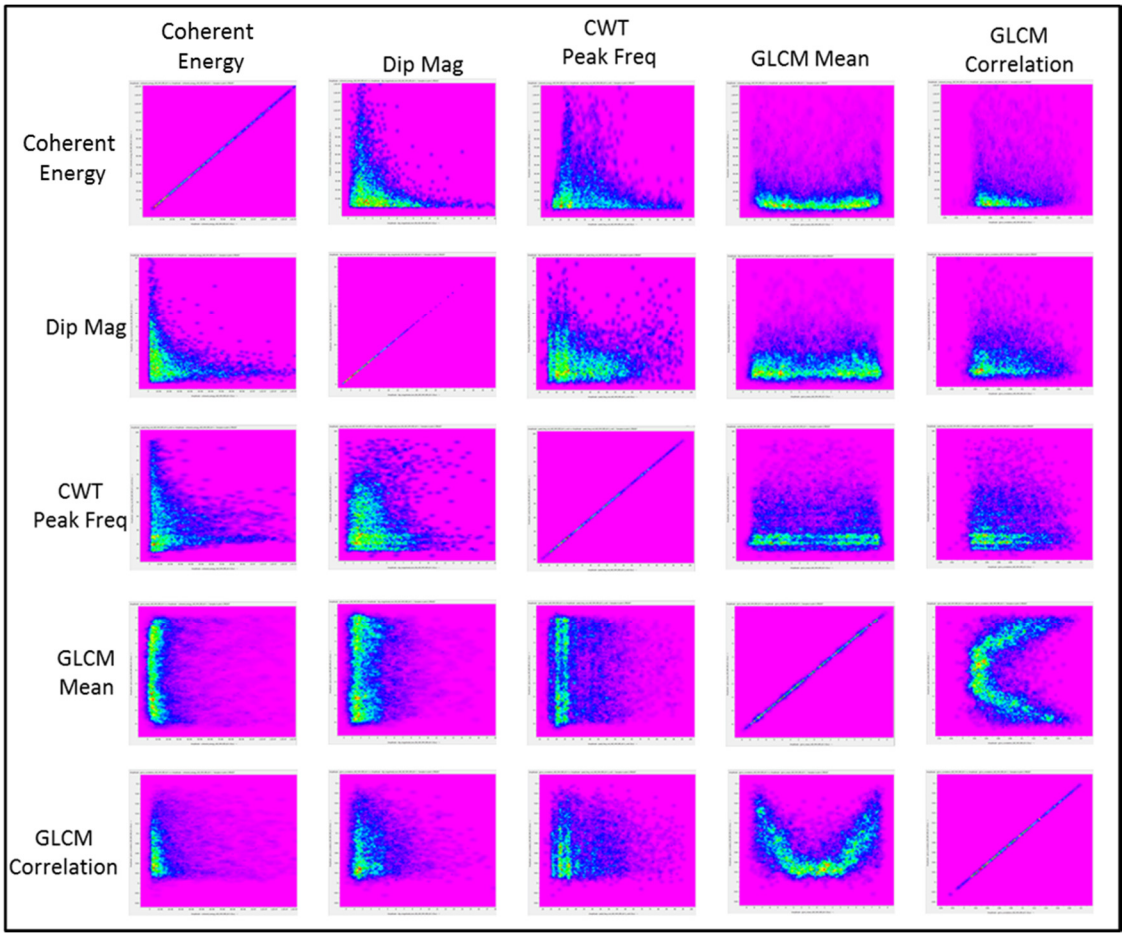

Figure 59. Correlations of all 5 attributes over the Oliver interval show independence of inputs with all R^2 values being less than 0.1.

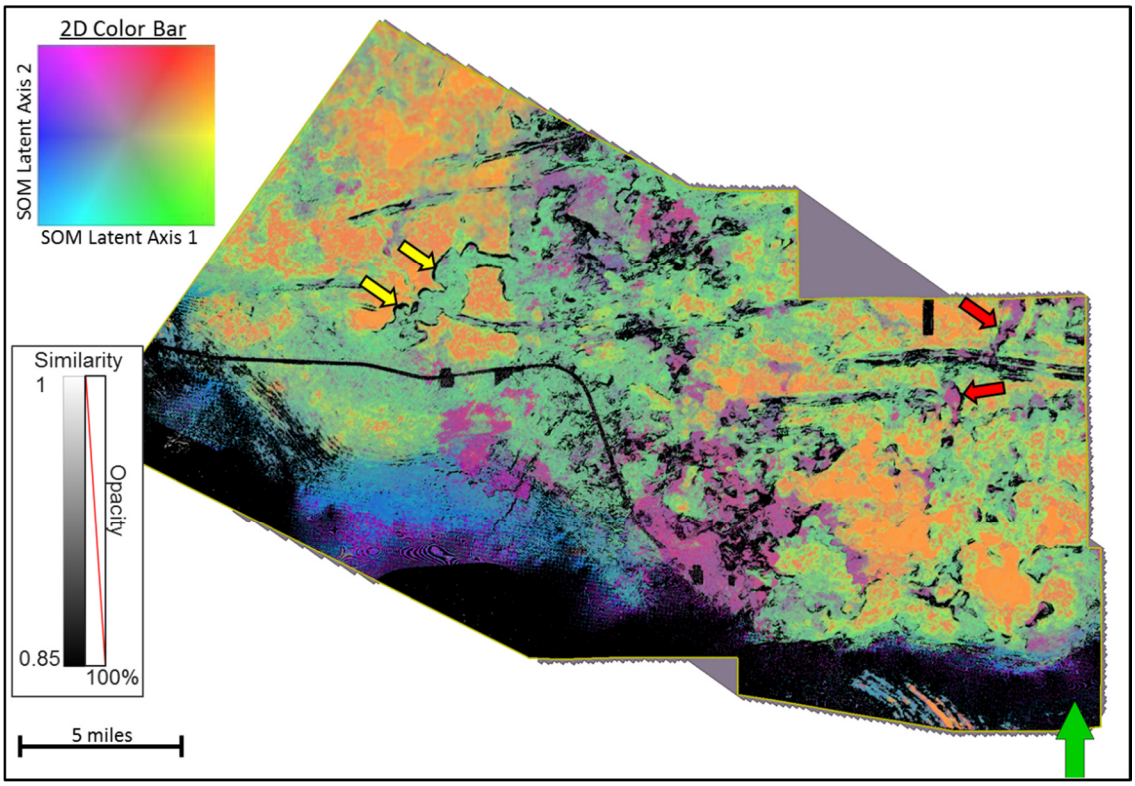

Figure 60. Horizon slice along the top Oliver through the SOM volume. This iteration provides good interpretation but are largely guided by the coherent energy; the orange facies color correlates strongly with the high coherent energy in Figure 54, while the green facies has a high correlation with the low coherent energy. Red arrows indicate the purple fill on the eastern channel while the yellow arrows indicate the larger western channel that is filled with the green facies. The reoccurrence of the orange coastal plain facies on the east is indicative of the development of the Oliver 600 and bolsters our evidence that the 600 sand is somehow related to the losses.

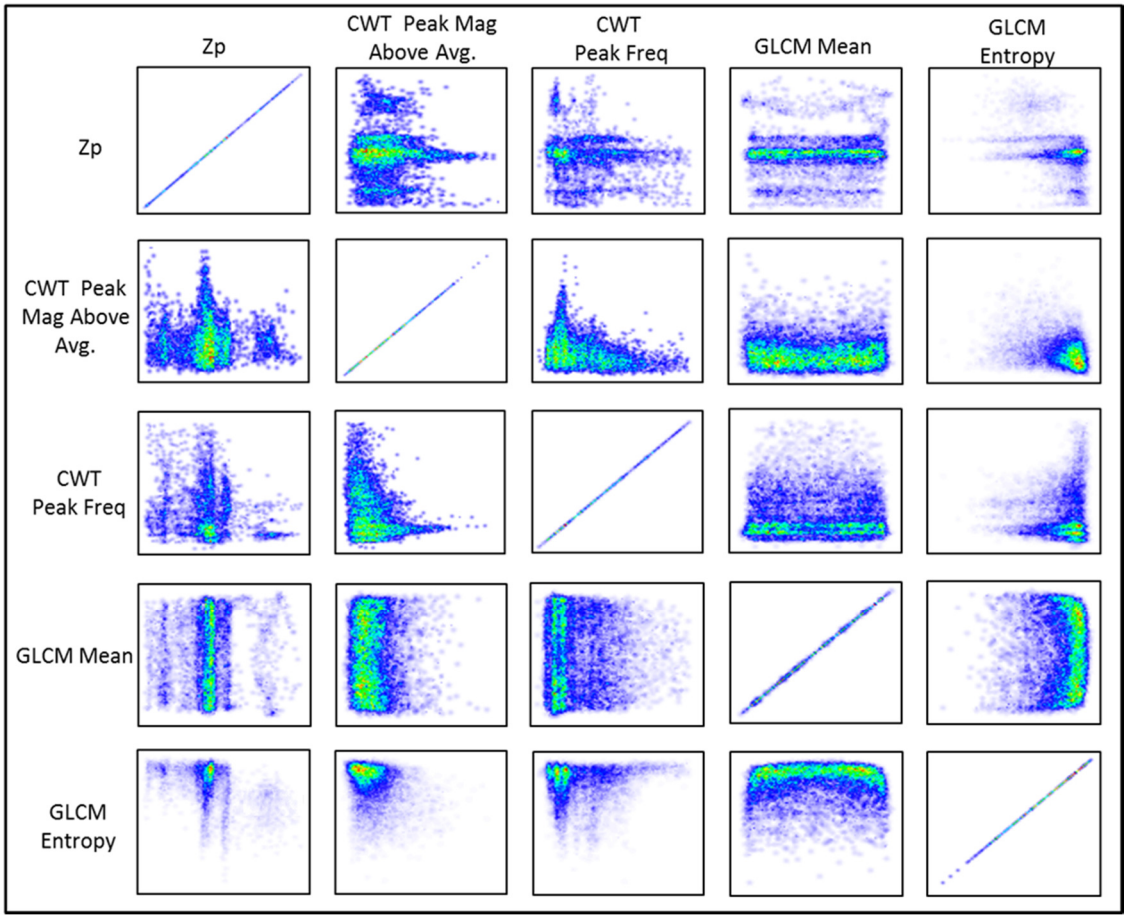

Figure 61. Correlations for the input attributes used in the second SOM.

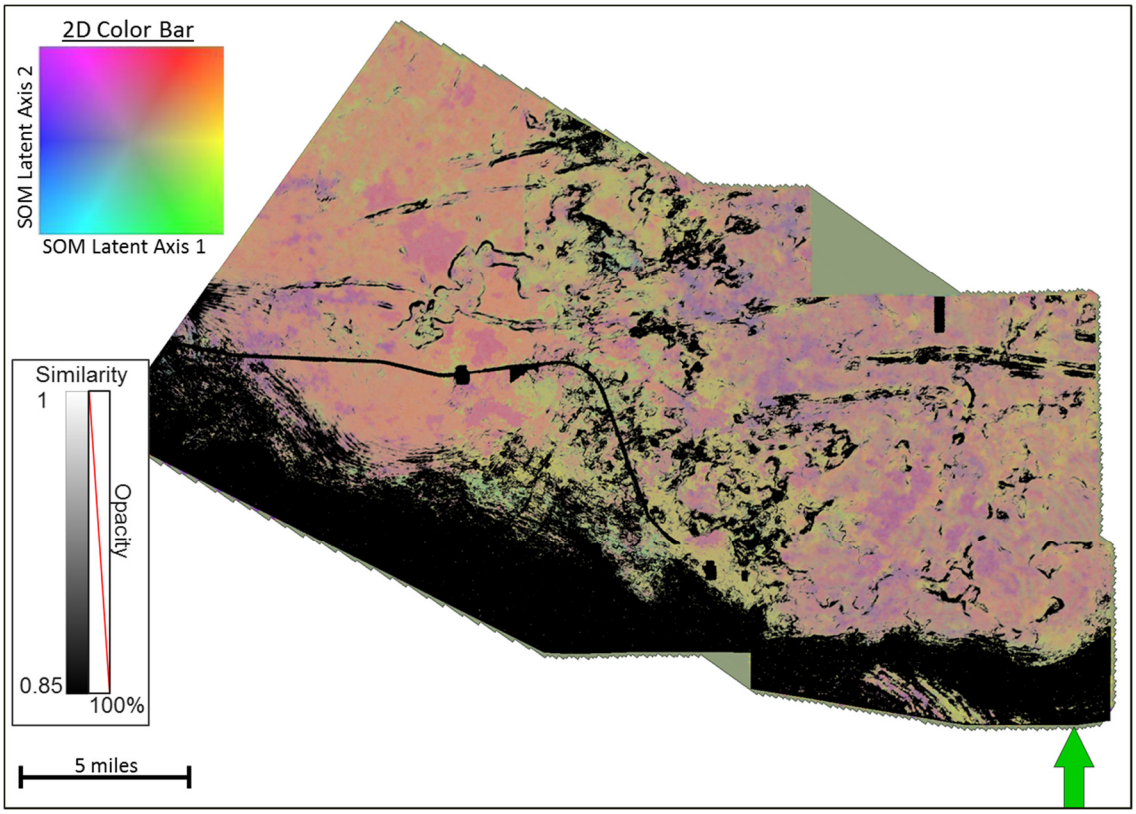

Figure 62. Horizon Slice along the top Oliver though the SOM volume computed using the five attributes shown in Figure 61. The coloration for this SOM is not as dramatic as the first, having at most three or four clusters. Although I like the first SOM better for interpreting the channels I like this version for classification of the shoreface facies (the dark yellow color).